

2018

Characterizing the Pore Structure of the Marcellus Shale

Liaosha Song

Follow this and additional works at: <https://researchrepository.wvu.edu/etd>

Recommended Citation

Song, Liaosha, "Characterizing the Pore Structure of the Marcellus Shale" (2018). *Graduate Theses, Dissertations, and Problem Reports*. 7259.

<https://researchrepository.wvu.edu/etd/7259>

This Dissertation is protected by copyright and/or related rights. It has been brought to you by the The Research Repository @ WVU with permission from the rights-holder(s). You are free to use this Dissertation in any way that is permitted by the copyright and related rights legislation that applies to your use. For other uses you must obtain permission from the rights-holder(s) directly, unless additional rights are indicated by a Creative Commons license in the record and/ or on the work itself. This Dissertation has been accepted for inclusion in WVU Graduate Theses, Dissertations, and Problem Reports collection by an authorized administrator of The Research Repository @ WVU. For more information, please contact researchrepository@mail.wvu.edu.

Characterizing the Pore Structure of the Marcellus Shale

Liaosha Song

**Dissertation submitted
to the Eberly College of Arts and Sciences
at West Virginia University
in partial fulfillment of the requirements for the degree of
Doctor of Philosophy in
Geology**

Timothy R. Carr, Ph.D., Chair

Ebrahim Fathi Ph.D.

Shikha Sharma Ph.D.

Timothy A. Warner Ph.D.

Amy Weislogel, Ph.D.

Department of Geology and Geography

Morgantown, West Virginia.

2018

**Keywords: porosity, pore size distribution, Marcellus Shale, SEM, pore structure,
microporosity, sorption, shale gas reservoirs**

Copyright 2018 Liaosha Song

ABSTRACT

Characterizing the Pore Structure of the Marcellus Shale

Liaosha Song

The large hydrocarbon resource and recent success of exploration and exploitation in mudstone (shale) reservoirs has stimulated research interests in these unconventional oil and gas reservoirs. Mudstone is categorized as an unconventional reservoir because of the nanometer-scale pore sizes and extremely low nano-darcy permeability compared to micrometer to millimeter-scale pore sizes and millidarcy to darcy permeability of conventional sandstone or carbonate reservoirs. The introduction of advanced imaging technology provides a powerful tool to examine the complex pore structure of mudrock, although quantification remains a challenge. In addition to the free void space of pores, there is an extra storage mechanism for shale gas, adsorbed gas on pore surfaces of organic matter and clay particles.

Porosity, as a critical reservoir property, has been used to calculate reserves, and permeability to estimate production rates. For an unconventional reservoir, the quantification of porosity and permeability is challenging because of the complexity of pore structure, and the extremely small size of the pore space. In this research, I introduce two cutting-edge technologies, semi-automatic analysis of ion milled scanning electron microscopy (SEM) images, and subcritical N₂ adsorption. The new technologies can be used to quantify and compare the results with other more conventional methods in order to improve our understanding of the pore structure of mudrock at a range of spatial scales. I integrate multiple techniques to characterize the pore system structures of the Marcellus Shale reservoir and improve our understanding of the evolution of organic-matter pores through lithology, richness of organic matter, and thermal maturity.

ACKNOWLEDGEMENTS

I would like to express my gratitude to my adviser, Dr. Timothy Carr, for his guidance and mentorship, as well as his generous support of my Ph.D. education. He gave me independence and freedom in my research, and guided me towards my goal. I have learned a lot from him, not only professionally, but also the importance of communication and cooperation. It was a pleasure collaborating and problem solving with Tim. Thank you, Tim, for being such a supportive mentor!

Thanks to the staff and faculty of the Department of Geology and Geography for all the help. Special thanks to the members of my committee, including Dr. Amy Weislogel, Dr. Shikha Sharma, Dr. Tim Warner, and Dr. Ebrahim Fathi at West Virginia University, for helping me with my dissertation.

I would like to recognize Dr. Graham Andrews and Dr. Qin He (Saint Francis University) for countless discussions about interviewing for an academic job. Also, thanks to Dr. Jaime Toro for helping me improve my teaching skills.

It is my great pleasure to be part of a vibrant research group composed of so many fantastic friends and colleagues: Cole Bowers, Chloe Wonnel, Joseph Filchock, Shuvajit Bhattacharya, Zhi Zhong, Yixuan Zhu, Payam Kavousi, Vikas Agrawal, Brittany Hupp, Ruiqian Chen, Fei Shang, and Haibin Di also offered a lot of helps. Special thanks to Keithan Martin and Tom Paronish for countless dynamic discussions and help editing my writings.

I would also like to thank Dr. Derrick Banerjee, Dr. Konstantinos Sierros, and Flexible Electronics for Sustainable Technologies (FEST) lab in the Mechanical and Aerospace Engineering Department of West Virginia University for offering the N₂ adsorption instrument.

Stepping into a career is an important process, yet challenging. The EQT summer internship program provided a great platform for me to gain valuable industrial experiences. Thanks to my mentors and managers at EQT Production, Travis Warner, Ashley Douds, Craig Eckert, Joe Morris, Chris Willian, Randy Blood, for introducing me to the industrial world during my internships. They motivated me to see the application side of the geosciences, introduced me to the real-world problems, and taught me how to present in a way that would be accessible to the audience with a broad background.

The research undertaken in this study was funded through the U. S. DoE National Energy Technology Lab as part of their Marcellus Shale Energy and Environmental Laboratory (MSEEL) (DOE Award No.: DE-FE0024297). The Energy Corporation of America (now Greylrock Energy) and Petroleum Development Corporation provided the cores, wireline logs, and core analysis data. Ingrain provided the SEM images. I also thank IHS (Petra) and NIH (ImageJ, Fiji) for providing the access to the software used in this study.

Above all, I would like to thank my family for always believing in me and encouraging me.

Dedicate to the love and memory of my grandmother Peilan Wang.

Sincerely,

Liaosha Song

Morgantown, West Virginia

United States of America

TABLE OF CONTENTS

ABSTRACT	ii
ACKNOWLEDGEMENTS.....	iii
TABLE OF CONTENTS.....	v
LIST OF FIGURES	ix
LIST OF TABLES.....	xvii
Chapter I.....	1
<i>An Efficient, Consistent, and Trackable Method to Quantify Organic Matter Hosted Porosity from Ion-milled SEM Images of Mudrock</i>	<i>1</i>
Abstract.....	2
Introduction.....	2
Data and methods.....	9
Image analysis workflow	10
Segmentation of the pore space	10
Segmentation of the organic matter	14
Determining porosity associated with organic matter and minerals	18
Results.....	20
Discussion.....	25
Sensitivity test.....	25
Challenges.....	27
Manual picking vs. automatic picking	28
Artifacts.....	29

Image analysis of OM and porosity	30
Conclusions.....	31
Reference Cited.....	34
Chapter II	49
<i>Depositional Environment and Impact on Pore Structure and Gas Storage Potential of Middle Devonian Organic Rich Shale, Northeastern West Virginia, Appalachian Basin.....</i>	
Abstract	49
Introduction.....	50
Methods	51
Results and Discussion	53
Conclusions.....	55
Reference Cited:.....	69
Chapter III.....	70
<i>Porosity and Storage Capacity of Middle Devonian Shale Across a Maturation Gradient.....</i>	
Abstract	86
1. Introduction.....	87
2. Materials and Methods.....	87
2.1 Materials	90
2.2 Subcritical Nitrogen Adsorption	90
2.3 Porosity	93
2.4 Mineralogical Composition.....	94
2.5 Additional Data	94
3. Results.....	94
3.1 Mineralogy, Total Organic Carbon, and Porosity	95

3.2 Nitrogen Adsorption	98
4. Discussion	102
4.1 Relationship between pore structure parameters.....	102
4.2 Relationships between pore structure and TOC.....	103
4.3 Relationships between pore structure and minerals	106
4.4 The relationship between thermal maturity and pore structure.....	108
Conclusions.....	110
Reference Cited:.....	111
Chapter IV.....	127
<i>The Pore Structural Evolution of Mudrock: A Case Study of the Mahantango and Marcellus</i>	
<i>Shales, Appalachian Basin.....</i>	<i>127</i>
Abstract.....	128
Introduction.....	129
Geologic Setting.....	132
Methods	133
Sampling	133
SEM	135
Subcritical Nitrogen Adsorption	139
X-ray Fluorescence (XRF).....	140
TOC Calculated from Petrophysical Well-logs	140
Results.....	142
Total Organic Carbon and Thermal Maturity	142
Mineral-hosted pores	143
OM-hosted pores.....	146
Compaction.....	147

Stratigraphic distribution of pore micro-textures.....	150
Pore surface area, pore volume, and pore size distribution.....	154
Discussion.....	157
Data validation.....	157
Mineralogy and Porosity.....	158
Organic Matter and Porosity.....	160
Stratigraphic Distribution of Pores.....	165
Thermal Maturity and Development of OM Hosted Pores.....	168
Sponge Model, Mechanism of OM-porosity Development.....	169
Mapping sorption storage capacity and free-gas storage capacity from well logs.....	170
Conclusions.....	172
Reference Cited:.....	175
Summary.....	191

LIST OF FIGURES

Figure 1-1. (A) Locations of the three study wells. Contours depict regional averages of vitrinite reflectance (Modified after Zagoriski et al., 2012). (B) Overview of the SEM area, the red rectangle indicates the locations of the smaller field of view SEM images. (C) sample SE2 SEM image illustrating major rock facies (high density minerals, organic matter, pore space) seen in SEM image of shale. The remainder of the image is the inorganic mineral matrix of mudrock, which typically has a density between 2 to 3 g/cc.

Figure 1-2. (a) (b) Examples of image analysis problem types in binarization, which are uneven illumination and stain problem or mixed graphics (from Sauvola and Pietikainen, 2000). (c) a sample image featuring the local variance of grayscale of pores. (d) Grayscale profile of AA', the dash line is the optimal thresholding line. Notice the optimal threshold changes along the profile. The Location of AA' is shown in (c).

Figure 1-3. Local threshold window radius and segmentation result (porosity).

Figure 1-4. Illustration of the pore segmentation on test sample: (a) (from Well CS1, 7133.75 ft. (2174.37 m), Marcellus Formation), (b) (from Well G55, 7162.45 ft. (2183.11m), Marcellus Formation), and (c) (from Well A1, 7620.10 ft. (2322.61 m), Mahantango Formation). (a1), (b1), and (c1) are original images. (a2), (b2), and (c2) are manually picked results with yellow outlines

highlighting the pore borders. (a3), (b3), and (c3) are automatic thresholding results using the proposed method.

Figure 1-5. Illustration of applying Otsu thresholding to segment the OM. Gray-level histograms are listed next to the original image and segmented OM. The blue dash line indicates the postulated optimal segmentation strategy.

Figure 1-6. Illustration of the OM segmentation on test sample d (from Well G55, 7201.10 ft. (2194.90 m), Marcellus Formation), e (from Well CS1, 7136.85 ft. (2175.31 m), Marcellus Formation), and f (from Well A1, 7729.50 ft. (2355.95 m), Marcellus Formation). (d1), (e1), and (f1) are original images. (d2), (e2), and (f2) are manually chosen results with blue outlines indicating the OM borders. (d3), (e3), and (f3) are automatic thresholding results using the proposed method.

Figure 1-7. Processes of filling pore space within segmented OM. X stands for the radius of dilation. Pores fully enclosed by OM can be filled directly. For OM that has pores on the edge, it needs to go through Dilate by X (number of pixels), Fill Holes, then Erode by X. The infilled pores will not be affected by the erosion. The demonstration is not associated with a specific scale, because it can be applied to a range of scale.

Figure 1-8. Correlation between organic matter captured by SEM images and bulk rock total organic carbon.

Figure 1-9. Application of the proposed workflow on an independently supplied image. (1) original image, (2) automated pore segmentation with red outlines highlighting the border of pores, yellow and blue arrows depict the difference between manual and automated segmentation, see detailed discussion in the text; (3) pores manually segmented by an independent third party; (4) automated segmented OM. Image courtesy of Dr. Guochang Wang.

Figure 1-10. Illustration of proposed workflow on a test image (from Well CS1, 7114.50 ft., 2168.50 m).

Figure 1-11. Input image quality and segmentation results (porosity). Solid lines are automatic thresholding (AT) results, while dash lines are manual picking (MP) results.

Figure 1-12. Comparing SEM visible porosity and GRI porosity.

Figure 2-1: The Map shows the location of wells in West Virginia and Pennsylvania used in this paper, and the thermal maturity trend of the Marcellus Shale (modified after East et al., 2012).

Figure 2-2. BJH pore-size-distributions of 5 samples degassed using 5 different temperatures.

Figure 2-3. Isotherms of samples from MIP-3H.

Figure 2-4: Pore size distribution of the samples across Tully Limestone, Marcellus Shale, and Onondaga Limestone with regard to the TOC weight percent.

Figure 2-5: XRD data from well MIP-3H (in volume %) illustrating the mineralogical variations of the Marcellus Shale.

Figure 2-6: The relationship between BET specific surface area and TOC.

Figure 2-7: The relationship between BJH pore volume and TOC.

Figure 2-8. Geochemical and well-log profiles of the MIP-3H core illustrating corrected gamma ray (CGR), true resistivity (RT), SRA TOC (CORE_TOC), ratio of thorium to uranium (Th/U) derived from spectral gamma ray, TOC calculated from uranium log (TOC_URAN), phosphorus, aluminum, vanadium and chromium derived from XRF (XRF_P, XRF_AL, V+CR), and NMR log.

Figure 3-1. Locations of the four study wells.

Figure 3-2. Stratigraphy of the study area

Figure 3-3. Mineralogical composition of shale samples in volume percentage, data from Table 2.

Figure 3-4. Nitrogen adsorption isotherms of samples.

Figure 3-5. Pore size distribution of samples from Mahantango and Marcellus Formations.

Figure 3-6. Relationships between total organic carbon (TOC) content and (A) average pore width, and (B) median pore size.

Figure 3-7. Relationship between specific surface area, pore volume, and TOC. Data points in green shadow are from Mahanntango Fm., while yellow shadow covers the Marcellus samples.

Figure 3-8. Relationship between TOC and (A) median pore size, and (B) GRI porosity.

Figure 3-9. Relationships between clay content and (A) specific surface area, and (B) pore volume.

Figure 3-10. Relationship between thermal maturity (represented by vitrinite reflectance) and specific surface area.

Figure 4-1. Locations and thermal maturity (as of vitrinite reflectance, R_o) of the three study wells, and the stratigraphic column of Middle Devonian in study area.

Figure 4-2. Imaging workflow (sample from well CS1, 7136.85 ft., % R_o =2.79).

Figure 4-3. Types of mineral-hosted pores. A) Inter-particle pores, samples from well CS1, 7133.75 ft. (2174.37m); B) Intra-particle pores, sample from well A1, 7702.65 ft. (2347.77m); C) Inter-particle pores hosted by clay platelets, sample from well A1, 7620.10 ft. (2322.61m); D) Inter- and Intra-particles hosted by pyrite framboids, sample from well CS1, 7082.40 ft. (2058.72m).

Figure 4-4. Correlation between source rock analysis (SRA) TOC and Uranium from spectral gamma ray from core scanning.

Figure 4-5. A) Dissolution pores along margins of carbonate grains. Blue arrows point to dissolution porosity, and yellow arrows point to original dissolution porosity filled by secondary OM. Sample from well CS1, 7114.50 ft. (2168.50m). B) Triangular pores hosted by clay platelets (phyllosilicate grains). Blue arrows point to inter-particle porosity (phyllosilicate porosity), yellow arrows point to phyllosilicate porosity filled by secondary OM. Sample from well CS1, 7036.00 ft. (2144.57m).

Figure 4-6. OM pore types. A) Spongy pores within a piece of secondary OM, sample from well CS1, 7133.75 ft. (2174.37m); B) Complex OM pores hosted by OM associated with minerals,

porous nature of OM is demonstrated by the inner structure of OM. Sample from well CS1, 7058.45 ft. (2151.42m); C) OM pores within secondary OM. Pore size varies significantly. Sample from well G55, 7141.25 ft. (2176.65m); D) Bubble porosity hosted by OM. Sample from well A1, 7720.65 ft. (2353.25m); E) Open fractures within OM and minerals, sample from well A1, 7547.30 ft. (2300.42m); F) OM pores within secondary OM. Pore size varies significantly. Sample from well CS1, 7114.50 ft. (2168.50m).

Figure 4-7. Images demonstrating compaction. A) Clay and mica bend around pyrite framboid and other mineral grains. Sample from well A1, 7729.50 ft. (2355.95m). B) Compactional bending of clays around more rigid grains. Sample from well G55, 7141.25 ft. (2176.65m). C) Clays bend around pyrite framboids, green dash line marking the pressure surrounding pyrite framboids. Sample from well CS1, 7082.40 ft. (2158.72m). D) compression of a vertically oriented phyllosilicate grain produced pores because of splits between phyllosilicate sheets. Sample from well CS1, 7133.75 ft. (2174.37m).

Figure 4-8. Typical SEM images for four different pore micro-facies in the Marcellus Shale. A: organic rich, sample from well A1, 7729.50 ft.; B: organic lean, sample from well G55, 7084.10 ft.; C: clay rich, sample from well A1, 7620.10 ft.; D: carbonate rich, sample from well A1, 7778.15 ft.

Figure 4-9. Pore size distribution from BET analyses calculated by BJH model. Data series are color coded by TOC value of the sample. Warmer color represents higher TOC.

Figure 4-10. OM recognized from SEM images plots against BET specific surface area (SSA) and BJH pore volume.

Figure 4-11. Total organic carbon (TOC) in weight percentage plotted against organic matter (OM) recognized from SEM images. The strong positive correlation indicates a good representativeness of the SEM images.

Figure 4-12. SEM images illustrating large pieces of OM with no SEM-visible porosity. Sample A came from well A1, 7729.50 ft., and sample B came from well G55 7217.40 ft.

Figure 4-13. Negative correlation between SEM-visible porosity and organic matter. As richness of OM increases, less pores are visible under SEM. However, BET analysis shows that organic-rich samples have substantial amount of pores smaller than 10 nm.

Figure 4-14. The correlation between transformation ratio (TR) and OM volume%. TR is defined as porosity in organic matter divided by whole area OM covered and the voids in it. We use this index to describe the extent of development of OM pores. Notice the weak negative correlation between them.

Figure 4-15. A) Positive correlation between TOC and BET specific surface area; B) negative correlation between bulk density and normalized pore volume.

Figure 4-16. Cross-section illustrating the sorption storage capacity change through different horizons in Marcellus Formation.

Figure 4-17. Cross-section illustrating the free-gas storage capacity change through different horizons in Marcellus Formation.

LIST OF TABLES

Table 1-1. Comparison of Manual picking results with automatic threshold result. Images from a to f are listed in Figure 1-4 and Figure 1-6.

Table 2-1 Sample preparation procedures used in previous research (Devonian-Mississippian (D-M); Formation (Fm.))

Table 2-2 Summary of outgassing conditions by material type (Olson, 2012)

Table 2-3. Low-pressure N₂ adsorption test and TOC results

Table 3-1. Vitrinite reflectance (R_o), total organic carbon (TOC) content, depth, and formation of shale samples

Table 3-2. Mineralogy Composition of Shale Samples in Volume Percentage.

Table 3-3. Bulk density, grain density, and GRI porosity of shale samples.

Table 3-4. Pore structure parameters determined via N₂ adsorption.

Table 4-1. Sample locations, Formations, and total organic carbon (TOC).

Table 4-2. Results of TOC measurements and vitrinite reflectance (R_o).

Table 4-3. XRF analysis (normalized to mineralogical composition) of Mahantango Formation and Marcellus Shale.

Table 4-4. Porosity Measurement from digitalized Scanning Electron Microscopy (SEM) Images. OM: organic matter, TR: transformation ratio.

Table 4-5. Porosity, OM, porosity in OM, and transformation ratio (TR) of four pore-micro-texture-facies.

Table 4-6. Test results of subcritical nitrogen adsorption. Specific surface area (SSA) is based on BET model, micropore area and volume are based on t-plot method, and pore volume is based on BJH model.

Chapter I

An Efficient, Consistent, and Trackable Method to Quantify Organic Matter Hosted Porosity from Ion-milled SEM Images of Mudrock

Liaosha Song¹, Travis Warner², Timothy Carr¹

1. Department of Geology and Geography, West Virginia University, Morgantown, WV, 26506

2. 30 Micrometers Consulting, LLC, Pittsburgh, PA, 15222

Accepted for publication by AAPG Bulletin

Abstract

To accurately quantify pore space and organic matter from two-dimensional scanning electron microscope (SEM) images, an efficient and consistent workflow using adaptive local thresholding, Otsu thresholding and Image Calculator is presented. The new workflow offers an automated segmentation of pore space and organic matter, and then differentiates the porosity hosted by organic matter and minerals. The workflow is demonstrated on a widely-distributed set of core samples from Mahantango and Marcellus shale units of the Appalachian basin. The vitrinite reflectance (R_o) of these samples ranges from 1.36% to 2.89%, covering a spectrum of thermal maturity. Organic matter (OM) abundance and mineralogy also vary significantly. The results are compared with routine rock-property-tests, such as helium porosimetry (Gas Research Institute (GRI) method) and total organic matter. The proposed workflow improves quantitative determination of porosity and organic matter in shale samples. Advantages of this workflow include improved accuracy, consistency and speed of analysis of SEM images of shale samples at the nano-scale.

Introduction

The exploration and exploitation of shale-gas reservoirs has attracted global interest in this fine-grained rock type. Shale gas production in the US increased from 0.8 trillion cubic feet (TCF) in 2000 to 16.76 TCF in 2017, and will account for nearly three-quarters of natural gas production by 2050 (EIA, 2018). Porosity, pore structure, organic matter abundance, grain assemblage composition, and thermal maturity are key factors in assessing shale gas resources and reserves, and understanding storage capacity and long-term producibility of a shale-gas reservoir. Shale, or more correctly mudrock (mudstone), has long been considered as seal or

source rock because of its low permeability and tendency to be associated in the geologic record with preserved organic matter.

One reason that makes a mudrock reservoir “unconventional” is that conventional drilling techniques are not successful in hydrocarbon production due to the nano-scale pore sizes. Characterization of nano-meter (nm) pores in a mudrock reservoir requires a high-resolution technique to show the fine-scale properties. Compared to other technologies such as mercury injection capillary pressure (MICP), physical adsorption, nuclear magnetic resonance (NMR), and helium porosimeter, scanning electron microscopy (SEM) provides a direct visual observation of the complex microstructure of a mudstone reservoir, which has a good potential to decipher the heterogeneity of pore geometry and grain assemblage (Dilks and Graham, 1985; Katz and Thompson, 1985; Jarvie et al., 2007; Loucks et al., 2009, 2012; Ross and R. Mark Bustin, 2009; Schieber, 2010, 2013; Sondergeld et al., 2010; Curtis and Ambrose, 2011; Slatt and O’Brien, 2011, 2013; Walls and Diaz, 2011; Klaver et al., 2012, 2015; Passey et al., 2012; Curtis et al., 2012; Fishman et al., 2012; K. L. Milliken et al., 2012; Bohacs et al., 2013; Milliken et al., 2013, 2014; Dong and Harris, 2013; Giffin et al., 2013; Pommer and Milliken, 2015; Lazar et al., 2016; Milliken and Olson, 2016; Nole et al., 2016). SEM images can also illustrate the distribution of resolvable porosity associated with organic matter (OM) and minerals. Quantification of nano- to micro-porosity is important for evaluating the storage capacity and flow-regime in unconventional reservoirs.

SEM has been exploited in various industries due to its potential high magnification and ability to resolve fine-scale features. Unlike optical microscopy, SEM uses an electron beam to scan the sample surface, and generates images by recording the interaction of the electron beam with atoms of the specimen at various depths within the sample. Several types of electrons are

generated (e.g. secondary electrons (SE), backscattered electrons(BSE), etc.), and they differ from one another in origin, energy, and travel direction, and provide distinguishing structural information about the sample (Huang et al., 2013).

Improved physical processing of samples has provided a significant improvement in SEM analysis of mudrock. With mechanical polishing, quantitative analysis of shale is nearly impossible, because numerous artificial pores are created due to sample breakage (Loucks et al., 2009). Ion milling technique uses a beam of ions to very precisely mill a sample. By carefully controlling the energy and intensity of the ion beam, a flat surface at the nano-scale is produced, resulting in removal of topographic artifacts and producing clearer imaging of pore structures and mineral textures (Erdman and Drenzek, 2013). The extremely low-relief surface sheds new light on the nano-scale microstructure and evolution of pores contained within the organic matter and inorganic mineral-matrix of mudrock-reservoirs (e.g. Loucks et al., 2009, 2012; Ambrose et al., 2010; Sondergeld et al., 2010; Curtis and Ambrose, 2011; Slatt and O'Brien, 2011; Curtis et al., 2012; Milliken et al., 2013, 2014). However, ion milling can create some artifacts such as curtain effects, and redeposition of milled minerals. Other artifacts include mineral precipitation after sample preparation and post-coring precipitations (Milliken and Olson, 2016). Most of these artifacts are easy to recognize (Loucks et al., 2012; Anovitz and Cole, 2015; Milliken and Olson, 2016). Nole et al. (2016) published a method to circumvent the artifacts created during ion milling utilizing the differences in circularity values in a segmented image.

On SEM (especially SE1 or SE2) images, pore space is defined by very low grayscale values, whereas minerals' surfaces have higher grayscale values (Hemes et al., 2013) (Figure 1-1). Quantitative image analysis of organic-rich shale uses thresholding and segmentation of pore space and OM from SEM images, but is challenging, because the process of image segmentation

does not necessarily lead to a unique solution. On the one hand, the variation of instrument settings can cause grayscale level shifts from some images to others. Even within a single image, the characteristic gray-scale value of organic matter, minerals, and pores can vary (Anovitz and Cole, 2015) (Figure 1-2). On the other hand, imaging artifacts, especially edge effects at pore boundaries, make it hard to choose an appropriate segmentation algorithm (Kelly et al., 2016).

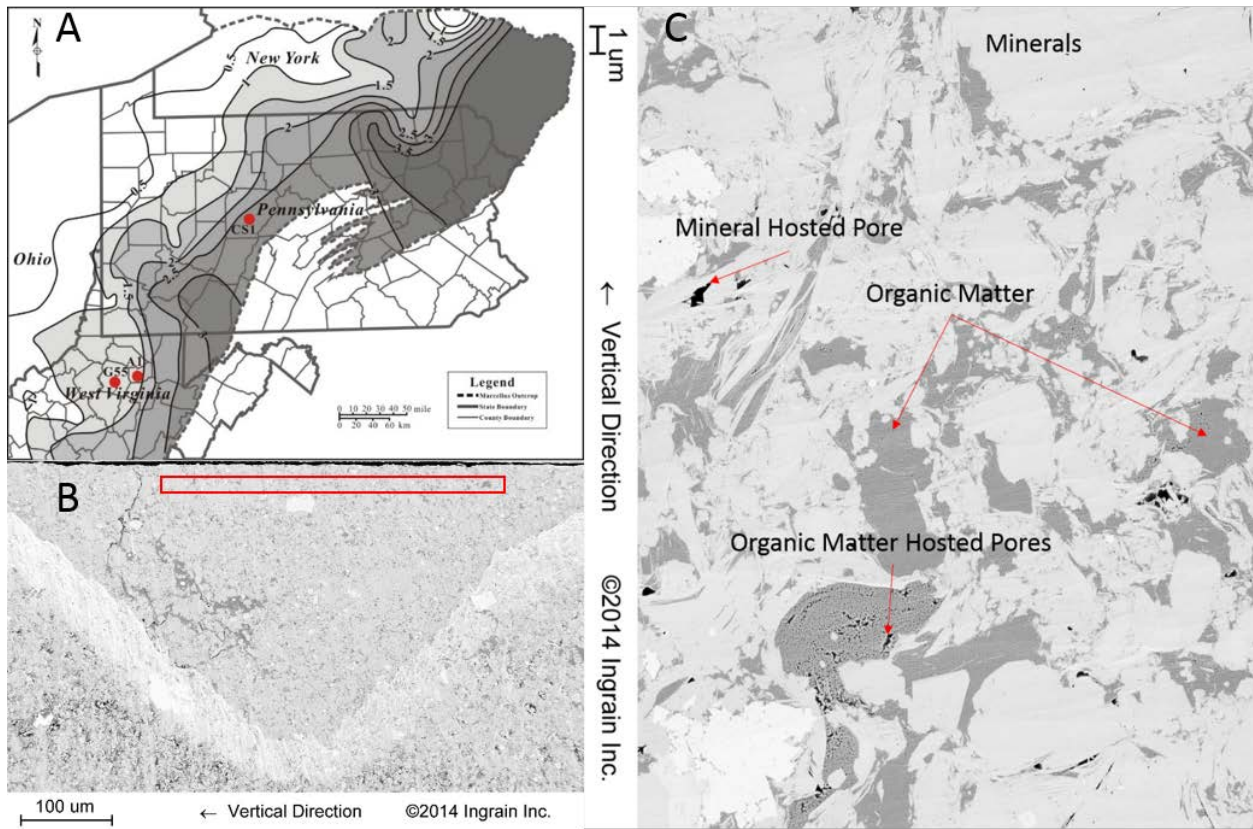


Figure 1-1. (A) Locations of the three study wells. Contours depict regional averages of vitrinite reflectance (Modified after Zagoriski et al., 2012). (B) Overview of the SEM area, the red rectangle indicates the locations of the smaller field of view SEM images. (C) sample SE2 SEM image illustrating major rock facies (high density minerals, organic matter, pore space) seen in SEM image of shale. The remainder of the image is the inorganic mineral matrix of mudrock, which typically has a density between 2 to 3 g/cc.

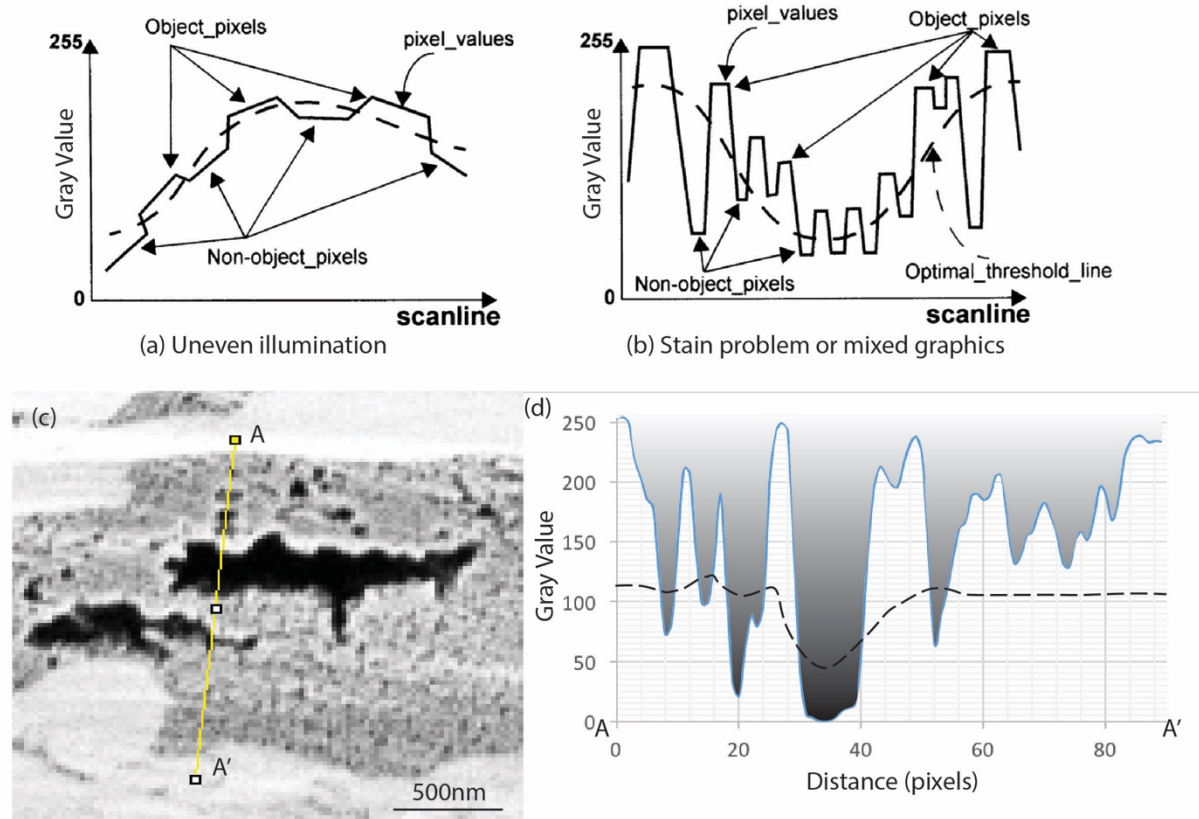


Figure 1-2. (a) and (b) Examples of image analysis problem types in segmentation, which are uneven illumination and stain problems (from Sauvola and Pietikainen, 2000). (c) a sample image featuring the local variance of grayscale of pores. (d) Grayscale profile of AA', the dashed line is the optimal threshold line. Notice the optimal threshold changes along the profile. The Location of AA' is shown in (c).

There is more than one way to seek an appropriate thresholding method to segment a 2D image (or a 3D volume). Manual thresholding, one in which the operator searches the whole range of grayscale (for 8-bit image, the range is from 0 to 255) and locates a specific threshold that contains most of the foreground pixels. Zhang et al. (2011) explored the lack of consistency with manual thresholding by systematically studying the effect of different thresholds on the pores. They tested a gray scale range from 10 to 100, and set 45 to 65 as the range that gave the best results. But even within this range, the estimated porosity varied from 4% to 13% (Zhang et al., 2011). Automated thresholding is preferable not only because it saves time, but it reduces potential human bias or subjectivity and increases consistency (Wildenschild and Sheppard, 2013). Hemes et al. (2013) used a combination of thresholding and Sobel-edge-detection algorithms to segment the pores, then used ArcGIS to manually correct the inaccurate pore segmentations (see also Klaver et al., 2015, 2016). The methodology proposed by Hemes et al. (2013) involves a large amount of manual correction of the segmentation, so it is very time-intensive when dealing with large SEM images. Kelly et al. (2016) employed a comprehensive image analysis workflow. They compared two different image segmentation methods. One is a fuzzy logic, membership-function based, c-means centroid search “soft thresholding”. The other is histogram-based thresholding with implementation of a level-set method. In many cases, the level set contours caused overestimation of the OM hosted porosity. Neither image segmentation method provided large enough connectivity. A consistent, efficient and trackable method of image analysis with high accuracy is very much needed for nano-scale porosity typical of mudstones.

Sezgin and Sankur 2004 reviewed 40 different image thresholding methods, and classified them into 6 categories based on the information they exploited: histogram shape, clustering,

entropy, object attribute, spatial methods and local methods (Sezgin and Sankur, 2004). Zhang et al. (2011) recommended using top-hat segmentation. This algorithm picks up peak or valley based on a local criterion. Yet a threshold still needs to be chosen, and for the estimated gray-scale range discussed above (45 to 65), the porosity results varied from 7% to 3.5%. Because of the local variance we noticed in our images (Figure 1-2) and other images that have been published over the years, we hypothesize that local thresholding that adapts the threshold value on each pixel to the local image characteristics is more promising than global thresholding (Sezgin and Sankur, 2004).

Currently, there is no standard workflow for acquiring petrophysical properties (e.g. porosity, organic matter richness) from SEM images of organic-rich shale. We introduce a workflow for quantitative SEM-image analysis that improves consistency and efficiency of results, and demonstrate the applicability of the workflow for investigating pore structure and OM character. The resulting quantification can contribute to improving our knowledge about heterogeneity of pore systems and organic matter in mudrock, and other fine-grained rocks and to better understand heterogeneity's role in controlling the reservoir properties in oil and gas exploration and production.

Critical questions to address in quantitative image analysis of organic-rich mudrock are (1) how to select a non-biased threshold to segment pore space and OM from SEM images, and (2) how to separate OM hosted pores from the whole pore system? An additional but critical question choosing the right representative elementary area (REA), is beyond the scope of this paper. However, before one can address the choice of REA, we need to make sure our segmentation of each image is consistent. These questions illustrate a common challenge associated with image analysis: reproducibility, usually addressed subjectively by the operator,

buy can be subject to bias and inconsistency. We test this workflow with our own samples and an image donated by Dr. Guochang Wang from St. Francis University, by comparing our results with a reference dataset derived from manual pore picking.

Data and methods

Data for this research consists of 32 core samples collected from three wells penetrating the Mahantango and Marcellus formations in the Appalachian basin. Samples range in depth from 7015.00 ft. to 7778.15 ft. (2166 to 2349m) (Figure 1-1 A). For this study, the core samples were ion-polished at Ingrain's Digital Rock Physics lab with a Gatan Ilion+ Argon Ion polishing system. No conductive coatings were applied to the milled surfaces. An area approximately 1 millimeter by 500 micrometers is polished. A 2D SEM overview image is taken with a field of view of approximately 750 micrometers. The red rectangle within the overview indicates where the smaller field of view 2D SEM images were acquired (Figure 1-1 B). Approximately 10 locations per sample were imaged with Carl Zeiss SEM systems at a low beam energy of 1 keV. Both backscatter electron (BSE) and secondary electron (SE2) detectors are used to capture images. Images from Well A1 and G55 are taken at resolution of approximately 15 nm/pixel, while images from Well CS1 are taken at resolution of 10 nm/pixel. All samples were viewed perpendicular to bedding (Figure 1C). SE2 SEM images are used in this research. SEM images were processed with ImageJ and Fiji (Schindelin et al., 2012, 2015; Schneider et al., 2012). Median filter was applied before quantification to reduce the noise in the images (Gallagher and Wise, 1981; Culligan et al., 2004, 2006; Kelly et al., 2016; Nole et al., 2016).

The surface of the testing sample was prepared by an Ar-ion polisher with a Jeol IB-09020CP, and coded with Pt. The image was acquired by concentric backscattered detector using

an FEI Helios Nanolab 600i. The working distance was 3.3mm, and the image was acquired at an accelerating voltage of 8kV.

Total organic carbon (TOC) content was quantified using the source rock analyzer (SRA), and the results were expressed in weight percentage. Organic matter abundance values in volume percent is typically calculated as the volume percent of OM calculated from the bulk TOC (wt. %) by assuming an OM density of 1.45 g/cm³ (Milliken et al., 2013).

Image analysis workflow

We illustrate a workflow that automatically thresholds an SEM image by adaptive local thresholding (Phansalkar thresholding) and Otsu thresholding. Then, we present a methodology to further segment porosity between organic matter and mineral matrix by Image Calculator (a command in ImageJ or Fiji). All steps are undertaken with Fiji, which is an open-source software developed by the National Institutes of Health (NIH). Every step of the methodology is trackable, so it offers not only a final numeric result, but precision and repeatability. The methodology is a step toward establishing a consistent and objective numerical model of the optically visible nano-scale pore structure of mudrock. Results demonstrate that this method is highly efficient and provides a high degree of accuracy and repeatability in image processing, advancing the study of pore structure of mudrock.

Segmentation of the pore space

Thresholding is the first and most important step of image segmentation. The process of image thresholding does not necessarily yield a unique solution for a threshold value. The main reason is variation in illumination level resulting from different voltage of current, or simply due to different instruments, in which case a single type of rock component (e.g. OM) will show

different absolute grayscale ranges. Therefore, an unchanging thresholding parameter is unlikely to exist, and selecting an appropriate method to find thresholds is of great significance. As humans cannot distinguish different gray scales consistently, choosing thresholds manually introduces subjectivity and uncertainty because of the lack of consistency between operators, and even between instances for the same operator (Anovitz and Cole, 2015).

To address this challenge, we introduce adaptive local thresholding. Sauvola and Pietikainen (2000) published a method that determined a local threshold for each pixel based on local variance and standard deviation. This method was originally designed for document analysis. When there is uneven illumination or stains, global thresholds cannot offer consistent results (Sauvola and Pietikainen, 2000). In certain area, the grayscale of pores is equal to that of OM in other areas, which causes significant error when trying to quantify the porosity (Figure 1-2). This local variance is typically caused by “shallow dipping of a pore boundary”, which results in low grayscale gradients in certain region (Hemes et al., 2013). The optimal threshold strategy is to determine a local threshold for each pixel based on local variance as demonstrated in Figure 1-2 a and b. Phansalkar et al. (2011) applied this method to cytological image analysis, and noticed a problem. When the contrast in the local neighborhood is very low, the relatively dark regions will be removed (categorized as background). In cytological images and SEM images of shales, these dark regions are also foreground. They addressed this problem by using equation 1 to calculate the local thresholds (equation 1):

$$T(x, y) = m(x, y) \left[1 + p e^{-q \cdot m(x, y)} + k \left(\frac{s(x, y)}{0.5} - 1 \right) \right] \quad (1)$$

Where $T(x,y)$ is the local threshold, $m(x,y)$ is the mean, $s(x,y)$ is the standard deviation, and k is a constant which takes values in the range 0.2 to 0.5, p equals 2, and q equals 10 (Phansalkart et al., 2011). In our test, $k=0.5$ gives the best results.

When applying adaptive local thresholding, the operator needs to choose a window size. It gives a limit of the region within which the local threshold will be computed. If the radius is too big, it will operate the same as global thresholding. When it gets too small, the thresholding itself will add to the local variance. Sauvola and Pietikainen (2000) recommend setting the window size to 10 to 20 pixels for images of 75 to 300 dpi (Sauvola and Pietikainen, 2000). So we ran a sensitivity test (Figure 1-3). Figure 1-4 shows the result of manually picked pores vs. automated segmentation.

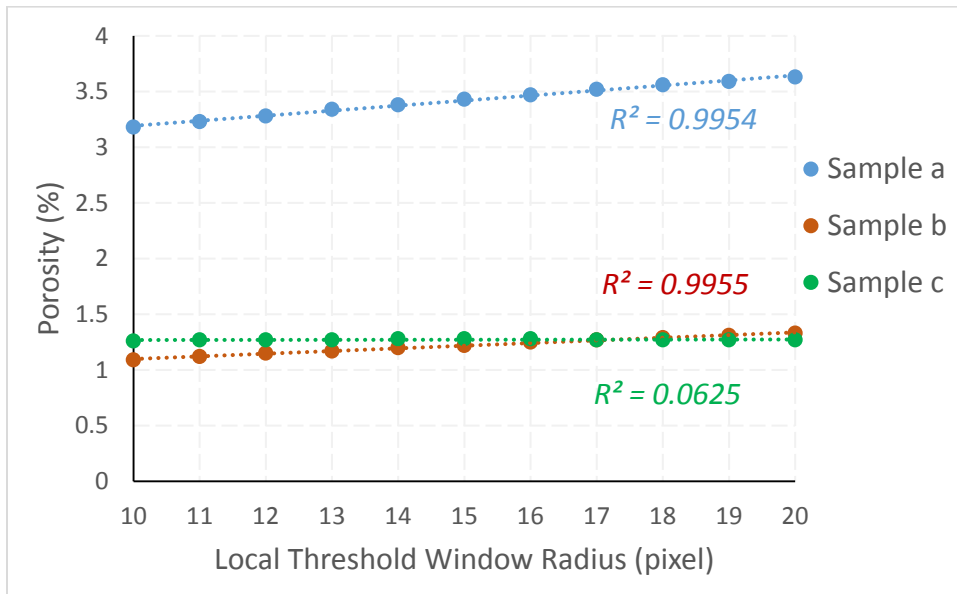


Figure 1-3. Local threshold window radius and segmentation result (porosity).

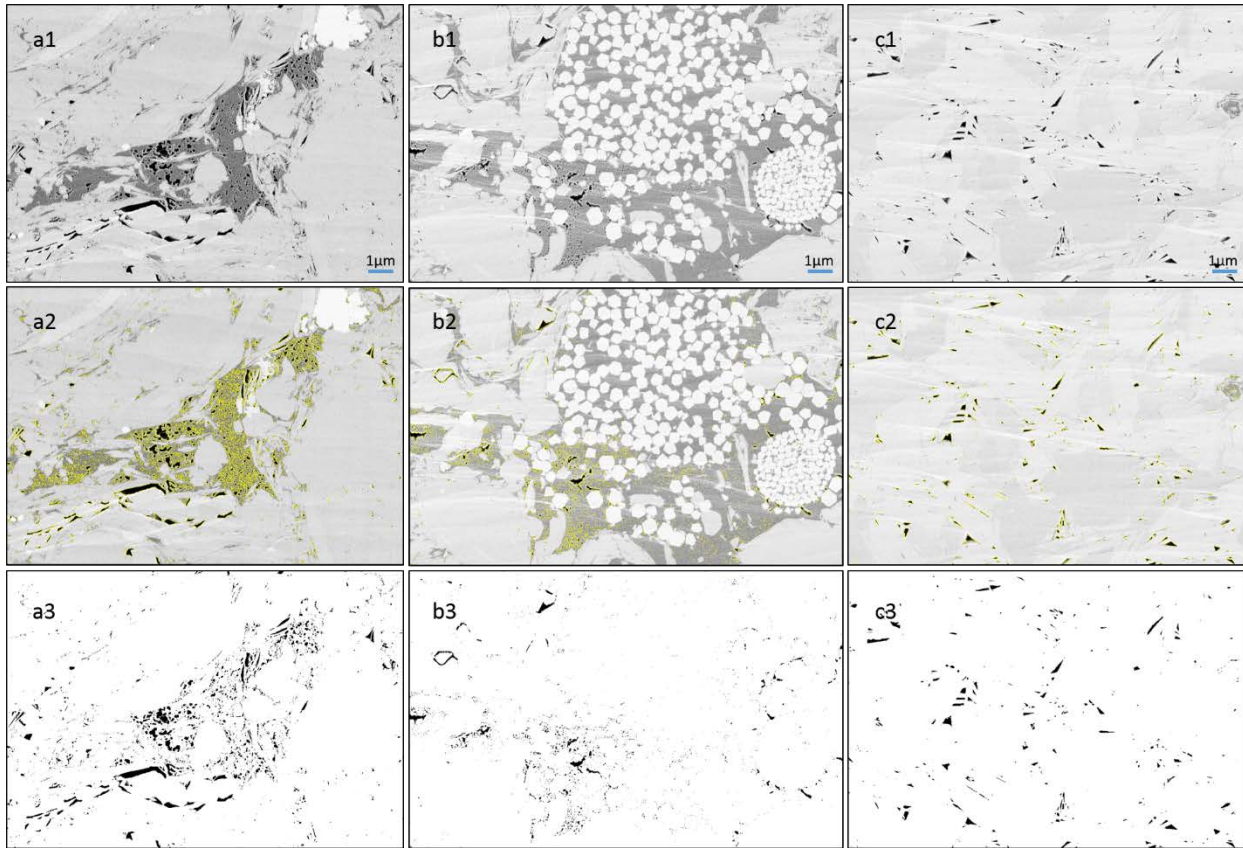


Figure 1-4. Illustration of the pore segmentation on test sample: (a) (from Well CS1, 7133.75 ft. (2174.37 m), Marcellus Formation), (b) (from Well G55, 7162.45 ft. (2183.11m), Marcellus Formation), and (c) (from Well A1, 7620.10 ft. (2322.61 m), Mahantango Formation). (a1), (b1), and (c1) are original images. (a2), (b2), and (c2) are manually picked results with yellow outlines highlighting the pore borders. (a3), (b3), and (c3) are automatic thresholding results using the proposed method.

Segmentation of the organic matter

Otsu's method is used to threshold OM and pore space. This method was developed by Nobuyuki Otsu in 1979 (Otsu, 1979), and it offers automatically perform clustering-based image thresholding. It reduces a grayscale image to a binary image. The algorithm assumes that the image contains two classes of pixels that are distributed in a bi-modal histogram (foreground pixels and background pixels). The optimum threshold is established by minimizing the weighted sum of intra-class variances of the foreground and background pixels, or equivalent (because the sum of pairwise squared distances is constant), maximizing the inter-class variance (Figure 1-5).

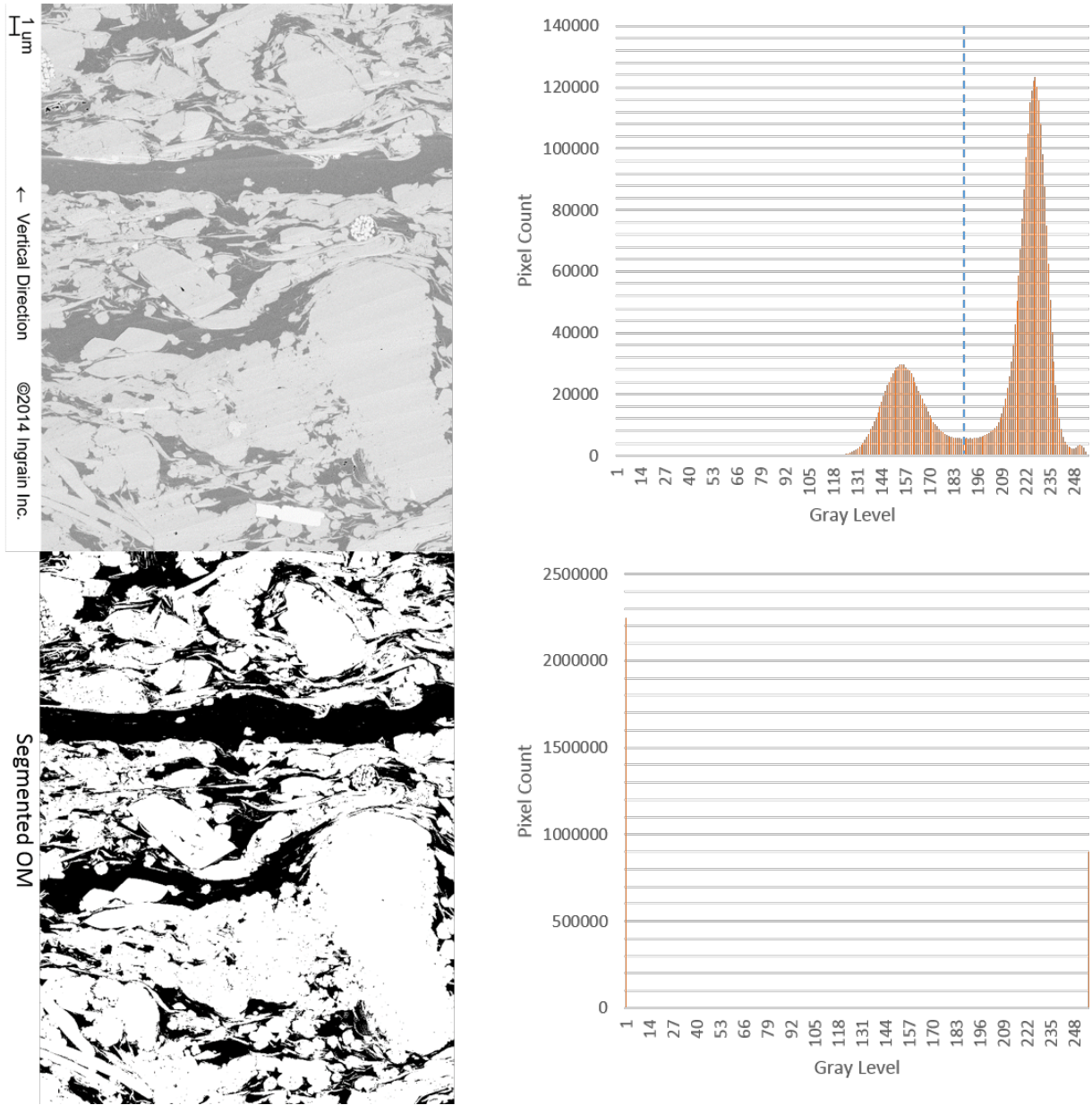


Figure 1-5. Illustration of applying Otsu thresholding to segment the OM. Gray-level histograms are listed next to the original image and segmented OM. The blue dash line indicates the postulated optimal segmentation strategy.

The intra-class variance is defined as a weighted sum of variances of the two classes:

$$\sigma_{\omega}^2(t) = \omega_0(t)\sigma_0^2(t) + \omega_1(t)\sigma_1^2(t). \quad (2)$$

Weights $\omega_{0,1}$ are the probabilities of the two classes separated by a threshold t , and $\sigma_{0,1}^2$ are variances of these two classes. In the shale image, one of the two classes is the darker part of the image, which is organic matter and pore space. The other class is the rest of the input image, which is mineral matrix. Since we already have the pore space segmented, it can be simply subtracted from the Otsu thresholding result with the Image Calculator feature in Fiji or ImageJ, and the OM remains. Figure 1-6 shows the result of manually picked OM vs. Otsu thresholding.

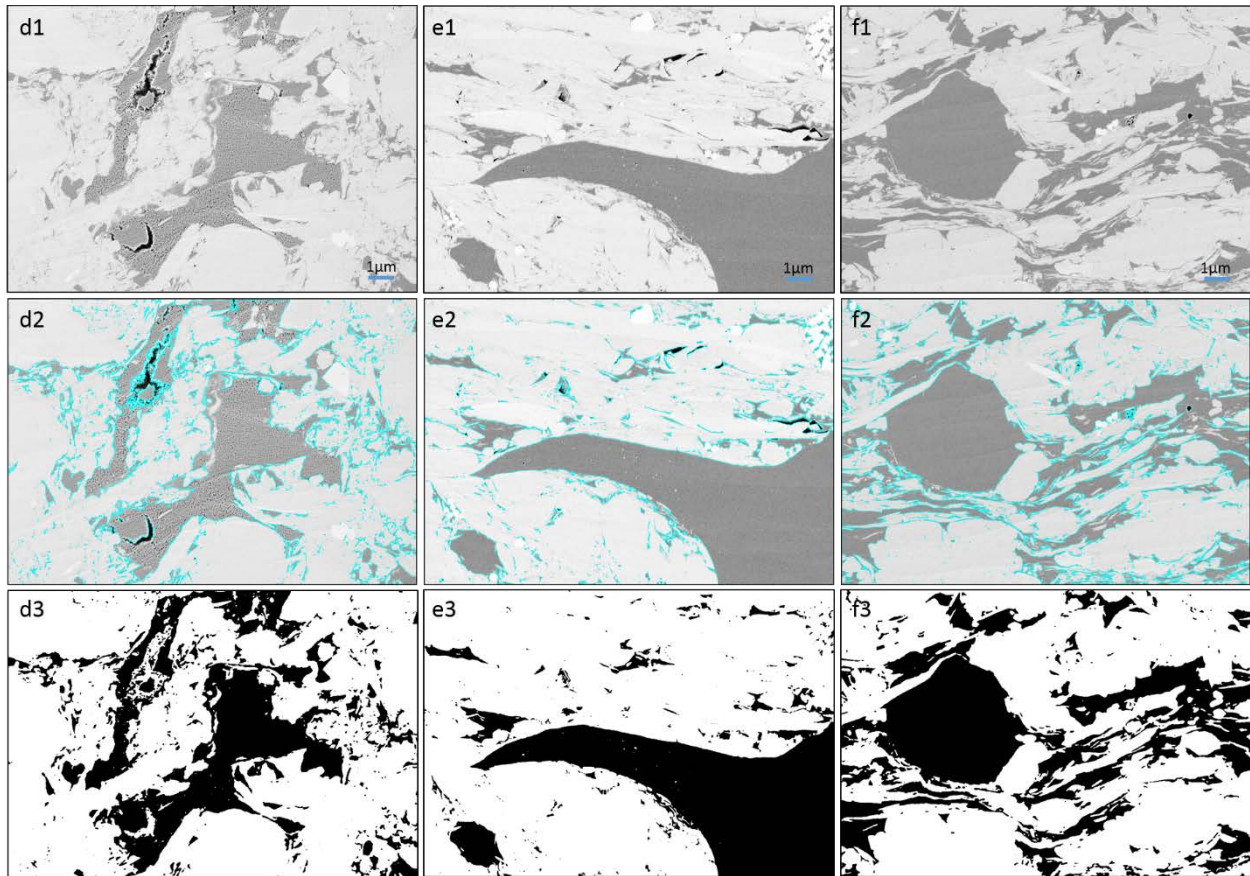


Figure 1-6. Illustration of the OM segmentation on test sample d (from Well G55, 7201.10 ft. (2194.90 m), Marcellus Formation), e (from Well CS1, 7136.85 ft. (2175.31 m), Marcellus Formation), and f (from Well A1, 7729.50 ft. (2355.95 m), Marcellus Formation). (d1), (e1), and (f1) are original images. (d2), (e2), and (f2) are manually chosen results with blue outlines indicating the OM borders. (d3), (e3), and (f3) are automatic thresholding results using the proposed method.

Determining porosity associated with organic matter and minerals

OM hosted porosity in organic-rich shale reservoirs is formed during thermal maturation (e.g. Loucks et al., 2009, 2012; Schieber, 2010, 2013), which is of great significance in evaluating the reservoir and understanding the evolution of pores in shale (e.g. Milliken et al., 2013). Loucks et al. (2012) summarized classification of pore types in shale and presented a classification system featuring interparticle, intraparticle, and OM pores. Milliken et al. (2013) studied the Marcellus Shale and subdivided OM pores into three types. Pommer and Milliken (2015) further defined OM-mineral interface pore as pores between mineral particle and OM, and categorized this as mineral-associated rather than OM-hosted pores. In this research, we will follow the Pommer and Milliken (2015) classification.

If the pores within segmented organic matter (e.g. Figure 1-6 d3, e3, f3) can be digitally infilled, the percentage of OM plus OM hosted porosity can be determined. This can be subtracted from the total pore space map (e.g. Figure 1-4 a3, b3, c3) with Image Calculator. The result is the mineral-hosted porosity. The OM hosted porosity is simply determined by subtracting mineral-hosted porosity from the total porosity.

When trying to infill the void space in OM, there are several different cases. The ideal case is pore space fully enclosed within OM. This type of OM hosted pore can be directly filled with the Fill Holes feature of Fiji or ImageJ. Another case is pores located very close to the border of OM that after segmentation are not fully enclosed in OM. For this pore type, we use the mathematical morphology operation of Dilate in Fiji or ImageJ to add pixels to the edges of OM. By doing so, the gap of open borders of OM can be connected. After that, run Fill Holes and Erode (another feature of Fiji or ImageJ) to remove the same amount of pixels from the edges

(Figure 1-7). This operation can also compensate the bright ring created because of the topographical artifacts and mineral surface charging.

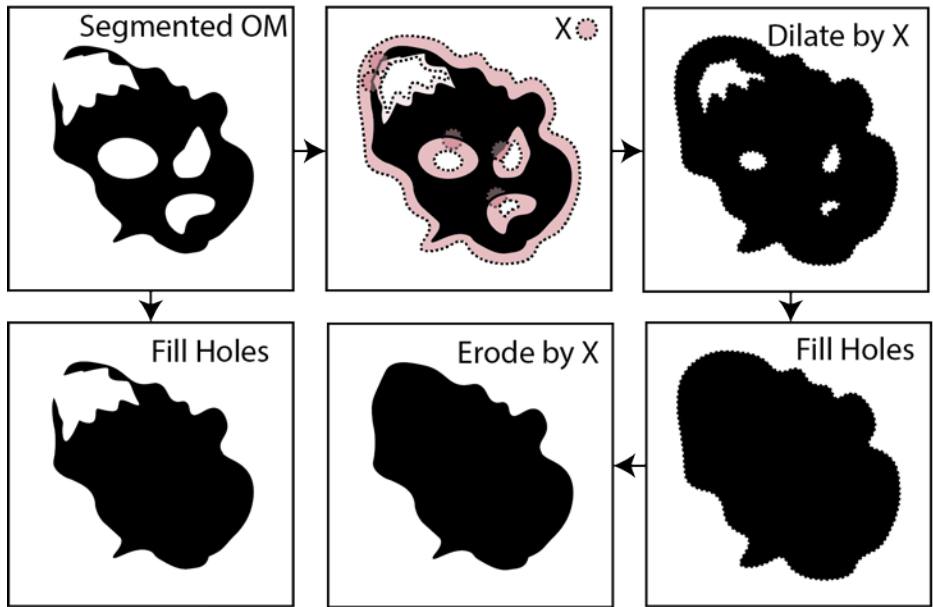


Figure 1-7. Processes of filling pore space within segmented OM. X stands for the radius of dilation. Pores fully enclosed by OM can be filled directly. For OM that has pores on the edge, it needs to go through Dilate by X (number of pixels), Fill Holes, then Erode by X. The infilled pores will not be affected by the erosion. The demonstration is not associated with a specific scale, because it can be applied to a range of scale.

To summarize, the 2D grayscale SE2 SEM image undergoes automatic thresholding and segmentation into several rock components, producing segmented binary-images of pore space and OM. The OM is then digitally infilled. With image calculator, the infilled OM is subtracted from the total pore space map to generate the mineral-hosted pore space map. Mineral-hosted pores can then be subtracted from the total pore space to generate an OM hosted pore map. After segmentation of the image and calculation of the percentage of pore space hosted by OM and minerals, the OM is obtained by simply adding the area of each of the individual components and dividing by the total image area, which can be acquired by Particle Analyzer in Fiji or ImageJ. Subsequent statistical techniques can be applied to each component. In addition, geometric analysis of pores such as fractal dimension, lacunarity and succolarity can be undertaken.

Results

Figure 1-4 demonstrates the segmentation results of three samples. Sample (a) comes from well CS1 and features SE2 image with a substantial backscatter component so that the contrast between minerals, OM, and pores is very vivid. The pore system is a combination of both OM hosted and mineral hosted pores. Sample (b) comes from well G55, and most pores in this image are within OM. Sample (c) comes from well A1, and the pore system is dominated by mineral-hosted pores. Most of the pores are formed by the chaotic stacking pattern of clay particles. Image a2, b2, and c2 are the manual picking results with yellow lines highlighting the pore borders. And image a3, b3, and c3 are the automatic thresholding results. The porosity values from SEM images are plotted where data points consist of an average value of 10 to 15 SEM images.

Figure 1-6 shows the results of OM segmentation in sample (d), (e), and (f). Image d2, e2, and f2 are derived from manual picking OM with blue lines highlighting the OM borders. Image d3, e3, and f3 are automatic thresholding results. The manually picked results are listed as reference dataset in this research, although we have to admit the fact that quantification of SEM images of shales can hardly lead to a result that can be used as ground truth because of multiple reasons we discussed earlier in this paper. The result is compared with TOC in weight percent. Richness of OM from image analysis has a strong positive correlation with TOC (Figure 1-8). The comparison of automatic threshold result with the ground truth (manual picked result) is listed in Table 1-1.

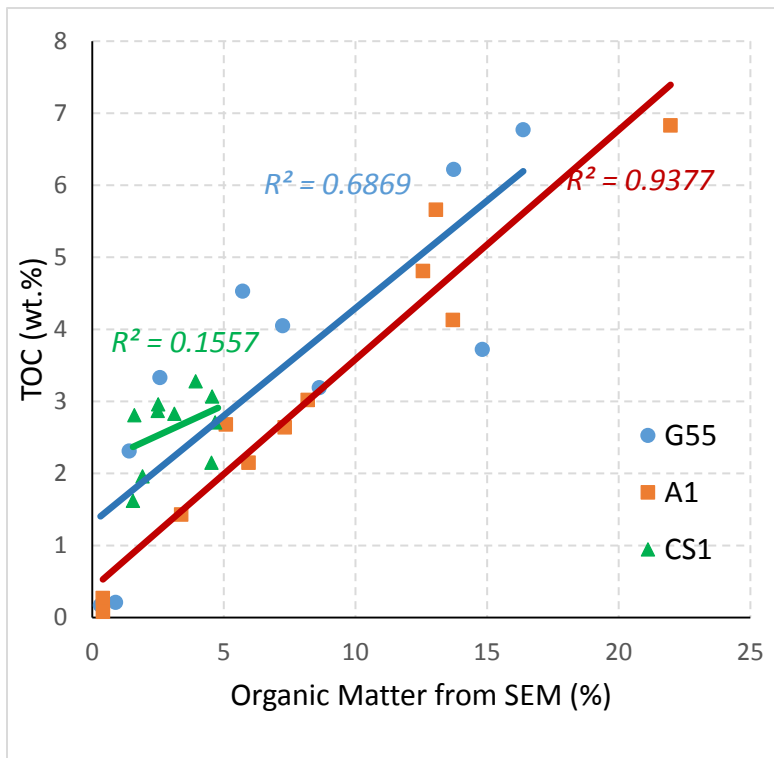


Figure 1-8. Correlation between organic matter captured by SEM images and bulk rock total organic carbon.

Table 1-1. Comparison of Manual picking results with automatic threshold result. Images from a to f are listed in Figure 1-4 and Figure 1-6.

	a	b	c
Manual delineation of porosity (%)	3.50	1.18	1.29
Automatic threshold porosity (%)	3.43	1.22	1.28
	d	e	f
Manual picking OM (%)	25.94	27.3	32.92
Automatic threshold OM (%)	25.31	27.22	32.06

We also tested one image from a Chinese shale sample, which is donated by Dr. Guochang Wang from St. Francis University. The result is demonstrated in Figure 1-9.

Figure 1-10 illustrates the presented workflow on differentiating OM hosted porosity and mineral hosted porosity.

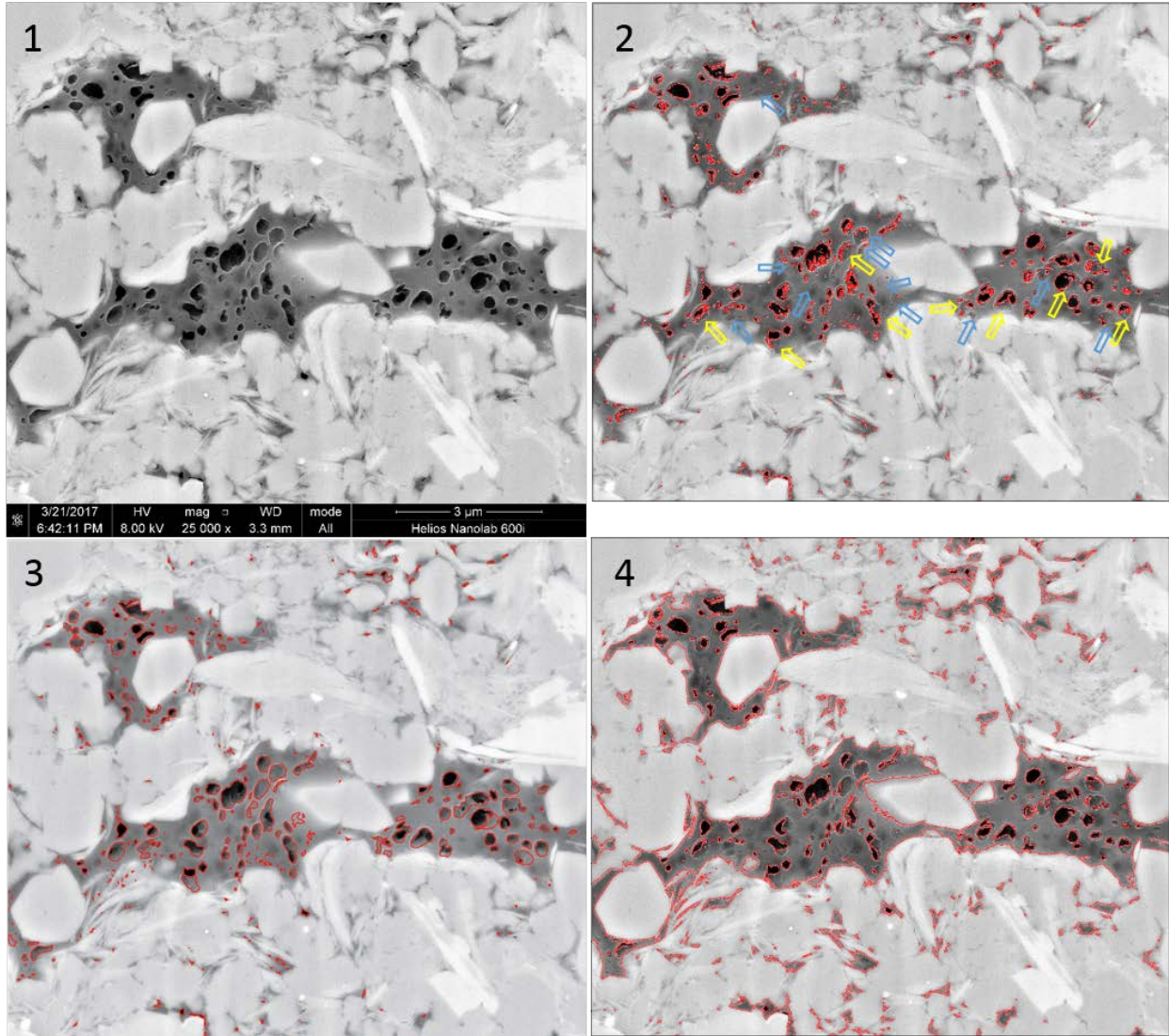


Figure 1-9. Application of the proposed workflow on an independently supplied image. (1) original image, (2) automated pore segmentation with red outlines highlighting the border of pores, yellow and blue arrows depict the difference between manual and automated segmentation, see detailed discussion in the text; (3) pores manually segmented by an independent third party; (4) automated segmented OM. Image courtesy of Dr. Guochang Wang.

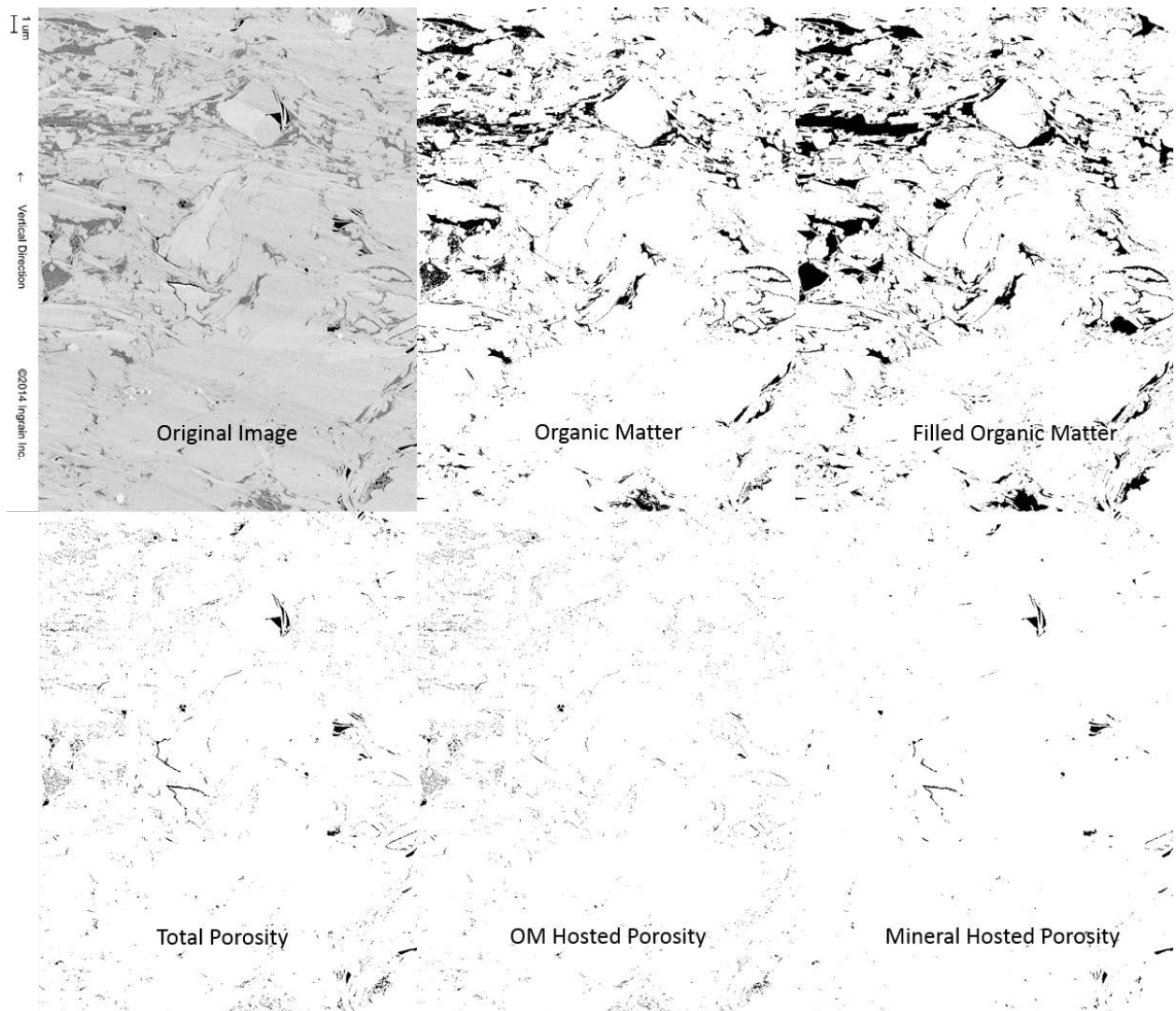


Figure 1-10. Illustration of proposed workflow on a test image (from Well CS1, 7114.50 ft., 2168.50 m).

Discussion

Sensitivity test

We did a sensitivity test on the effect of the thresholding parameter on the pore segmentation result, using samples a, b, and c. The local threshold window radius was tested in a range from 10 to 20 pixels (Figure 1-3). For sample (a), we observed a gradual increase of the porosity result from 3.18 to 3.63% when the local threshold window radius increases from 10 to 20. The results show a very good linear correlation (Figure 1-3). For sample (b), the porosity increases from 1.09 to 1.33% in the same window range. Sample (c) shows a different trend. The porosity readings at 10, 15, and 20 pixels window radii are 1.26, 1.28, and 1.27 respectively. This change is almost negligible. Based on this observation, if we choose 15 pixels as the thresholding window radius, then for sample (a), the porosity in a 10 to 20 pixels window changes within 0.25%, and for sample (b), the porosity value changes about 0.12%. The consistency of the adaptive local thresholding is assumed to be acceptable, and is completely repeatable if using the same window size on the same image. The manually picked results for these three samples are 3.50, 1.18, and 1.29% respectively. We recommend choosing 15 pixels as the default local threshold window radius, because for samples (a) and (b), it produces the median value of porosity and minimizes the variance.

All the three sample we used to demonstrate the method are SE2 SEM images, but their pore types are different. In sample (c), most pores are hosted by clay particles. The contrast between pores and minerals is very vivid. As a result on sample (c), the result is not very sensitive to the radius setting. By setting the window radius to a fixed number, we achieve a consistent result. Essentially, there is no fixed thresholding, and porosity readings are very similar through different thresholding window radii.

We also tested the effect of image resolution. The original images were saved as 600 pixel per inch (PPI). We change the resolution by reducing the pixel size, and then ran the segmentation automatically and manually. We tested 300, 100, and 75 PPI. Since the scale bar is fixed, these changes mean an analysis at 2×, 6×, and 8× of the original resolution. Although each sample trend is different, we observe an overall decrease in porosity results when lowering the input image resolution (Figure 1-11). For example, in reducing the resolution from 600 to 300 and 100 PPI, sample (a), (b), and (c) lost 0.36, 0.51, and 0.21% of the visible porosity respectively by automatic thresholding, and 0.49, 0.30, and 0.07% visible porosity respectively by manual picking. This change is much higher than the effect of threshold window size. Also we notice that the visible porosity loss of sample (c) is lower than the other two samples. We attribute this to the fact that sample (c) has the least OM content, which makes the pores easier to be picked. While sample (a) and (b) have significant amount of OM hosted pores, when the pixel density is lowered, pores fade in OM and make them hard to recognize.

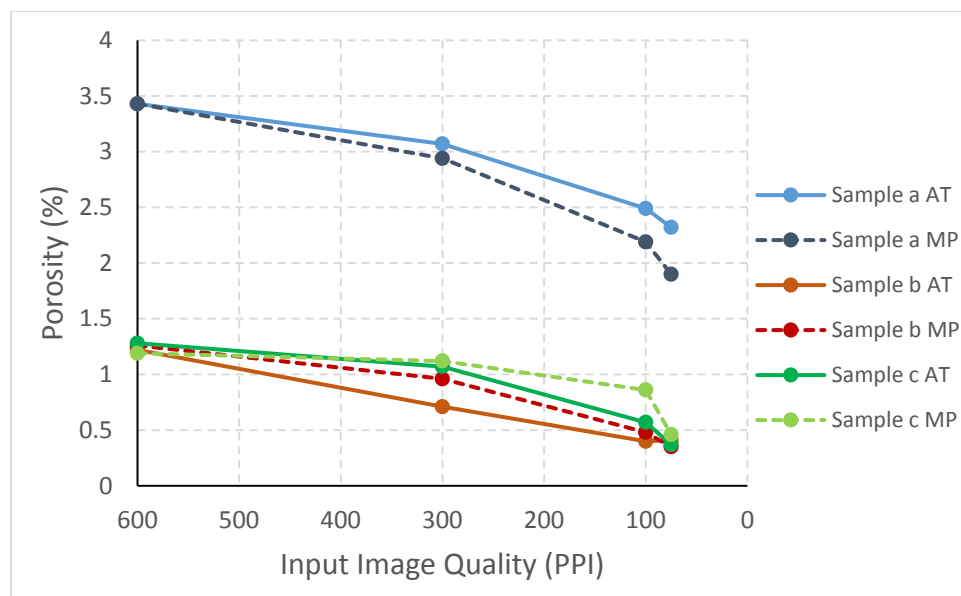


Figure 1-11. Input image quality and segmentation results (porosity). Solid lines are automatic thresholding (AT) results, while dash lines are manual picking (MP) results.

Challenges

Ion-milling SEM is a powerful tool to study mudrock, yet it faces significant challenges. The first is the extremely fine scale of observation required to provide sufficient resolution, especially under high magnification. Typically the scale of observation is tens of square micrometers. An upscale from pore-imaging to compositional mapping (e.g. Energy Dispersive X-Ray Spectroscopy/EDS elemental mapping), and to the thin-section scale, is an immediate and obvious challenge. In addition, vertical and lateral heterogeneity in laminated mudrock may vary at the micrometer to centimeter scale (Lazar et al., 2015). To address this issue, large mosaics of SEM images have been used to obtain more representative information about the microstructure of mudrock (Klaver et al., 2012, 2015; Giffin et al., 2013; Hemes et al., 2013, 2015, Houben et al., 2013, 2014; Deirieh, 2016). These studies acquired hundreds of images and stitch them

together to cover a large area. Then an REA can be determined, representing the area above which the fraction of minerals and porosities doesn't change significantly. However, the REA differs significantly between different mudrock samples (Klaver et al., 2012, 2015, Houben et al., 2013, 2014; Hemes et al., 2015; Deirieh, 2016; Kelly et al., 2016). Therefore, it is still very challenging to determine whether an SEM image or a series of images are representative of the mudrock.

Manual delineation vs. automatic segmentation

To achieve the highest accuracy, when categorizing organic matter pores and inorganic pores, some scientists prefer manual pore interpretation over automatic pore recognition. There is no absolutely reliable pore segmentation, therefore we have chosen a manually delineated product as our reference, although we are aware of the limitation of such data. Sometimes, a manual interpretation of the SEM images is necessary because of artifacts, especially open fractures and redeposition of the ion milled materials. However, manual interpretation, when dealing with the large quantity of images required for a statistically representative elementary area within a heterogeneous mudrock, it can be very time-consuming, and is subject to operational bias.

The fast development of improved SEM imaging techniques, especially broad ion-beam (BIB) milling, make it beneficial to have a consistent methodology of image analysis. The cutting-edge mosaic method and multi-beam SEM have begun to address a long-lasting problem in SEM, namely representativeness, by scanning a much larger area compared to normal SEM. The large area analysis results are not as strongly affected by the scale of observation and the selection of region of interest (ROI). When representativeness is no longer the dominating issue, maintaining the consistency of the results becomes more important. If results are not consistent,

comparing results among samples or even different images of the sample could be problematic. Also, the time efficiency of manual processing becomes an issue because of the size of the scanning area and the high resolution.

Artifacts

Edge effects are common artifacts in SEM images of shale. Non-planar surfaces such as pore edges give off a greater electron signal than planar regions, which results in brighter pixels (Kelly et al., 2016). These surfaces appear to be a bright “ring” surrounding the OM or minerals (Jiang et al., 2015; Kelly et al., 2016). This makes it challenging to segment porosity automatically. However, since the edge effect increases the local variance, the segmentation algorithm proposed in this research actually take advantage of this type of artifact when it occurs.

We tested our work flow on an independently provided image (Figure 1-9). The major disagreement between our automatic segmentation and independent third party’s manual delineation is marked by the yellow and blue arrows. The method we propose can handle the edge effect very well. But there are certain very shallow pores that are incorrectly labeled as OM. Similar artifacts have also been noticed by Hemes et al. (2013), and referred to as a low-angle deepening pore border (yellow arrows in Figure 1-9). Disagreements that are marked with blue arrows, unlike other pores or low-angle pore borders, are caused by surface roughness or very shallow dents. From a quantitative perspective, we do not think they should be counted as pores. For this image, the automated-segmented porosity is 2.07%, while the manually picked porosity is 3.08%; pores depicted by blue arrows account for 0.75% of the difference. We therefore suggest the “correct” porosity result should be 2.33%, and our method captured 89% of the whole pore system. The problematic pores in Figure 9 are all very shallow, so that the detector received signals from the bottom of pores, and since they are OM hosted pores, the bottom is

obviously OM. A noteworthy question is to what extent we should categorize these very shallow depressions as pore space.

Image analysis of OM and porosity

Most organic matter (OM) in the Mahantango and Marcellus mudrock reservoirs is amorphous. SEM imaging allows the visualization of the spatial distribution of OM in mudrock. Our data show that the richness of OM in mudrock observed in SEM is correlated with the bulk rock TOC content (Figure 1-8). The application of SEM determined OM measurements appear representative of plug scale measurement that are commonly applied to larger-scale (e.g. reservoir) models. Although this technique can offer a comprehensive understanding of samples in terms of organic matter, one should not rely on individual SEM images measurement. Instead, multiple images (10 to 15) should be acquired.

The underestimation of porosity remains an issue for SEM, especially 2D SEM (Loucks et al., 2009, Milliken et al., 2013). Compared to the GRI method (crushed core analysis), SEM underestimates the porosity (Figure 1-12), because SEM cannot resolve and detect the large number of pores below current SEM resolution of 10 nm/pixel (in this research), whereas GRI can detect porosity contribution from pores much less than 10 nm (Luffel and Guidry, 1992). Milliken et al. (2013) studied samples from the Marcellus Shale, and found an unexpected negative correlation between TOC content and SEM visible porosity, although most of the visible pores are hosted by OM (Milliken et al., 2013). Although SEM can achieve a resolution of about 1 nm, the scale of observation is reduced to the point at which the observations do not provide a representative elementary area. Additionally, 2D SEM images show slices or cross sections of samples usually in the vertical orientation, so three-dimensional data about the pore

space that may be elongated in the third dimension within a heterogeneous rock such as shale are not accurately measured.

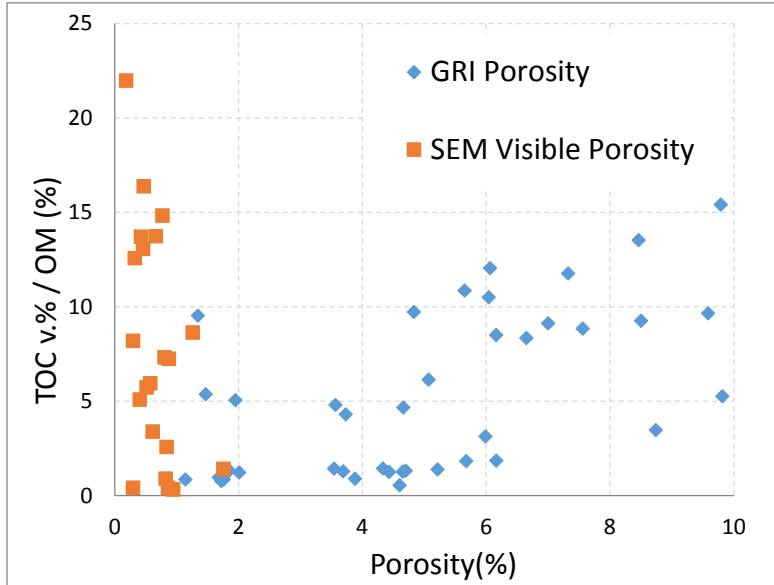


Figure 1-12. Comparing SEM visible porosity and GRI porosity.

The limitations of SEM for porosity determination should always be taken into consideration. Increasing abundance of OM has been shown to correlate with decreasing visible porosity in SEM images (Milliken et al., 2013). When dealing with samples that have a large portion of pores below the resolution of SEM, the porosity value itself has limited reliability.

Conclusions

Ion-milling SEM is a direct analytical technique to characterize the microstructure of a mudrock reservoir at a resolution of nanometers. Quantitative analysis provides important information regarding pore structure, porosity associated with organic matter or inorganic minerals, and richness of organic matter. Quantification of SEM images of mudrock samples remains challenging because of the lack of well-developed automated thresholding and segmentation methods. Manually picking the threshold is time-consuming and maintaining inter-

lab and intra-lab consistency is a challenge. Automated segmentation of SEM images offers benefits over manual methods. The key conclusions include:

1. A new workflow is described to quantify porosity and OM content from SEM image analysis. The segmentation of pore space and OM is based on adaptive local thresholding (Phansalkart Thresholding), Otsu thresholding, and Image Calculator, all of which can be accessed in public domain software such as ImageJ and Fiji. The workflow is documented to improve the consistency and efficiency of quantitative image analysis while maintaining acceptable accuracy.
2. The thresholding method segments the image based on local variance. It allows us to take advantage of the very common yet challenging edge effect. During the thresholding and segmentation processes, no specific threshold is required, thus avoiding potential bias. The workflow presented requires minimal supervision, or extra work. However, very shallow depressions do require additional work to provide a solution.
3. The only parameter that needs to be set when running segmentation of pores is the local thresholding window size. Based on our sensitivity test results, we recommend using 15 pixels for a 600 PPI image, although the result is not very sensitive to the window size (in the range between 10 and 20 pixels). The quality of the input image contributes more to the segmentation result. Lowering pixel density (lowering the resolution) will make pores harder to recognize.
4. Mineral hosted pores are easier to identify because the contrast between the foreground (pore space) and background (minerals) is larger compare to OM hosted pores.
5. The proposed thresholding method not only provides the porosity values, but also yields the distribution of pores and OM, a potential input for further research.

6. The proposed thresholding method was applied to Zeiss SE2 SEM images, and an FEI BSE SEM image. It successfully captured 89% of the pores.
7. Quantitative visual analysis of 2D-SE2-SEM images provides a representative value when estimating richness of organic matter. However, it can underestimate the porosity compared to the GRI method. This may be the result of differences in pore size resolution between the two radically different methods.

Reference Cited

- Adesida, A. G., I. Y. Akkutlu, D. E. Resasco, and C. S. Rai, 2011, SPE 147397 Kerogen Pore Size Distribution of Barnett Shale using DFT Analysis and Monte Carlo Simulations: SPE Annual Technical Conference and Exhibition, p. 1–14, doi:10.2118/147397-MS.
- Ambrose, R. J., D. Energy, R. C. Hartman, and W. Labs, 2010, SPE 131772 New Pore-scale Considerations for Shale Gas in Place Calculations: doi:10.2118/131772-MS.
- Anovitz, L. M., and D. R. Cole, 2015, Characterization and Analysis of Porosity and Pore Structures: Reviews in Mineralogy and Geochemistry, v. 80, p. 61–164, doi:10.2138/rmg.2015.80.04.
- Bai, B., M. Elgmati, H. Zhang, and M. Wei, 2013, Rock characterization of Fayetteville shale gas plays: Fuel, v. 105, p. 645–652, doi:10.1016/j.fuel.2012.09.043.
- Barrett, E. P., L. G. Joyner, and P. P. Halenda, 1951, The determination of pore volume and area distributions in porous substances. I. computations from nitrogen isotherms: Journal of the American Chemical Society, v. 73, no. 1, p. 373–380, doi:10.1021/ja01145a126.
- Bennett, R. H., N. R. O. Brien, M. H. Hulbert, O. S. Directorate, N. Oceanographic, O. S. Directorate, and N. Oceanographic, 1991, Determinants of clay microfabric signatures-Processes and mechanisms, *in* Microstructure of fine-grained sediments: New York, Springer-Verlag, p. 5–32.
- Bernard, S., L. Brown, R. Wirth, A. Schreiber, H.-M. Schulz, B. Horsfield, A. C. Aplin, and E. J. Mathia, 2013, FIB-SEM and TEM Investigations of an Organic-rich Shale Maturation Series from the Lower Toarcian Posidonia Shale, Germany: Nanoscale Pore System and Fluid-rock Interactions: Electron microscopy of shale hydrocarbon reservoirs: AAPG Memoir 102, p. 53–66, doi:10.1306/13391705M1023583.
- Bohacs, K. M., Q. R. Passey, M. Rudnicki, W. L. Esch, and O. R. Lazar, 2013, The Spectrum of Fine-Grained Reservoirs from “Shale Gas” to “Shale Oil”/ Tight Liquids : Essential Attributes, Key

- Controls, Practical Characterization: IPTC 2013: International Petroleum Technology Conference, no. Figure 1, p. 1–16, doi:10.2523/16676-MS.
- Boyce, M., A. Yanni, and T. Carr, 2010, Depositional control of organic content in the Middle Devonian Marcellus interval of West Virginia and Western Pennsylvania: Critical Assessment of ..., p. 3–6.
- Brunauer, S., P. H. Emmett, and E. Teller, 1938, Adsorption of Gases in Multimolecular Layers: Journal of the American Chemical Society, v. 60, no. 1, p. 309–319, doi:citeulike-article-id:4074706\rdoi:10.1021/ja01269a023.
- Bustin, R. M., A. M. M. Bustin, B. Columbia, X. Cui, and D. J. K. Ross, 2008, SPE 119892 Impact of Shale Properties on Pore Structure and Storage Characteristics.
- Bustin, R. M., a Bustin, D. Ross, G. Chalmers, V. Murthy, C. Laxmi, and X. Cui, 2009, Shale Gas Opportunities and Challenges *: Search and Discovery Articles, v. 40382.
- Carr, T. R. et al., 2016, The Marcellus Shale Energy and Environment Laboratory (MSEEL)*, in AAPG Eastern Section Meeting, Lexington, Kentucky.
- Chalmers, G. R. L., and R. Marc Bustin, 2007, On the effects of petrographic composition on coalbed methane sorption: International Journal of Coal Geology, v. 69, no. 4, p. 288–304, doi:10.1016/j.coal.2006.06.002.
- Chalmers, G. R. L., D. J. K. Ross, and R. M. Bustin, 2012, Geological controls on matrix permeability of Devonian Gas Shales in the Horn River and Liard basins, northeastern British Columbia, Canada: International Journal of Coal Geology, v. 103, p. 120–131, doi:10.1016/j.coal.2012.05.006.
- Chen, R., and S. Sharma, 2017, Linking the Acadian Orogeny with organic-rich black shale deposition: Evidence from the Marcellus Shale: Marine and Petroleum Geology, v. 79, p. 149–158, doi:10.1016/j.marpetgeo.2016.11.005.

- Chen, R., and S. Sharma, 2016, Role of alternating redox conditions in the formation of organic-rich interval in the Middle Devonian Marcellus Shale , Appalachian Basin , USA: *Palaeogeography, Palaeoclimatology, Palaeoecology*, v. 446, p. 85–97, doi:10.1016/j.palaeo.2016.01.016.
- Chen, R., S. Sharma, T. Bank, D. Soeder, and H. Eastman, 2015, Comparison of isotopic and geochemical characteristics of sediments from a gas- and liquids-prone wells in Marcellus Shale from Appalachian Basin, West Virginia: *Applied Geochemistry*, v. 60, p. 59–71, doi:10.1016/j.apgeochem.2015.01.001.
- Clarkson, C. R., J. M. Wood, S. E. Burgis, S. D. Aquino, and M. Freeman, 2012, Nanopore-structure analysis and permeability predictions for a tight gas siltstone reservoir by use of low-pressure adsorption and mercury-intrusion techniques: *SPE Reservoir Evaluation & Engineering*, v. 15, no. 6, p. 648–661, doi:10.2118/155537-PA.
- Crain, E. R., and D. Holgate, 2014, A 12-Step program to reduce uncertainty in kerogen-rich reservoirs: *Canadian Well Logging Society*, v. i, no. Spring, p. 10–16.
- Culligan, K. A., D. Wildenschild, B. S. B. Christensen, W. G. Gray, and M. L. Rivers, 2006, Pore-scale characteristics of multiphase flow in porous media : A comparison of air – water and oil – water experiments: *Advances in Water Resources*, v. 29, p. 227–238, doi:10.1016/j.advwatres.2005.03.021.
- Culligan, K. A., D. Wildenschild, B. S. B. Christensen, W. G. Gray, M. L. Rivers, and A. F. B. Tompson, 2004, Interfacial area measurements for unsaturated flow through a porous medium: *Water Resources Research*, v. 40, no. W12413, p. 1–12, doi:10.1029/2004WR003278.
- Curtis, M. E., and R. J. Ambrose, 2011, Investigation of the relationship between organic porosity and thermal maturity in the Marcellus Shale, *in* SPE Conference: p. 4pp, doi:10.2118/144370-ms.
- Curtis, M. E., C. H. Sondergeld, R. J. Ambrose, and C. S. Rai, 2012, Microstructural investigation of gas

- shales in two and three dimensions using nanometer-scale resolution imaging: AAPG Bulletin, v. 96, no. 4, p. 665–677, doi:10.1306/08151110188.
- Deirieh, A., 2016, From Clay Slurries to Mudrocks : A Cryo-SEM Investigation of the Development of the Porosity and Microstructure: Massachusetts Institute of Technology, 226 p.
- Desbois, G., J. L. Urai, and P. A. Kukla, 2009, Morphology of the pore space in claystones – evidence from BIB/FIB ion beam sectioning and cryo-SEM observations: eEarth Discussions, v. 4, no. 1, p. 1–19, doi:10.5194/eed-4-1-2009.
- Dilks, A., and S. C. Graham, 1985, Quantitative Mineralogical Characterization of Sandstones by Back-scattered Electron Image Analysis: Journal of Sedimentary Petrology, v. 55, no. 3, p. 347–355.
- Dong, T., and N. B. Harris, 2013, Pore Size Distribution and Morphology in the Horn River Shale, Middle and Upper Devonian, Northeastern British Columbia, Canada: Electron microscopy of shale hydrocarbon reservoirs: AAPG Memoir 102, p. 67–80, doi:10.1306/13391706M1023584.
- Driskill, B., J. Walls, J. DeVito, and S. W. Sinclair, 2013, Applications of SEM Imaging to Reservoir Characterization in the Eagle Ford Shale, South Texas, U.S.A., *in* Electron microscopy of shale hydrocarbon reservoirs: AAPG Memoir 102: p. 115–136, doi:10.1306/13391709M1023587.
- EIA, U. S., 2018, Annual Energy Outlook 2018 with projections to 2050 Table of contents: Washington, DC, 74 p.
- Erdman, N., and N. Drenzek, 2013, Integrated Preparation and Imaging Techniques for the Microstructural and Geochemical Characterization of Shale by Scanning Electron Microscopy: Electron microscopy of shale hydrocarbon reservoirs: AAPG Memoir 102, p. 7–14, doi:10.1306/13391700M1023581.
- Espitalie, J., G. Deroo, and F. Marquis, 1985, La pyrolyse Rock-Eval et ses applications. Deuxième

- partie.: *Revue de l'Institut Français du Pétrole*, v. 40, no. 6, p. 755–784, doi:10.2516/ogst:1985045.
- Ettensohn, F. R., and T. R. Lierman, 2012, Large-scale Tectonic Controls on the Origin of Paleozoic Dark-shale Source-rock Basins: Examples from the Appalachian Foreland Basin, Eastern United States: *AAPG Bulletin*, v. 100, no. January 2012, p. 95–124, doi:10.1306/13351549M1003529.
- Fishman, N. S., J. L. Ridgley, D. K. Higley, M. L. W. Tuttle, and D. L. Hall, 2012, Ancient Microbial Gas in the Upper Cretaceous Milk River Formation, Alberta and Saskatchewan: A Large Continuous Accumulation in Fine-grained Rocks: Shale Reservoirs —Giant Resources for the 21st Century: *AAPG Memoir 97*, v. 97, p. 258–289, doi:10.1306/13321471M973493.
- Gallagher, N. C. J., and G. L. Wise, 1981, A Theoretical Analysis of the Properties of Median Filters: *IEEE Transactions on acoustic, speech, and signal processing*, v. 29, no. 6, p. 1136–1141.
- Giffin, S., R. Littke, J. Klaver, and J. L. Urai, 2013, Application of BIB-SEM technology to characterize macropore morphology in coal: *International Journal of Coal Geology*, v. 114, p. 85–95, doi:10.1016/j.coal.2013.02.009.
- Hemes, S., G. Desbois, J. L. Urai, M. De Craen, and M. Honty, 2013, Variations in the morphology of porosity in the Boom Clay Formation: Insights from 2D high resolution BIB-SEM imaging and Mercury injection Porosimetry: *Geologie en Mijnbouw/Netherlands Journal of Geosciences*, v. 92, no. 4, p. 275–300, doi:doi:10.1017/S0016774600000214.
- Hemes, S., G. Desbois, J. L. Urai, B. Schröppel, and J. O. Schwarz, 2015, Multi-scale characterization of porosity in Boom Clay (HADES-level, Mol, Belgium) using a combination of X-ray u-CT, 2D BIB-SEM and FIB-SEM tomography: *Microporous and Mesoporous Materials*, v. 208, p. 1–20, doi:10.1016/j.micromeso.2015.01.022.
- Houben, M. E., G. Desbois, and J. L. Urai, 2014, A comparative study of representative 2D microstructures in Shaly and Sandy facies of Opalinus Clay (Mont Terri, Switzerland) inferred from

- BIB-SEM and MIP methods: *Marine and Petroleum Geology*, v. 49, p. 143–161, doi:10.1016/j.marpetgeo.2013.10.009.
- Houben, M. E., G. Desbois, and J. L. Urai, 2013, Pore morphology and distribution in the Shaly facies of Opalinus Clay (Mont Terri, Switzerland): Insights from representative 2D BIB-SEM investigations on mm to nm scale: *Applied Clay Science*, v. 71, p. 82–97, doi:10.1016/j.clay.2012.11.006.
- Huang, J., T. Cavanaugh, and B. Nur, 2013, An Introduction to SEM Operational Principles and Geologic Applications for Shale Hydrocarbon Reservoirs: Electron microscopy of shale hydrocarbon reservoirs: *AAPG Memoir 102*, p. 1–6, doi:10.1306/13391699M1023580.
- Jarvie, D. M., R. J. Hill, T. E. Ruble, and R. M. Pollastro, 2007, Unconventional shale-gas systems: The Mississippian Barnett Shale of north-central Texas as one model for thermogenic shale-gas assessment: *AAPG Bulletin*, v. 91, no. 4, p. 475–499, doi:10.1306/12190606068.
- Katz, A. J., and A. H. Thompson, 1985, Fractal Sandstone Pores: Implications for Conductivity and Pore Formation: *Physical Review Letters*, v. 54, no. 12, p. 1325–1328.
- Kelly, S., H. El-sobky, C. Torres-verdín, and M. T. Balhoff, 2016, Advances in Water Resources Assessing the utility of FIB-SEM images for shale digital rock physics: *Advances in Water Resources*, v. 95, p. 302–316, doi:10.1016/j.advwatres.2015.06.010.
- Klaver, J., G. Desbois, R. Littke, and J. L. Urai, 2015, BIB-SEM characterization of pore space morphology and distribution in postmature to overmature samples from the Haynesville and Bossier Shales: *Marine and Petroleum Geology*, v. 59, p. 451–466, doi:10.1016/j.marpetgeo.2014.09.020.
- Klaver, J., G. Desbois, J. L. Urai, and R. Littke, 2012, BIB-SEM study of the pore space morphology in early mature Posidonia Shale from the Hils area, Germany: *International Journal of Coal Geology*, v. 103, p. 12–25, doi:10.1016/j.coal.2012.06.012.

- Ko, L. T., R. G. Loucks, K. L. Milliken, Q. Liang, T. Zhang, X. Sun, P. C. Hackley, S. C. Ruppel, and S. Peng, 2017, Controls on pore types and pore-size distribution in the Upper Triassic Yanchang Formation, Ordos Basin, China: Implications for pore-evolution models of lacustrine mudrocks: *Interpretation*, v. 5, no. 2, p. 127–148, doi:10.1190/INT-2016-0115.1.
- Kuila, U., and M. Prasad, 2013, Specific surface area and pore-size distribution in clays and shales: *Geophysical Prospecting*, v. 61, no. 2, p. 341–362, doi:10.1111/1365-2478.12028.
- Lash, G. G., and D. R. Blood, 2014, Organic matter accumulation, redox, and diagenetic history of the Marcellus Formation, southwestern Pennsylvania, Appalachian basin: *Marine and Petroleum Geology*, v. 57, no. November, p. 244–263, doi:10.1016/j.marpetgeo.2014.06.001.
- Lash, G. G., and T. Engelder, 2011, Thickness trends and sequence stratigraphy of the Middle Devonian Marcellus Formation, Appalachian Basin: Implications for Acadian foreland basin evolution: *AAPG Bulletin*, v. 95, no. 1, p. 61–103, doi:10.1306/06301009150.
- Lazar, R., K. Bohacs, R. Klimentidis, M. Dumitrescu, and J. Ottmann, 2016, An SEM Study of Porosity in the Eagle Ford Shale of Texas—Pore Types and Porosity Distribution in a Depositional and Sequence-stratigraphic Context: The Eagle Ford Shale: A renaissance in U.S. oil production: *AAPG Memoir 110*, p. 167–186, doi:10.1306/13541961M1103589.
- Lazar, O. R., K. M. Bohacs, J. H. S. Macquaker, J. Schieber, and T. M. Demko, 2015, Capturing Key Attributes of Fine-Grained Sedimentary Rocks In Outcrops, Cores, and Thin Sections: Nomenclature and Description Guidelines: *Journal of Sedimentary Research*, v. 85, no. 3, p. 230–246.
- Loucks, R. G., R. M. Reed, S. C. Ruppel, and U. Hammes, 2012, Spectrum of pore types and networks in mudrocks and a descriptive classification for matrix-related mudrock pores: *AAPG Bulletin*, v. 96, no. 6, p. 1071–1098, doi:10.1306/08171111061.

- Loucks, R. G., R. M. Reed, S. C. Ruppel, and D. M. Jarvie, 2009, Morphology, Genesis, and Distribution of Nanometer-Scale Pores in Siliceous Mudstones of the Mississippian Barnett Shale: *Journal of Sedimentary Research*, v. 79, no. 12, p. 848–861, doi:10.2110/jsr.2009.092.
- Luffel, D. L., and F. K. Guidry, 1992, New Core Analysis Methods for Measuring Reservoir Rock Properties of Devonian Shale, *in* SPE Annual Technical Conference and Exhibition: p. 1184–1190, doi:10.2118/20571-PA.
- Mastalerz, M., A. Schimmelmann, A. Drobniak, and Y. Chen, 2013, Porosity of Devonian and Mississippian New Albany Shale across a maturation gradient: Insights from organic petrology', gas adsorption, and mercury intrusion: *AAPG Bulletin*, v. 97, no. 10, p. 1621–1643, doi:10.130/04011312194.
- Matthew, B. L., and T. R. Carr, 2009, Lithostratigraphy and Petrophysics of the Devonian Marcellus Interval in West Virginia and Southwestern Pennsylvania.
- Milliken, K. L., and R. J. Day-Stirrat, 2013, Cementation in mudrocks: Brief review with examples from cratonic basin mudrocks: *AAPG Memoir*, v. 103, p. 133–150, doi:10.1306/13401729H5252.
- Milliken, K. L., R. J. Day-Stirrat, P. K. Papazis, and C. Dohse, 2012, Carbonate Lithologies of the Mississippian Barnett Shale, Fort Worth Basin, Texas: Shale reservoirs—Giant resources for the 21st century, p. 290–321, doi:10.1306/13321473M97252.
- Milliken, K. L., W. L. Esch, R. M. Reed, and T. Zhang, 2012, Grain assemblages and strong diagenetic overprinting in siliceous mudrocks, Barnett Shale (Mississippian), Fort Worth Basin, Texas: *AAPG Bulletin*, v. 96, no. 8, p. 1553–1578, doi:10.1306/12011111129.
- Milliken, K. L., L. T. Ko, M. Pommer, and K. M. Marsaglia, 2014, Sem Petrography of Eastern Mediterranean Sapropels: Analogue Data For Assessing Organic Matter In Oil and Gas Shales: *Journal of Sedimentary Research*, v. 84, no. 11, p. 961–974, doi:10.2110/jsr.2014.75.

- Milliken, K. L., and T. Olson, 2016, Amorphous and Crystalline Solids as Artifacts in SEM Images: p. 1–8, doi:10.1306/13592013M112252.
- Milliken, K. L., and R. M. Reed, 2010, Multiple causes of diagenetic fabric anisotropy in weakly consolidated mud , Nankai accretionary prism , IODP Expedition 316: *Journal of Structural Geology*, v. 32, no. 12, p. 1887–1898, doi:10.1016/j.jsg.2010.03.008.
- Milliken, K. L., M. Rudnicki, D. N. Awwiller, and T. Zhang, 2013, Organic matter-hosted pore system, Marcellus Formation (Devonian), Pennsylvania: *AAPG Bulletin*, v. 97, no. 2, p. 177–200, doi:10.1306/07231212O48.
- Mosher, K., J. He, Y. Liu, E. Rupp, and J. Wilcox, 2013, Molecular simulation of methane adsorption in micro- and mesoporous carbons with applications to coal and gas shale systems: *International Journal of Coal Geology*, v. 109–110, p. 36–44, doi:10.1016/j.coal.2013.01.001.
- Nole, M., H. Daigle, K. L. Milliken, and M. Prodanovic, 2016, A method for estimating microporosity of fine-grained sediments and sedimentary rocks via scanning electron microscope image analysis: *Sedimentology*, v. 63, no. 6, p. 1507–1521, doi:10.1111/sed.12271.
- Olson, E., 2012, The Importance of Sample Preparation when Measuring Specific Surface Area: *Journal of GXP Compliance*, v. 16, no. 3, p. 52~62.
- Otsu, N., 1979, A Threshold Selection Method from Gray-Level Histograms: *IEEE Transactions on Systems, Man, and Cybernetics*, v. 19, no. 1, p. 62–66, doi:10.1109/TSMC.1979.4310076.
- Passey, Q. R., K. M. Bohacs, W. L. Esch, R. E. Klimentidis, and S. K. Sinha, 2012, My source rock is now my reservoir - geologic and petrophysical characterization of shale-gas reservoirs: *Search and Discovery*, v. 80231, no. 80231, p. 47pp.
- Phansalkart, N., S. More, A. Sabale, and M. Joshi, 2011, Adaptive Local Thresholding for Detection of

Nuclei in Diversity Stained Cytology Images, *in* International Conference on Communications and Signal Processing: p. 218–220.

Pommer, M., and K. Milliken, 2015, Pore types and pore-size distributions across thermal maturity, Eagle Ford Formation, southern Texas: AAPG Bulletin, v. 99, no. 9, p. 1713–1744, doi:10.1306/03051514151.

Reed, R. M., R. G. Loucks, and S. C. Ruppel, 2014, Comment on “ Formation of nanoporous pyrobitumen residues during maturation of the Barnett Shale (Fort Worth Basin) ” by Bernard et al . (2012): International Journal of Coal Geology, v. 127, p. 111–113, doi:10.1016/j.coal.2013.11.012.

Ross, D. J. K., and R. M. Bustin, 2008a, Characterizing the shale gas resource potential of Devonian-Mississippian strata in the Western Canada sedimentary basin: Application of an integrated formation evaluation: AAPG Bulletin, v. 92, no. 1, p. 87–125, doi:10.1306/09040707048.

Ross, D. J. K., and R. M. Bustin, 2008b, Characterizing the shale gas resource potential of Devonian-Mississippian strata in the Western Canada sedimentary basin: Application of an integrated formation evaluation: AAPG Bulletin, v. 92, no. 1, p. 87–125, doi:10.1306/09040707048.

Ross, D. J. K., and R. M. Bustin, 2009, The importance of shale composition and pore structure upon gas storage potential of shale gas reservoirs: Marine and Petroleum Geology, v. 26, no. 6, p. 916–927, doi:10.1016/j.marpetgeo.2008.06.004.

Ross, D. J. K., and R. M. Bustin, 2009, The importance of shale composition and pore structure upon gas storage potential of shale gas reservoirs: Marine and Petroleum Geology, v. 26, no. 6, p. 916–927, doi:10.1016/j.marpetgeo.2008.06.004.

Ross, D. J. K., and R. Marc Bustin, 2007, Impact of mass balance calculations on adsorption capacities in microporous shale gas reservoirs: Fuel, v. 86, no. 17–18, p. 2696–2706,

doi:10.1016/j.fuel.2007.02.036.

Sageman, B. B., A. E. Murphy, J. P. Werne, C. A. Ver Straeten, D. J. Hollander, and T. W. Lyons, 2003, A tale of shales: The relative roles of production, decomposition, and dilution in the accumulation of organic-rich strata, Middle-Upper Devonian, Appalachian basin: *Chemical Geology*, v. 195, no. 1–4, p. 229–273, doi:10.1016/S0009-2541(02)00397-2.

Saidian, M., L. J. Godinez, and M. Prasad, 2016, Effect of clay and organic matter on nitrogen adsorption specific surface area and cation exchange capacity in shales (mudrocks): *Journal of Natural Gas Science and Engineering*, v. 33, p. 1095–1106, doi:10.1016/j.jngse.2016.05.064.

Saidian, M., L. J. Godinez, and M. Prasad, 2015, Effect of Clay and Organic Matter on Nitrogen Adsorption Specific Surface Area and Cation Exchange Capacity in Shales (Mudrocks): *Annual Logging Symposium*, v. 56, p. 1–16.

Sauvola, J., and M. Pietikainen, 2000, Adaptive document image binarization: *Pattern recognition*, v. 33, p. 225–236.

Schieber, J., 2010, Common Themes in the Formation and Preservation of Intrinsic Porosity in Shales and Mudstones - Illustrated with Examples Across the Phanerozoic: *SPE Unconventional Gas Conference*, p. 10, doi:10.2118/132370-MS.

Schieber, J., 2013, SEM Observations on Ion-milled Samples of Devonian Black Shales from Indiana and New York: The Petrographic Context of Multiple Pore Types: *Electron microscopy of shale hydrocarbon reservoirs: AAPG Memoir 102*, no. April 2010, p. 153–172, doi:10.1306/13391711M1023589.

Schindelin, J. et al., 2012, Fiji: an open source platform for biological image analysis.: *Nature Methods*, v. 9, no. 7, p. 676–682, doi:10.1038/nmeth.2019.Fiji.

- Schindelin, J., C. T. Rueden, M. C. Hiner, and K. W. Eliceiri, 2015, The ImageJ ecosystem: An open platform for biomedical image analysis: *Molecular Reproduction and Development*, v. 82, no. 7–8, p. 518–529, doi:10.1002/mrd.22489.
- Schneider, J., P. B. Flemings, R. J. Day-Stirrat, and J. T. Germaine, 2011, Insights into pore-scale controls on mudstone permeability through resedimentation experiments: *Geology*, v. 39, no. 11, p. 1011–1014, doi:10.1130/G32475.1.
- Schneider, C. a, W. S. Rasband, and K. W. Eliceiri, 2012, NIH Image to ImageJ: 25 years of image analysis: *Nature Methods*, v. 9, no. 7, p. 671–675, doi:10.1038/nmeth.2089.
- Sezgin, M., and B. Sankur, 2004, Survey over image thresholding techniques and quatitative performance evaluation: *Journal of Electronic Imaging*, v. 13, no. 1, p. 146–168, doi:10.1117/1.1631316.
- Sing, K., 2001, The use of nitrogen adsorption for the characterisation of porous materials: *Colloids and Surfaces A: Physicochemical and Engineering Aspects*, v. 187–188, p. 3–9, doi:10.1016/S0927-7757(01)00612-4.
- Sing, K. S. W., D. H. Everett, R. a. W. Haul, L. Moscou, R. a. Pierotti, J. Rouquérol, and T. Siemieniewska, 1982, Reporting Physisorption Data for Gas / Solid Systems with Special Reference to the Determination of Surface Area and Porosity: *Pure and Applied Chemistry*, v. 57, no. 4, p. 603–619, doi:10.1351/pac198557040603.
- Sing, K. S. W., and R. T. Williams, 2004, Physisorption hysteresis loops and the characterization of nanoporous materials: *Adsorption Science and Technology*, v. 22, no. December 2015, p. 773–782, doi:10.1260/0263617053499032.
- Slatt, R. M., and N. R. O'Brien, 2013, Microfabrics Related to Porosity Development, Sedimentary and Diagenetic Processes, and Composition of Unconventional Resource Shale Reservoirs as Determined by Conventional Scanning Electron Microscopy: *Electron microscopy of shale*

- hydrocarbon reservoirs: AAPG Memoir 102, p. 37–44, doi:10.1306/13391703M102441.
- Slatt, R. M., and N. R. O'Brien, 2011, Pore types in the Barnett and Woodford gas shales: Contribution to understanding gas storage and migration pathways in fine-grained rocks: AAPG Bulletin, v. 95, no. 12, p. 2017–2030, doi:10.1306/03301110145.
- Soeder, D. J., 2017, The Development of Natural Gas from the Marcellus Shale: Boulder, Colorado, The Geological Society of America, 143 p.
- Sondergeld, C. H., R. J. Ambrose, C. S. Rai, and J. Moncrieff, 2010, Micro-structural studies of gas shales: Society of Petroleum Engineers Unconventional Gas Conference, SPE Paper 131771, p. 17, doi:10.2118/131771-MS.
- Song, L., T. Paronish, V. Agrawal, B. Hupp, and S. Sharma, 2017, Depositional Environment and Impact on Pore Structure and Gas Storage Potential of Middle Devonian Organic Rich Shale, Northeastern West Virginia, Appalachian Basin, in Unconventional Resources Technology Conference (URTeC:2667397): doi:10.15530/urtec-2017-2667397.
- Strapoć, D., M. Mastalerz, A. Schimmelmann, A. Drobniak, and N. R. Hasenmueller, 2010, Geochemical constraints on the origin and volume of gas in the New Albany Shale (Devonian-Mississippian), eastern Illinois Basin: AAPG Bulletin, v. 94, no. 11, p. 1713–1740, doi:10.1306/06301009197.
- Thommes, M., K. Kaneko, A. V. Neimark, J. P. Olivier, F. Rodriguez-Reinoso, J. Rouquerol, and K. S. W. Sing, 2015, Physisorption of gases, with special reference to the evaluation of surface area and pore size distribution (IUPAC Technical Report): Pure and Applied Chemistry, v. 87, no. 9–10, p. 1051–1069, doi:10.1515/pac-2014-1117.
- Tian, H., L. Pan, X. Xiao, R. W. T. Wilkins, Z. Meng, and B. Huang, 2013, A preliminary study on the pore characterization of Lower Silurian black shales in the Chuandong Thrust Fold Belt, southwestern China using low pressure N₂ adsorption and FE-SEM methods: Marine and Petroleum

- Geology, v. 48, p. 8–19, doi:10.1016/j.marpetgeo.2013.07.008.
- Velde, B., 1996, Compaction trends of clay-rich deep sea sediments: *Marine Geology*, v. 133, p. 193–201.
- Walls, J. D., and E. Diaz, 2011, Relationship of shale porosity- permeability trends to pore type and organic content: *Petrophysics in Tight Oil Workshop*.
- Wang, G., and T. R. Carr, 2013, Organic-rich marcellus shale lithofacies modeling and distribution pattern analysis in the appalachian basin: *AAPG Bulletin*, v. 97, no. 12, p. 2173–2205, doi:10.1306/05141312135.
- Wang, G., Y. Ju, Z. Yan, and Q. Li, 2015, Pore structure characteristics of coal-bearing shale using fluid invasion methods: A case study in the Huainan-Huaibei Coalfield in China: *Marine and Petroleum Geology*, v. 62, p. 1–13, doi:10.1016/j.marpetgeo.2015.01.001.
- Wildenschild, D., and A. P. Sheppard, 2013, X-ray imaging and analysis techniques for quantifying pore-scale structure and processes in subsurface porous medium systems: *Advances in Water Resources*, v. 51, p. 217–246, doi:10.1016/j.advwatres.2012.07.018.
- Yu, W., K. Sepehrnoori, and T. W. Patzek, 2016, Modeling Gas Adsorption in Marcellus Shale With Langmuir and BET Isotherms.: *SPE Journal*, v. 21, no. 2, p. 589–600, doi:10.2118/170801-PA.
- Zagorski, W. a., G. R. Wrightstone, and D. C. Bowman, 2012, The Appalachian Basin Marcellus Gas Play: Its History of Development, Geologic Controls on Production, and Future Potential as a World-class Reservoir, *in AAPG Memoir 97: Shale Reservoirs-Giant Resources for the 21st Century*: p. 172–200, doi:10.1306/13321465M973491.
- Zhang, T., G. S. Ellis, S. C. Ruppel, K. Milliken, and R. Yang, 2012, Organic Geochemistry Effect of organic-matter type and thermal maturity on methane adsorption in shale-gas systems: *Organic*

Geochemistry, v. 47, p. 120–131, doi:10.1016/j.orggeochem.2012.03.012.

Zhang, S., R. E. Klimentidis, and P. Barthelemy, 2011, Porosity and permeability analysis on nanoscale FIB-SEM 3D imaging of shale rock, *in* International Symposium of the Society of Core Analysis: p. 1–12.

Chapter II

Depositional Environment and Impact on Pore Structure and Gas Storage Potential of Middle Devonian Organic Rich Shale, Northeastern West Virginia, Appalachian Basin

Liaosha Song*, Tom Paronish*, Vikas Agrawal*, Brittany Hupp*, Shikha Sharma*, Timothy Carr*

*Department of Geology and Geography, West Virginia University, Morgantown, WV, USA

Published at Unconventional Resources Technology Conference, at Austin, Texas 24-26 July 2017

Reference Number: URTeC 2667397

Abstract

Characterizing the pore structure of a shale-gas reservoir is significant for calculating the original gas in place and fluid-flow characteristics. To better understand the impact of organic matter accumulation, redox condition, and depositional environment on pore structure and storage capacity, integrated geological and petrophysical characterization of the Devonian organic-rich shale was conducted. Core samples from a newly drilled science well from the Marcellus Shale Energy and Environment Laboratory (MSEEL) project and other wells in the Appalachian basin were selected to undertake this research. X-ray fluorescence (XRF), X-ray diffraction (XRD), and pyrolysis were performed to understand variations in composition, mineralogy and total organic carbon (TOC). Samples were examined from an interval including the overlying Tully Limestone, organic-lean Mahantango Shale, organic-rich Marcellus Shale and top of the underlying Onondaga Limestone.

We introduce the application of subcritical N₂ adsorption to measure pore volume, pore-size distribution, and pore-surface area, which are critical properties in characterization of the nano-scale pore regime of mudstone reservoirs. Results of the test are used to build models of the mudstone pore systems. With variations of TOC and mineralogy, changes in the characteristics of pore structure are observed. Middle Devonian shale units have complex, heterogeneous pore size distributions as identified by subcritical N₂ adsorption. XRD results suggest a high content of clay minerals (mainly illite) through both Mahantango and Marcellus shale formations. Hysteresis of N₂ adsorption isotherm indicates slit-shape pores between 2nm and 50nm, possibly formed by clay particles. Organic matter shows a strong influence on pore volume and pore surface area, which strongly influences hydrocarbon storage mechanisms of shale-gas reservoirs. Carbonate-rich intervals show very low pore volume especially micropore (pore width smaller

than 2nm) volume, and surface area. The results of N₂ adsorption are compared with NMR log to upgrade the evaluation.

Introduction

Micro- to mesoporous structures of unconventional reservoirs are challenging to characterize because of the extremely small pore sizes. Investigation of the micro- or mesoporous structures and their impact on flow properties requires experimental approaches, and sample preparation that will not affect the physical structure of samples while removing water, hydrocarbon, and other contaminants. To study shale pores more accurately, techniques such as gas adsorption and nuclear magnetic resonance (NMR), have been applied. The low-temperature nitrogen N₂ adsorption method can offer micro-pore volume, meso-pore size distribution, and pore surface area. Understanding the limitations of the analyses is also important, since at the scale of micro- to meso-pores, the measurement techniques influence the result. In this paper, we review some of the sample preparation procedures to find an appropriate and repeatable measurement. The NMR T₂ spectra of core samples can be used to calculate porosity and permeability, and characterize pore-throat structures. Significant variations in pore structures can be expected within a formation due to lithologic variations resulting from depositional environment, sediment influx, diagenesis, and thermal maturation.

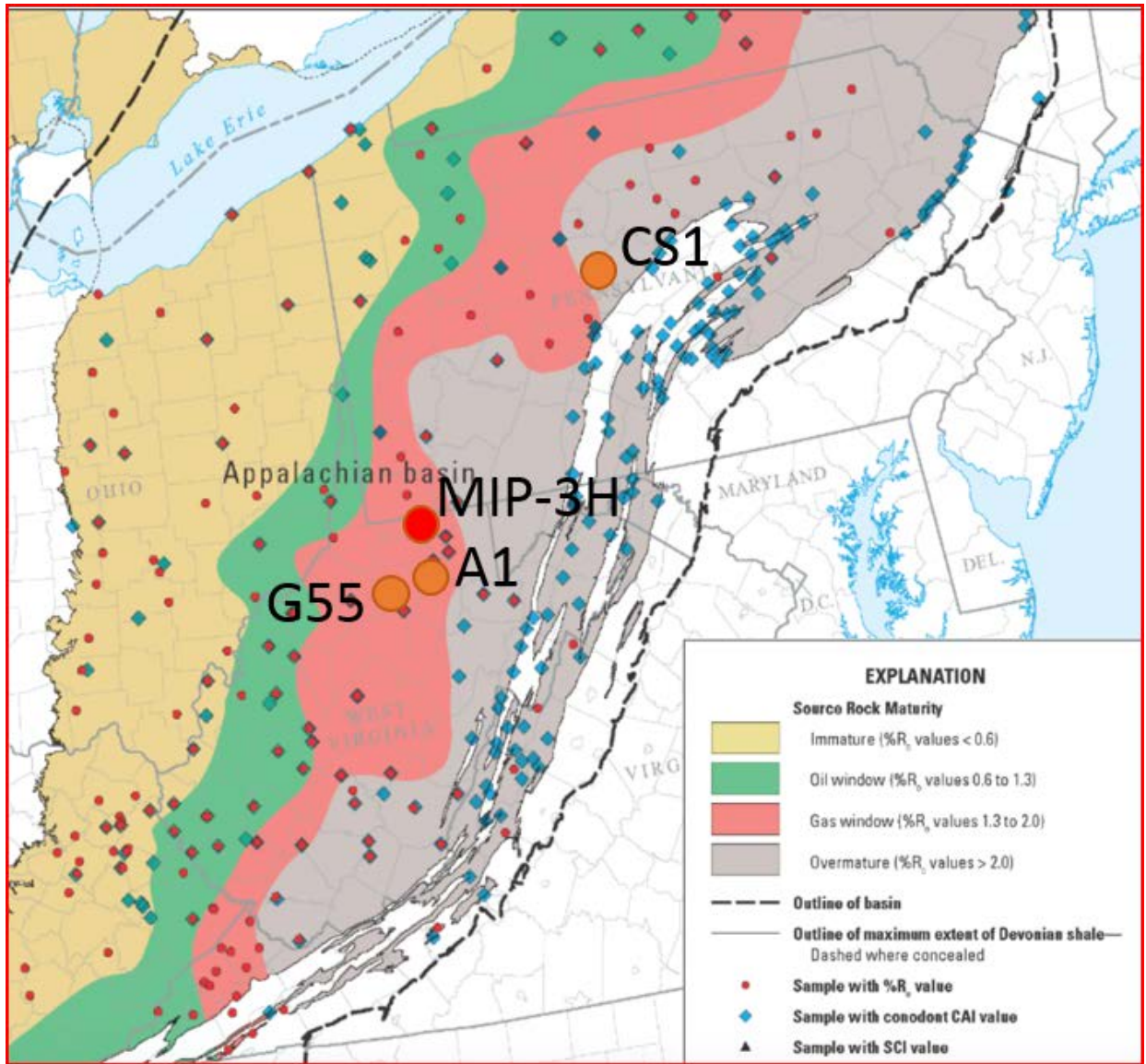


Figure 2-1: The Map shows the location of wells in West Virginia and Pennsylvania used in this paper, and the thermal maturity trend of the Marcellus Shale (modified after East et al., 2012).

Shale samples were obtained from four wells penetrating the Mahantango and Marcellus Formations in West Virginia and Pennsylvania, covering a range of thermal maturity (Figure 2-1). Total organic carbon content and mineralogy also vary significantly. Core samples from Marcellus Shale Energy and Environment Laboratory (MSEEL) project (MIP-3H well) were

selected to run X-ray diffraction (XRD), X-ray fluorescence (XRF), total organic carbon (TOC) and low-pressure nitrogen adsorption (also refer to as BET test) analyses and to compare to other wells. These techniques were used to characterize the pore-system characteristics of the Middle Devonian organic-rich shale in Appalachian basin, including the pore type, pore size, surface area, and pore volume. This research improves our understanding of the characteristics of the Marcellus and other organic-rich shale reservoirs and could further benefit evaluation of the hydrocarbon storage capacity of shale-reservoirs.

Methods

Source Rock Analysis (SRA)

Approximately 60 - 100 mg of pulverized rock was accurately weighed into an SRA crucible and placed in the SRA- Agilent autosampler, and held isothermally at 300°C for 3 minutes. During this isothermal heating, the free hydrocarbons are volatilized and detected by the FID detector where they are quantitatively detected and reported as milligrams (mg) of S1 per gram of rock. The free CO₂ is simultaneously liberated and detected by the IR cell and reported as milligrams (mg) of S3 per gram of rock up to 400°C. After the isothermal period, the temperature is ramped at 25°C/minute to 600°C. Between 300°C and 600°C organic hydrocarbons are generated from the pyrolytic degradation of the kerogen in the rock. The hydrocarbons are detected by the FID, labeled as S2, and reported as milligrams (mg) of S2 per gram of rock. Residual carbon is also measured and is recorded as S4 peak. TOC is calculated by using the equation: %TOC = 0.1 × [0.082 × (S1 + S2) + S4] (Espitalie et al., 1985). The WFT Source Rock Standard 533 (P/N 810-141) was run after every five samples. The standard deviation of the analysis was 0.07%. SRA analysis was performed at the National Energy Technology Laboratory in Morgantown.

X-ray Diffraction Analysis

Sixty-two samples collected as side-wall plugs from the MSEEL project were analyzed for x-ray diffraction (XRD) analysis to determine bulk mineralogy. These samples were ground in a steel grinding container for 5-10 minutes until powdered. Powder samples were pressed into chemplex pellets for loading of samples into the diffractometer. XRD analysis was performed using the PANalytical X'Pert Pro X-ray Diffractometer at West Virginia University Shared Research Facilities. Samples for this project were analyzed at 2θ angles between 5° and 75° , with a step time of ~ 75 seconds, leading to each sample being ran for approximately 13.5 minutes. X-rays were concentrated through a 20mm brass opening. The raw spectra were interpreted using the X'pert HighScore Plus Program to establish percentage of various mineral phases present. Bulk mineralogical interpretations were semi-quantitatively determined using reference intensity ratios (RIR).

Portable X-ray Fluorescence Geochemical Analysis

X-ray fluorescence (XRF) was performed on the same 62 samples that were prepared for x-ray diffraction analysis. The chemplex pellets were analyzed using a Bruker portable x-ray fluorescence spectrometer Tracer III-SD provided by the Division of Plant and Soil Sciences at West Virginia University. Each sample was analyzed for 120 seconds. Runs were completed to acquire major and trace elemental concentrations reported as weight percent. All runs were calibrated using the Bruker Mudrock calibration.

Low-pressure N₂ adsorption (BET test)

Low-pressure N₂ adsorption were conducted on a Micromeritics ASAP-2020 instrument at -196°C (77K). About 1 gram of shale sample was crushed with mortar and pestle until the whole mass passes through a 60-mesh sieve to prevent potential sample biasing due to sieving. One

sample from well CS1 is chosen to run the temperature test. About 5 gram of core sample was crushed and separated to 5 portions. Then samples were outgassed under high-vacuum apparatus at 120⁰C for 24 hours to remove adsorbed water and volatile matter before analyses with N₂. The relative pressure (P/P₀) ranged from 0.009 to 0.990. Both adsorption and desorption data points were acquired. Adsorption branch of the isotherms were used to obtain information about micropores (<2 nm in diameter) and mesopores (2~50 nm in diameter). The classification of pore sizes used in this article follows the classification system of the International Union of Pure and Applied Chemistry. This classification of pore sizes has proven to be very convenient in coal and shale studies (Bustin et al., 2008; Clarkson et al., 2012; Mastalerz et al., 2013).

Specific surface area (SSA) was calculated based on Brunauer-Emmet-Teller (BET) theory Pore volumes, and pore distributions based on Barrett-Joyner-Halenda (BJH) model, t-Plot, H-K model (Brunauer et al., 1938; Barrett et al., 1951; Sing, 2001).

Results and Discussion

1. Selection of degassing conditions

Prior to the BET test, samples are degassed. The impact of degassing procedure on the results must be considered before the test, because the interpretation models are based on clean surfaces for the adsorbent. The ultimate goal of degassing is to remove all the water and volatiles (such as remaining hydrocarbons), and other impurities, so that N₂ can reach the majority of pore space in the sample, while avoiding irreversible damage to organic matter, minerals, and sample texture. For this purpose, the nano-Darcy range permeability of shale makes it impractical to run this test on intact or large pieces of core sample. Most reservoir properties measurements of mudrocks are

performed on crushed core samples, because with crushed powder, the total path length for the gas to access the entire pore structure is significantly shorter than intact core samples, and the test can be completed within reasonable time (Luffel and Guidry, 1992; Kuila and Prasad, 2013).

Adesida et al., 2011 studied the effect of crushing on pore-structure parameters measured by N₂ gas adsorption. The results show that the specific surface area and total specific pore volume measured increases with decreasing sample particle size, which make sense since by crushing the sample to a finer size, extra surface area is created (Adesida et al., 2011). The increased pore volume is related to better pore accessibility at smaller grain sizes. When crushing the core sample, the different mechanical properties of the constituents (organic matter and minerals) of mudrocks are noticeable, and difference results in variance tendency to grind. By sieving the crushed sample into different sizes, it may result in a bias in the composition and mineralogy of each separated fraction (Kuila and Prasad, 2013). Therefore, the entire volume of crushed samples are used for BET test. The crushing procedure will follow Kuila and Prasad (2013) with a different grain size. Samples are crushed until the entire mass passes through a 60-mesh sieve (40 mesh in their research) to prevent potential sample biasing due to sieving. The samples preparation procedure should also be repeatable. After literature review, most research on N₂ adsorption on mudrocks has been conducted on 60 mesh samples (Table 2-1). Thus the result can be compared with former research, and benefit future study.

Table 2-1 Sample preparation procedures used in previous research (Devonian-Mississippian (D-M); Formation (Fm.))

Authors	Year	Gas	T (°C)	Mesh Size	Time (hour)	Sample Location	BET SSA (m ² /g)
Lu et al.	1995	He, CH ₄	50~60	18~25	24	Devonian Shale from WV and MI	
Chalmers and Bustin	2006, 2007	N ₂ , CO ₂	105	60	>12	North America coal and shale	0.01~7.9
Chalmers and Bustin	2008	N ₂ , CO ₂	150	60	12	Lower Cretaceous NE British Columbia	N ₂ : 2.5~19.5; CO ₂ : 16.1~62.9
Ross and Bustin	2009	N ₂ , CO ₂	110	60	24	Jurassic, D-M, North British Columbia	3.4~44.5
Adesida	2011	N ₂	100	20~40	3	Barnett	0.06~11.16
Strapoc et al.	2010	N ₂ , CO ₂		60		New Albany Shale (D-M), Illinois Basin	4~20
Mastalerz et al.	2012	N ₂ , CO ₂	110	60	14	New Albany Shale (D-M), Illinois Basin	N ₂ : 0.2~2.4;

							CO ₂ : 10.9~12.8
Zhang et al., 2012	2012	CH ₄	200	100	over night	Green River Fm., UT; Woodford Shale, OK; Camero coal, CO; Barnett Shale, Fort Worth Basin, TX	
Clarkson et al.	2012	N ₂ , CO ₂			4 over night	Triassic Montney, Western Canada	0.62~3.05
Clarkson et al.	2013	N ₂ , CO ₂	60	60	> 4 days	North America	2.3~17.1
Kuila	2013	N ₂	200	40	24	Haynesville	22.85~23.1 1
Heller and Zoback	2014	CO ₂	40	70	100~2	Eagle Ford, Barnett, Marcellus, Montney	

Maria-Fernanda Romero-Sarmiento	2014	N ₂	80		6	Mississippian Barnett Shale	14~39
---------------------------------	------	----------------	----	--	---	-----------------------------	-------

Another important factor for degassing is the temperature. Olson, 2012 summarized degassing temperature for 6 categories of materials (Table 2-2). Unfortunately, there isn't a category for mudrock, but still sheds some light on the selection of temperature. Amorphous oxides (e.g. silica, alumina) are similar to numerous minerals in mudrock, and a temperature from 100°C to 200°C did not change the pore structure (Olson, 2012). To find the best temperature for this research, one sample was split into 5 portions and degassed under 5 different temperatures. Figure 2-2 shows the pore size distributions of this sample at different temperatures. The overall trends are the same over all the five tests. However, as temperature increases, we noticed an increase in pore volume. Samples degassing under 80°C and 120°C show almost the same pore size distribution (PSD), which agrees with previous research on Barnett Shale (Adesida et al., 2011). In the rest of this study, 120°C is used as the degas temperature.

Table 2-2 Summary of outgassing conditions by material type (Olson, 2012)

Material Type	Flow or Vacuum	Temp. (°C)	Duration (hr)
Active pharmaceutical ingredients	Either	40 or ½ melting point	≥ 2
Activated carbon, zeolites, catalysts	Vacuum	90 then 300	1 then ≥ 3
Magnesium Stearate	Vacuum	40	2
Excipients, e.g. starches, celluloses, sugars, polymers	Either	20o < Tg or ½ melting point	≥ 2
Amorphous oxides, e.g. silica, alumina	Either	100 to 200	≥ ½
Metal oxide, e.g. titanium dioxide, zinc oxide, iron oxide, nickel oxide	Flow	300	≥ 2
Ionic salts & crystalline nonmetals	Either	300 or ½ melting point	≥ 2

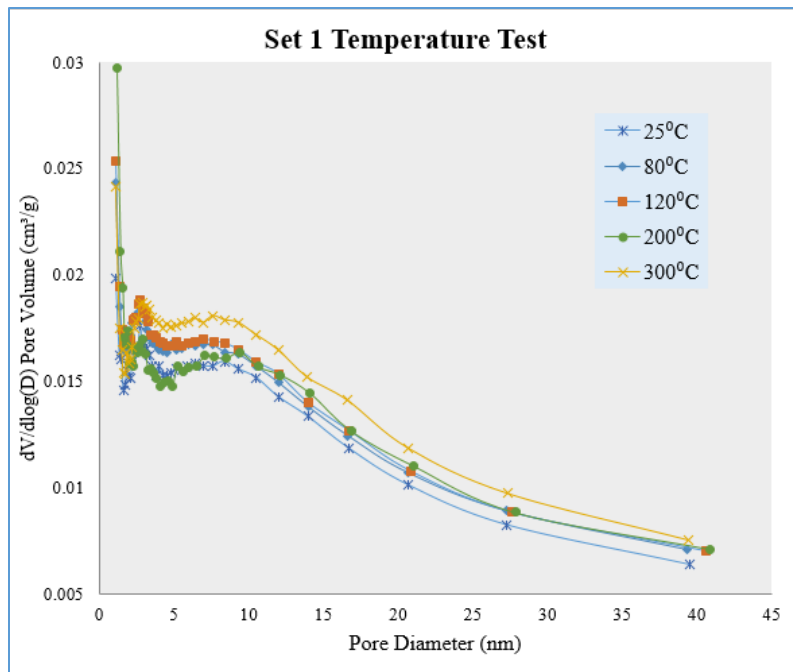


Figure 2-2. Barrett-Joyner-Halenda (BJH) pore-size-distributions of 5 samples degassed using 5 different temperatures.

2. Pore size distributions

Isotherms are the direct result from low pressure N₂ adsorption tests. Figure 2-3 shows the isotherms of the six samples from MIP-3H, all of which are classified as a type IV isotherm with H3 or H4 hysteresis loop (Sing et al., 1982; Sing, 2001). This shape of isotherm indicates that the shale samples are micro- to meso-porous materials, and this type of hysteresis loop often is observed with aggregates of plate-like particles forming slit-shaped pores. At high P/P₀ section (P/P₀ > 0.9), the isotherm shows a steep increase and no limit when P/P₀ close to 1. This is attribute to the sample also has macro pores, and the steep increase is representative of macro pore filling (Sing et al., 1982).

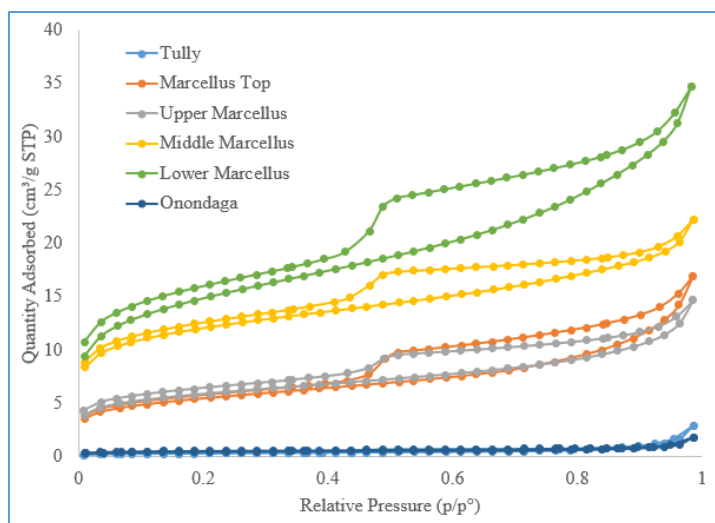


Figure 2-3. Isotherms of samples from MIP-3H, which has a type IV isotherm with H3 or H4 hysteresis loop.

The pore size distribution of the six samples from MIP-3H are calculated with the Barrett-Joyner-Halenda (BJH) model (Figure 2-4). The variation in pore structure are mainly controlled by TOC and mineralogy (Figure 2-5). Tully Limestone and Onondaga Limestone show significantly less pores compared with the Marcellus Shale within the meso-pore zone (2~50nm), and very few pores below 20 nm. In the Marcellus Shale, the pore structure also varies. The Marcellus top sample has a spike at 7 nm and a bigger pore volume than the upper Marcellus sample. The sample from the top of the Marcellus also has the highest clay content (Figure 2-5). Samples from the upper and middle Marcellus have similar PSD in 20nm to 50nm interval. The sample from the upper and middle Marcellus have similar PSD in 20nm to 50nm interval. The sample from the lower Marcellus, which has the highest TOC content, has the highest pore volume.

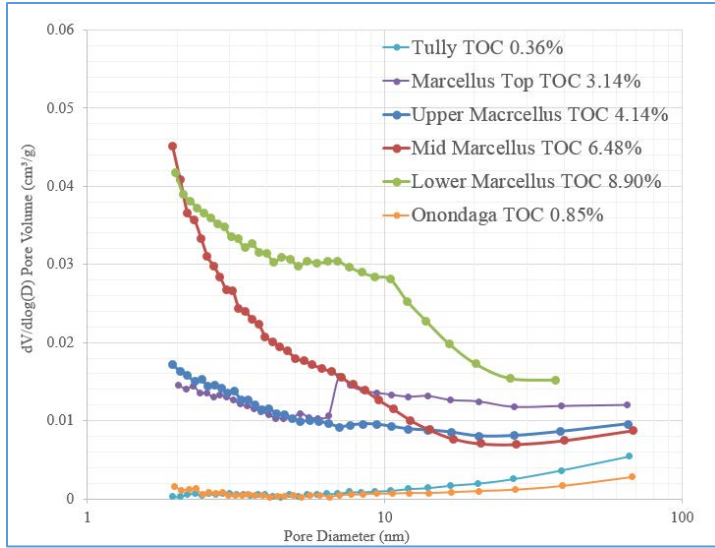


Figure 2-4: Pore size distribution of the samples across Tully Limestone, Marcellus Shale, and Onondaga Limestone with regard to the TOC weight percentage.

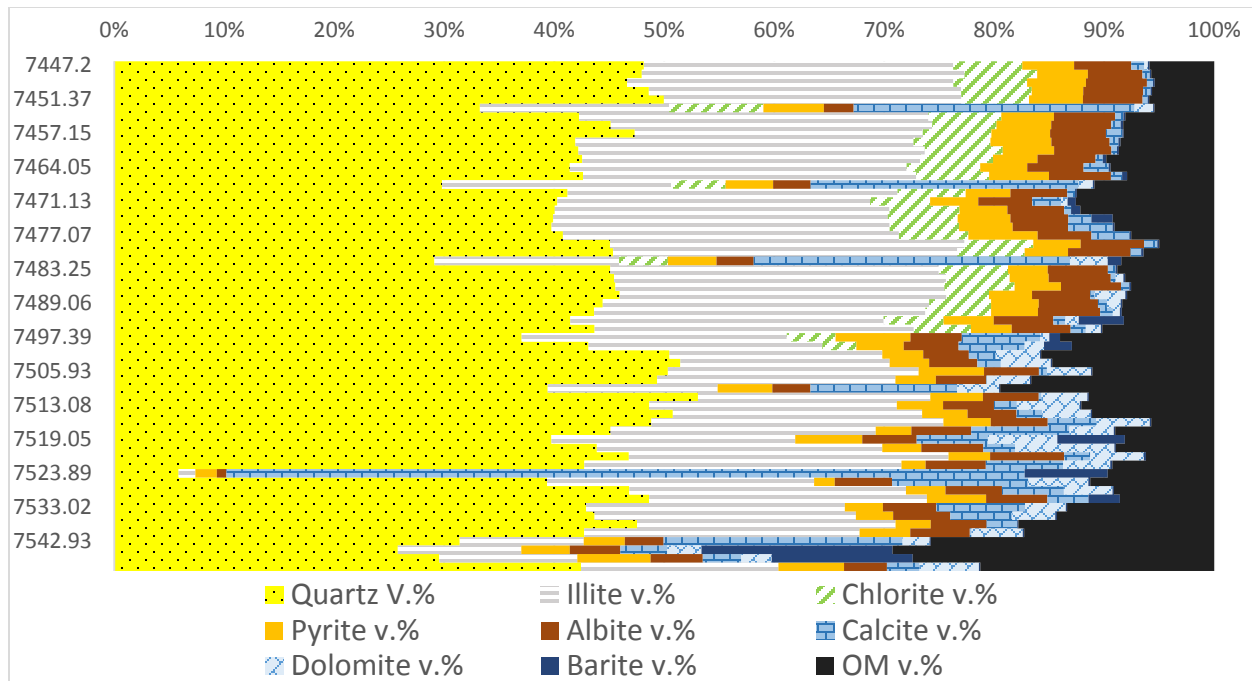


Figure 2-5: XRD data from well MIP-3H (in volume %) illustrating the mineralogical variations of the Marcellus Shale.

3. TOC, pore surface area, and pore volume

The specific surface area (SSA) of the six samples ranges from 1.09 m²/g to 52.9 m²/g (Table 2-3). The BJH pore volume of samples range from 0.003052 cm³/g to 0.051914 cm³/g (Table 2-3). The micro pore volume and surface area are calculated by T-plot. The BET specific surface area and BJH pore volume indicate an overall positive correlation with TOC (Figure 2-6, 2-7). MIP-3H, G55 and A1 (listed as 1.36<Ro<1.41) shows a better correlation compare to CS1 (listed as 2.67<Ro<2.89). There is a significant decrease in micro- to meso-pores with increasing carbonate content.

Table 2-3. Low-pressure N₂ adsorption test and TOC results

Depth(ft.)	Formation	BET SSA (m ² /g)	Micropore Area (m ² /g)	Micropore Volume (cm ³ /g)	BJH Pore Volume (cm ³ /g)	TOC wt. %
7201	Tully	1.09	0.1823	0.000078	0.004566	0.36
7452	Marcellus Top	19.43	4.3996	0.001861	0.027743	3.14
7466	Upper Marcellus	20.8849	5.6005	0.002382	0.024733	4.14
7508	Mid Marcellus	42.93	14.7628	0.006300	0.039927	6.48
7544	Lower Marcellus	52.90	10.5677	0.004379	0.051914	8.9
7555	Onondaga	1.74	0.5313	0.00022	0.003052	0.85

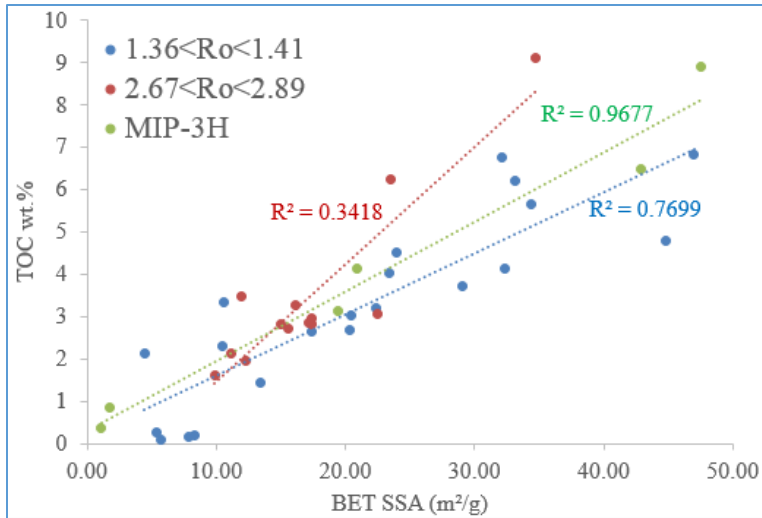


Figure 2-6: The relationship between BET specific surface area and TOC.

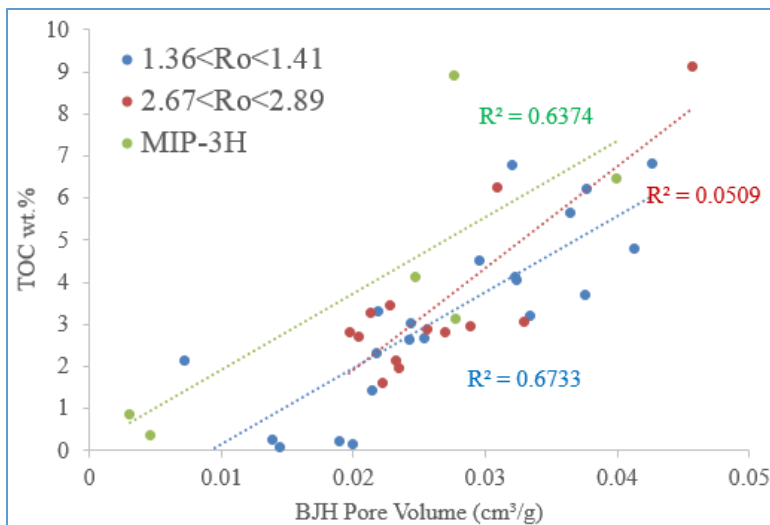


Figure 2-7: The relationship between BJH pore volume and TOC.

4. Mineralogy, lithology, and depositional environment

The MIP-3H well utilizes both common and advanced logging tools to provide insight into TOC and mineralogy at the log-scale (Figure 2-8). The Marcellus Shale at the MSEEL location is defined by three high gamma ray peaks (greater than 300 API) separated by thin carbonate

intervals (lower than 110 API). Linear relations between SRA derived TOC measurements and uranium and gamma ray help to predict the organic content throughout the Marcellus Shale interval. Generally, there is an increase in organic content with depth from about 5 wt.% in the upper Marcellus to 15 wt.% in the most organic portion of the lower Marcellus. This trend is reiterated by an increase in resistivity (Figure 2-8, tract 2 orange), which denotes organic matter and carbonate through this interval.

Mineralogy is determined using the XRD (Figure 2-5). The abundance of organic matter in volume percentage is calculated from TOC wt.% following Crain's workflow (Crain and Holgate, 2014). Then the XRD results are converted into volume fraction of minerals and organic matter with average mineral density. The average density of organic matter is set to be 1.26 g/cc (Crain and Holgate, 2014). Overall, there is a decrease in the clay content with depth in the Marcellus Shale with an increase in the organic matter. In lower Marcellus, the volume fraction of organic matter is 33% (Figure 2-5).

The NMR log shows relatively consistent porosity ranging from about 2 to 4% through the Marcellus Shale interval (Figure 2-8). There is, however overall decrease in the T2 distributions, with slower T2 arrivals in the upper Marcellus (3ms and greater) and faster in most organic portion of the Lower Marcellus (<3ms). This trend could be related to a change in pore fluid type or an overall decrease in the pore size distribution.

The XRF data (Figure 2-8) provide general trends that relate the Marcellus unit to redox environment and the amount of detrital influence using relative quantities of major and trace elements, as well as, how they relate to one another. Descending through the stratigraphy, there is a decrease in detrital delivery which is represented by a decrease in aluminum. In middle and lower Marcellus, the reduction of Al corresponds with GR log and TOC peaks. The interpreted redox

conditions range from dysoxic in the upper Marcellus to anoxic to slightly euxinic in the middle and lower Marcellus. The covariance of uranium (represented by TOC_URAN) and GR log readings indicate a reducing environment. The decrease of Th/U hinges with the TOC peaks, and the Th/U values remain less than 1 indicating a suboxic to anoxic environment. These are expressed by an overall increase in the concentration of trace elements, specifically in V+Cr trends, which show denitrification (Sageman et al., 2003; Lash and Blood, 2014; Chen et al., 2015; Chen and Sharma, 2017).

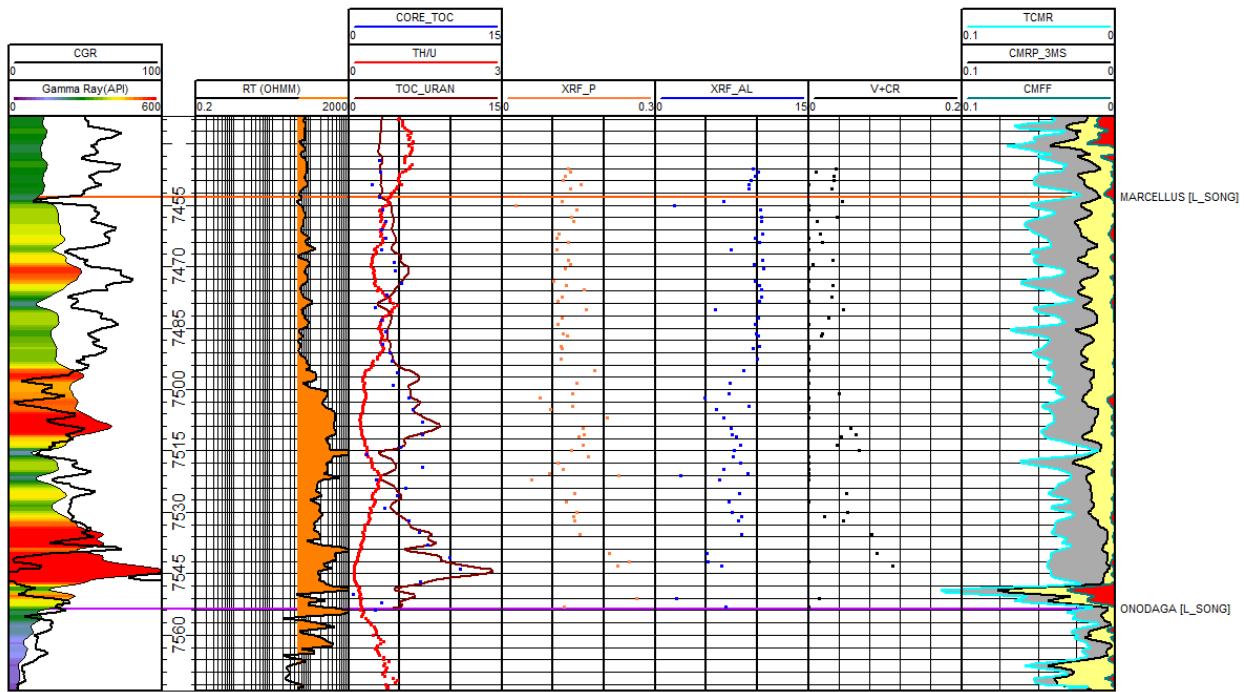


Figure 2-8. Geochemical and well-log profiles of the MIP-3H core illustrating corrected gamma ray (CGR), true resistivity (RT), SRA TOC (CORE_TOC), ratio of thorium to uranium (Th/U) derived from spectral gamma ray, TOC calculated from uranium log (TOC_URAN), phosphorus, aluminum, vanadium and chromium derived from XRF (XRF_P, XRF_AL, V+CR), and NMR log.

Conclusions

Characterizing the pore structure of unconventional reservoirs is important for understanding the storage capacity and flow regime. Low pressure N₂ adsorption is a good method to study nano-scale pore structures especially micro- and meso-pores. It can provide pore surface area and pore volume information, which represents adsorbed gas and free gas storage capacity respectively. For accurate analysis, sample preparation is critical. We recommend crushing the sample until the entire mass passes through a 60-mesh sieve to prevent potential sample biasing due to sieving, then degas the sample at 120°C for 24 hours. The results indicate that micro- to meso-pores are concentrated in the organic content. Pore volume and pore surface area both show good positive correlations with TOC. Calibrated XRD results indicate that in lower Marcellus, the volume fraction of highly nano-porous organic matter is approximately 30%, which offers significant hydrocarbon storage capacity.

Reference Cited:

- Adesida, A. G., I. Y. Akkutlu, D. E. Resasco, and C. S. Rai, 2011, SPE 147397 Kerogen Pore Size Distribution of Barnett Shale using DFT Analysis and Monte Carlo Simulations: SPE Annual Technical Conference and Exhibition, p. 1–14, doi:10.2118/147397-MS.
- Ambrose, R. J., D. Energy, R. C. Hartman, and W. Labs, 2010, SPE 131772 New Pore-scale Considerations for Shale Gas in Place Calculations: doi:10.2118/131772-MS.
- Anovitz, L. M., and D. R. Cole, 2015, Characterization and Analysis of Porosity and Pore Structures: Reviews in Mineralogy and Geochemistry, v. 80, p. 61–164, doi:10.2138/rmg.2015.80.04.
- Bai, B., M. Elgmati, H. Zhang, and M. Wei, 2013, Rock characterization of Fayetteville shale gas plays: Fuel, v. 105, p. 645–652, doi:10.1016/j.fuel.2012.09.043.
- Barrett, E. P., L. G. Joyner, and P. P. Halenda, 1951, The determination of pore volume and area distributions in porous substances. I. computations from nitrogen isotherms: Journal of the American Chemical Society, v. 73, no. 1, p. 373–380, doi:10.1021/ja01145a126.
- Bennett, R. H., N. R. O. Brien, M. H. Hulbert, O. S. Directorate, N. Oceanographic, O. S. Directorate, and N. Oceanographic, 1991, Determinants of clay microfabric signatures- Processes and mechanisms, *in* Microstructure of fine-grained sediments: New York, Springer-Verlag, p. 5–32.
- Bernard, S., L. Brown, R. Wirth, A. Schreiber, H.-M. Schulz, B. Horsfield, A. C. Aplin, and E. J. Mathia, 2013, FIB-SEM and TEM Investigations of an Organic-rich Shale Maturation Series from the Lower Toarcian Posidonia Shale, Germany: Nanoscale Pore System and Fluid-rock Interactions: Electron microscopy of shale hydrocarbon reservoirs: AAPG

- Memoir 102, p. 53–66, doi:10.1306/13391705M1023583.
- Bohacs, K. M., Q. R. Passey, M. Rudnicki, W. L. Esch, and O. R. Lazar, 2013, The Spectrum of Fine-Grained Reservoirs from “Shale Gas” to “Shale Oil”/ Tight Liquids : Essential Attributes, Key Controls, Practical Characterization: IPTC 2013: International Petroleum Technology Conference, no. Figure 1, p. 1–16, doi:10.2523/16676-MS.
- Boyce, M., A. Yanni, and T. Carr, 2010, Depositional control of organic content in the Middle Devonian Marcellus interval of West Virginia and Western Pennsylvania: Critical Assessment of ..., p. 3–6.
- Brunauer, S., P. H. Emmett, and E. Teller, 1938, Adsorption of Gases in Multimolecular Layers: Journal of the American Chemical Society, v. 60, no. 1, p. 309–319, doi:citeulike-article-id:4074706\rdoi: 10.1021/ja01269a023.
- Bustin, R. M., A. M. M. Bustin, B. Columbia, X. Cui, and D. J. K. Ross, 2008, SPE 119892 Impact of Shale Properties on Pore Structure and Storage Characteristics.
- Bustin, R. M., a Bustin, D. Ross, G. Chalmers, V. Murthy, C. Laxmi, and X. Cui, 2009, Shale Gas Opportunities and Challenges *: Search and Discovery Articles, v. 40382.
- Carr, T. R. et al., 2016, The Marcellus Shale Energy and Environment Laboratory (MSEEL)*, *in* AAPG Eastern Section Meeting, Lexington, Kentucky.
- Chalmers, G. R. L., and R. Marc Bustin, 2007, On the effects of petrographic composition on coalbed methane sorption: International Journal of Coal Geology, v. 69, no. 4, p. 288–304, doi:10.1016/j.coal.2006.06.002.
- Chalmers, G. R. L., D. J. K. Ross, and R. M. Bustin, 2012, Geological controls on matrix permeability of Devonian Gas Shales in the Horn River and Liard basins, northeastern British Columbia, Canada: International Journal of Coal Geology, v. 103, p. 120–131,

doi:10.1016/j.coal.2012.05.006.

Chen, R., and S. Sharma, 2017, Linking the Acadian Orogeny with organic-rich black shale deposition: Evidence from the Marcellus Shale: *Marine and Petroleum Geology*, v. 79, p. 149–158, doi:10.1016/j.marpetgeo.2016.11.005.

Chen, R., and S. Sharma, 2016, Role of alternating redox conditions in the formation of organic-rich interval in the Middle Devonian Marcellus Shale , Appalachian Basin , USA: *Palaeogeography, Palaeoclimatology, Palaeoecology*, v. 446, p. 85–97, doi:10.1016/j.palaeo.2016.01.016.

Chen, R., S. Sharma, T. Bank, D. Soeder, and H. Eastman, 2015, Comparison of isotopic and geochemical characteristics of sediments from a gas- and liquids-prone wells in Marcellus Shale from Appalachian Basin, West Virginia: *Applied Geochemistry*, v. 60, p. 59–71, doi:10.1016/j.apgeochem.2015.01.001.

Clarkson, C. R., J. M. Wood, S. E. Burgis, S. D. Aquino, and M. Freeman, 2012, Nanopore-structure analysis and permeability predictions for a tight gas siltstone reservoir by use of low-pressure adsorption and mercury-intrusion techniques: *SPE Reservoir Evaluation & Engineering*, v. 15, no. 6, p. 648–661, doi:10.2118/155537-PA.

Crain, E. R., and D. Holgate, 2014, A 12-Step program to reduce uncertainty in kerogen-rich reservoirs: *Canadian Well Logging Society*, v. i, no. Spring, p. 10–16.

Culligan, K. A., D. Wildenschild, B. S. B. Christensen, W. G. Gray, and M. L. Rivers, 2006, Pore-scale characteristics of multiphase flow in porous media : A comparison of air – water and oil – water experiments: *Advances in Water Resources*, v. 29, p. 227–238, doi:10.1016/j.advwatres.2005.03.021.

Culligan, K. A., D. Wildenschild, B. S. B. Christensen, W. G. Gray, M. L. Rivers, and A. F. B.

- Tompson, 2004, Interfacial area measurements for unsaturated flow through a porous medium: *Water Resources Research*, v. 40, no. W12413, p. 1–12, doi:10.1029/2004WR003278.
- Curtis, M. E., and R. J. Ambrose, 2011, Investigation of the relationship between organic porosity and thermal maturity in the Marcellus Shale, *in* SPE Conference: p. 4pp, doi:10.2118/144370-ms.
- Curtis, M. E., C. H. Sondergeld, R. J. Ambrose, and C. S. Rai, 2012, Microstructural investigation of gas shales in two and three dimensions using nanometer-scale resolution imaging: *AAPG Bulletin*, v. 96, no. 4, p. 665–677, doi:10.1306/08151110188.
- Deirieh, A., 2016, *From Clay Slurries to Mudrocks : A Cryo-SEM Investigation of the Development of the Porosity and Microstructure*: Massachusetts Institute of Technology, 226 p.
- Desbois, G., J. L. Urai, and P. A. Kukla, 2009, Morphology of the pore space in claystones – evidence from BIB/FIB ion beam sectioning and cryo-SEM observations: *eEarth Discussions*, v. 4, no. 1, p. 1–19, doi:10.5194/eed-4-1-2009.
- Dilks, A., and S. C. Graham, 1985, Quantitative Mineralogical Characterization of Sandstones by Back-scattered Electron Image Analysis: *Journal of Sedimentary Petrology*, v. 55, no. 3, p. 347–355.
- Dong, T., and N. B. Harris, 2013, Pore Size Distribution and Morphology in the Horn River Shale, Middle and Upper Devonian, Northeastern British Columbia, Canada: Electron microscopy of shale hydrocarbon reservoirs: *AAPG Memoir 102*, p. 67–80, doi:10.1306/13391706M1023584.
- Driskill, B., J. Walls, J. DeVito, and S. W. Sinclair, 2013, Applications of SEM Imaging to

- Reservoir Characterization in the Eagle Ford Shale, South Texas, U.S.A., *in* Electron microscopy of shale hydrocarbon reservoirs: AAPG Memoir 102: p. 115–136, doi:10.1306/13391709M1023587.
- EIA, U. S., 2018, Annual Energy Outlook 2018 with projections to 2050 Table of contents: Washington, DC, 74 p.
- Erdman, N., and N. Drenzek, 2013, Integrated Preparation and Imaging Techniques for the Microstructural and Geochemical Characterization of Shale by Scanning Electron Microscopy: Electron microscopy of shale hydrocarbon reservoirs: AAPG Memoir 102, p. 7–14, doi:10.1306/13391700M1023581.
- Espitalie, J., G. Deroo, and F. Marquis, 1985, La pyrolyse Rock-Eval et ses applications. Deuxième partie.: *Revue de l'Institut Français du Pétrole*, v. 40, no. 6, p. 755–784, doi:10.2516/ogst:1985045.
- Ettensohn, F. R., and T. R. Lierman, 2012, Large-scale Tectonic Controls on the Origin of Paleozoic Dark-shale Source-rock Basins: Examples from the Appalachian Foreland Basin, Eastern United States: *AAPG Bulletin*, v. 100, no. January 2012, p. 95–124, doi:10.1306/13351549M1003529.
- Fishman, N. S., J. L. Ridgley, D. K. Higley, M. L. W. Tuttle, and D. L. Hall, 2012, Ancient Microbial Gas in the Upper Cretaceous Milk River Formation, Alberta and Saskatchewan: A Large Continuous Accumulation in Fine-grained Rocks: *Shale Reservoirs —Giant Resources for the 21st Century*: AAPG Memoir 97, v. 97, p. 258–289, doi:10.1306/13321471M973493.
- Gallagher, N. C. J., and G. L. Wise, 1981, A Theoretical Analysis of the Properties of Median Filters: *IEEE Transactions on acoustic, speech, and signal processing*, v. 29, no. 6, p. 1136–

1141.

Giffin, S., R. Littke, J. Klaver, and J. L. Urai, 2013, Application of BIB-SEM technology to characterize macropore morphology in coal: *International Journal of Coal Geology*, v. 114, p. 85–95, doi:10.1016/j.coal.2013.02.009.

Hemes, S., G. Desbois, J. L. Urai, M. De Craen, and M. Honty, 2013, Variations in the morphology of porosity in the Boom Clay Formation: Insights from 2D high resolution BIB-SEM imaging and Mercury injection Porosimetry: *Geologie en Mijnbouw/Netherlands Journal of Geosciences*, v. 92, no. 4, p. 275–300, doi:doi:10.1017/S0016774600000214.

Hemes, S., G. Desbois, J. L. Urai, B. Schröppel, and J. O. Schwarz, 2015, Multi-scale characterization of porosity in Boom Clay (HADES-level, Mol, Belgium) using a combination of X-ray u-CT, 2D BIB-SEM and FIB-SEM tomography: *Microporous and Mesoporous Materials*, v. 208, p. 1–20, doi:10.1016/j.micromeso.2015.01.022.

Houben, M. E., G. Desbois, and J. L. Urai, 2014, A comparative study of representative 2D microstructures in Shaly and Sandy facies of Opalinus Clay (Mont Terri, Switzerland) inferred from BIB-SEM and MIP methods: *Marine and Petroleum Geology*, v. 49, p. 143–161, doi:10.1016/j.marpetgeo.2013.10.009.

Houben, M. E., G. Desbois, and J. L. Urai, 2013, Pore morphology and distribution in the Shaly facies of Opalinus Clay (Mont Terri, Switzerland): Insights from representative 2D BIB-SEM investigations on mm to nm scale: *Applied Clay Science*, v. 71, p. 82–97, doi:10.1016/j.clay.2012.11.006.

Huang, J., T. Cavanaugh, and B. Nur, 2013, An Introduction to SEM Operational Principles and Geologic Applications for Shale Hydrocarbon Reservoirs: *Electron microscopy of shale hydrocarbon reservoirs: AAPG Memoir 102*, p. 1–6, doi:10.1306/13391699M1023580.

- Jarvie, D. M., R. J. Hill, T. E. Ruble, and R. M. Pollastro, 2007, Unconventional shale-gas systems: The Mississippian Barnett Shale of north-central Texas as one model for thermogenic shale-gas assessment: AAPG Bulletin, v. 91, no. 4, p. 475–499, doi:10.1306/12190606068.
- Katz, A. J., and A. H. Thompson, 1985, Fractal Sandstone Pores: Implications for Conductivity and Pore Formation: Physical Review Letters, v. 54, no. 12, p. 1325–1328.
- Kelly, S., H. El-sobky, C. Torres-verdín, and M. T. Balhoff, 2016, Advances in Water Resources Assessing the utility of FIB-SEM images for shale digital rock physics: Advances in Water Resources, v. 95, p. 302–316, doi:10.1016/j.advwatres.2015.06.010.
- Klaver, J., G. Desbois, R. Littke, and J. L. Urai, 2015, BIB-SEM characterization of pore space morphology and distribution in postmature to overmature samples from the Haynesville and Bossier Shales: Marine and Petroleum Geology, v. 59, p. 451–466, doi:10.1016/j.marpetgeo.2014.09.020.
- Klaver, J., G. Desbois, J. L. Urai, and R. Littke, 2012, BIB-SEM study of the pore space morphology in early mature Posidonia Shale from the Hils area, Germany: International Journal of Coal Geology, v. 103, p. 12–25, doi:10.1016/j.coal.2012.06.012.
- Ko, L. T., R. G. Loucks, K. L. Milliken, Q. Liang, T. Zhang, X. Sun, P. C. Hackley, S. C. Ruppel, and S. Peng, 2017, Controls on pore types and pore-size distribution in the Upper Triassic Yanchang Formation , Ordos Basin , China : Implications for pore-evolution models of lacustrine mudrocks: Interpretation, v. 5, no. 2, p. 127–148, doi:10.1190/INT-2016-0115.1.
- Kuila, U., and M. Prasad, 2013, Specific surface area and pore-size distribution in clays and shales: Geophysical Prospecting, v. 61, no. 2, p. 341–362, doi:10.1111/1365-2478.12028.

- Lash, G. G., and D. R. Blood, 2014, Organic matter accumulation, redox, and diagenetic history of the Marcellus Formation, southwestern Pennsylvania, Appalachian basin: *Marine and Petroleum Geology*, v. 57, no. November, p. 244–263, doi:10.1016/j.marpetgeo.2014.06.001.
- Lash, G. G., and T. Engelder, 2011, Thickness trends and sequence stratigraphy of the Middle Devonian Marcellus Formation, Appalachian Basin: Implications for Acadian foreland basin evolution: *AAPG Bulletin*, v. 95, no. 1, p. 61–103, doi:10.1306/06301009150.
- Lazar, R., K. Bohacs, R. Klimentidis, M. Dumitrescu, and J. Ottmann, 2016, An SEM Study of Porosity in the Eagle Ford Shale of Texas—Pore Types and Porosity Distribution in a Depositional and Sequence-stratigraphic Context: *The Eagle Ford Shale: A renaissance in U.S. oil production: AAPG Memoir 110*, p. 167–186, doi:10.1306/13541961M1103589.
- Lazar, O. R., K. M. Bohacs, J. H. S. Macquaker, J. Schieber, and T. M. Demko, 2015, Capturing Key Attributes of Fine-Grained Sedimentary Rocks In Outcrops, Cores, and Thin Sections: Nomenclature and Description Guidelines: *Journal of Sedimentary Research*, v. 85, no. 3, p. 230–246.
- Loucks, R. G., R. M. Reed, S. C. Ruppel, and U. Hammes, 2012, Spectrum of pore types and networks in mudrocks and a descriptive classification for matrix-related mudrock pores: *AAPG Bulletin*, v. 96, no. 6, p. 1071–1098, doi:10.1306/08171111061.
- Loucks, R. G., R. M. Reed, S. C. Ruppel, and D. M. Jarvie, 2009, Morphology, Genesis, and Distribution of Nanometer-Scale Pores in Siliceous Mudstones of the Mississippian Barnett Shale: *Journal of Sedimentary Research*, v. 79, no. 12, p. 848–861, doi:10.2110/jsr.2009.092.
- Luffel, D. L., and F. K. Guidry, 1992, *New Core Analysis Methods for Measuring Reservoir*

- Rock Properties of Devonian Shale, *in* SPE Annual Technical Conference and Exhibition: p. 1184–1190, doi:10.2118/20571-PA.
- Mastalerz, M., A. Schimmelmann, A. Drobniak, and Y. Chen, 2013, Porosity of Devonian and Mississippian New Albany Shale across a maturation gradient: Insights from organic petrology, gas adsorption, and mercury intrusion: AAPG Bulletin, v. 97, no. 10, p. 1621–1643, doi:10.130/04011312194.
- Matthew, B. L., and T. R. Carr, 2009, Lithostratigraphy and Petrophysics of the Devonian Marcellus Interval in West Virginia and Southwestern Pennsylvania.
- Milliken, K. L., and R. J. Day-Stirrat, 2013, Cementation in mudrocks: Brief review with examples from cratonic basin mudrocks: AAPG Memoir, v. 103, p. 133–150, doi:10.1306/13401729H5252.
- Milliken, K. L., R. J. Day-Stirrat, P. K. Papazis, and C. Dohse, 2012, Carbonate Lithologies of the Mississippian Barnett Shale, Fort Worth Basin, Texas: Shale reservoirs—Giant resources for the 21st century, p. 290–321, doi:10.1306/13321473M97252.
- Milliken, K. L., W. L. Esch, R. M. Reed, and T. Zhang, 2012, Grain assemblages and strong diagenetic overprinting in siliceous mudrocks, Barnett Shale (Mississippian), Fort Worth Basin, Texas: AAPG Bulletin, v. 96, no. 8, p. 1553–1578, doi:10.1306/12011111129.
- Milliken, K. L., L. T. Ko, M. Pommer, and K. M. Marsaglia, 2014, Sem Petrography of Eastern Mediterranean Sapropels: Analogue Data For Assessing Organic Matter In Oil and Gas Shales: Journal of Sedimentary Research, v. 84, no. 11, p. 961–974, doi:10.2110/jsr.2014.75.
- Milliken, K. L., and T. Olson, 2016, Amorphous and Crystalline Solids as Artifacts in SEM Images: p. 1–8, doi:10.1306/13592013M112252.

- Milliken, K. L., and R. M. Reed, 2010, Multiple causes of diagenetic fabric anisotropy in weakly consolidated mud , Nankai accretionary prism , IODP Expedition 316: *Journal of Structural Geology*, v. 32, no. 12, p. 1887–1898, doi:10.1016/j.jsg.2010.03.008.
- Milliken, K. L., M. Rudnicki, D. N. Awwiller, and T. Zhang, 2013, Organic matter-hosted pore system, Marcellus Formation (Devonian), Pennsylvania: *AAPG Bulletin*, v. 97, no. 2, p. 177–200, doi:10.1306/072312I2O48.
- Mosher, K., J. He, Y. Liu, E. Rupp, and J. Wilcox, 2013, Molecular simulation of methane adsorption in micro- and mesoporous carbons with applications to coal and gas shale systems: *International Journal of Coal Geology*, v. 109–110, p. 36–44, doi:10.1016/j.coal.2013.01.001.
- Nole, M., H. Daigle, K. L. Milliken, and M. Prodanovic, 2016, A method for estimating microporosity of fine-grained sediments and sedimentary rocks via scanning electron microscope image analysis: *Sedimentology*, v. 63, no. 6, p. 1507–1521, doi:10.1111/sed.12271.
- Olson, E., 2012, The Importance of Sample Preparation when Measuring Specific Surface Area: *Journal of GXP Compliance*, v. 16, no. 3, p. 52~62.
- Otsu, N., 1979, A Threshold Selection Method from Gray-Level Histograms: *IEEE Transactions on Systems, Man, and Cybernetics*, v. 19, no. 1, p. 62–66, doi:10.1109/TSMC.1979.4310076.
- Passey, Q. R., K. M. Bohacs, W. L. Esch, R. E. Klimentidis, and S. K. Sinha, 2012, My source rock is now my reservoir - geologic and petrophysical characterization of shale-gas reservoirs: *Search and Discovery*, v. 80231, no. 80231, p. 47pp.
- Phansalkart, N., S. More, A. Sabale, and M. Joshi, 2011, Adaptive Local Thresholding for

Detection of Nuclei in Diversity Stained Cytology Images, *in* International Conference on Communications and Signal Processing: p. 218–220.

Pommer, M., and K. Milliken, 2015, Pore types and pore-size distributions across thermal maturity, Eagle Ford Formation, southern Texas: AAPG Bulletin, v. 99, no. 9, p. 1713–1744, doi:10.1306/03051514151.

Reed, R. M., R. G. Loucks, and S. C. Ruppel, 2014, Comment on “ Formation of nanoporous pyrobitumen residues during maturation of the Barnett Shale (Fort Worth Basin) ” by Bernard et al . (2012): International Journal of Coal Geology, v. 127, p. 111–113, doi:10.1016/j.coal.2013.11.012.

Ross, D. J. K., and R. M. Bustin, 2008a, Characterizing the shale gas resource potential of Devonian-Mississippian strata in the Western Canada sedimentary basin: Application of an integrated formation evaluation: AAPG Bulletin, v. 92, no. 1, p. 87–125, doi:10.1306/09040707048.

Ross, D. J. K., and R. M. Bustin, 2008b, Characterizing the shale gas resource potential of Devonian-Mississippian strata in the Western Canada sedimentary basin: Application of an integrated formation evaluation: AAPG Bulletin, v. 92, no. 1, p. 87–125, doi:10.1306/09040707048.

Ross, D. J. K., and R. M. Bustin, 2009, The importance of shale composition and pore structure upon gas storage potential of shale gas reservoirs: Marine and Petroleum Geology, v. 26, no. 6, p. 916–927, doi:10.1016/j.marpetgeo.2008.06.004.

Ross, D. J. K., and R. M. Bustin, 2009, The importance of shale composition and pore structure upon gas storage potential of shale gas reservoirs: Marine and Petroleum Geology, v. 26, no. 6, p. 916–927, doi:10.1016/j.marpetgeo.2008.06.004.

- Ross, D. J. K., and R. Marc Bustin, 2007, Impact of mass balance calculations on adsorption capacities in microporous shale gas reservoirs: *Fuel*, v. 86, no. 17–18, p. 2696–2706, doi:10.1016/j.fuel.2007.02.036.
- Sageman, B. B., A. E. Murphy, J. P. Werne, C. A. Ver Straeten, D. J. Hollander, and T. W. Lyons, 2003, A tale of shales: The relative roles of production, decomposition, and dilution in the accumulation of organic-rich strata, Middle-Upper Devonian, Appalachian basin: *Chemical Geology*, v. 195, no. 1–4, p. 229–273, doi:10.1016/S0009-2541(02)00397-2.
- Saidian, M., L. J. Godinez, and M. Prasad, 2016, Effect of clay and organic matter on nitrogen adsorption specific surface area and cation exchange capacity in shales (mudrocks): *Journal of Natural Gas Science and Engineering*, v. 33, p. 1095–1106, doi:10.1016/j.jngse.2016.05.064.
- Saidian, M., L. J. Godinez, and M. Prasad, 2015, Effect of Clay and Organic Matter on Nitrogen Adsorption Specific Surface Area and Cation Exchange Capacity in Shales (Mudrocks): *Annual Logging Symposium*, v. 56, p. 1–16.
- Sauvola, J., and M. Pietikainen, 2000, Adaptive document image binarization: *Pattern recognition*, v. 33, p. 225–236.
- Schieber, J., 2010, Common Themes in the Formation and Preservation of Intrinsic Porosity in Shales and Mudstones - Illustrated with Examples Across the Phanerozoic: *SPE Unconventional Gas Conference*, p. 10, doi:10.2118/132370-MS.
- Schieber, J., 2013, SEM Observations on Ion-milled Samples of Devonian Black Shales from Indiana and New York: The Petrographic Context of Multiple Pore Types: *Electron microscopy of shale hydrocarbon reservoirs: AAPG Memoir 102*, no. April 2010, p. 153–172, doi:10.1306/13391711M1023589.

- Schindelin, J. et al., 2012, Fiji: an open source platform for biological image analysis.: Nature Methods, v. 9, no. 7, p. 676–682, doi:10.1038/nmeth.2019.Fiji.
- Schindelin, J., C. T. Rueden, M. C. Hiner, and K. W. Eliceiri, 2015, The ImageJ ecosystem: An open platform for biomedical image analysis: Molecular Reproduction and Development, v. 82, no. 7–8, p. 518–529, doi:10.1002/mrd.22489.
- Schneider, J., P. B. Flemings, R. J. Day-Stirrat, and J. T. Germaine, 2011, Insights into pore-scale controls on mudstone permeability through resedimentation experiments: Geology, v. 39, no. 11, p. 1011–1014, doi:10.1130/G32475.1.
- Schneider, C. a, W. S. Rasband, and K. W. Eliceiri, 2012, NIH Image to ImageJ: 25 years of image analysis: Nature Methods, v. 9, no. 7, p. 671–675, doi:10.1038/nmeth.2089.
- Sezgin, M., and B. Sankur, 2004, Survey over image thresholding techniques and quantitative performance evaluation: Journal of Electronic Imaging, v. 13, no. 1, p. 146–168, doi:10.1117/1.1631316.
- Sing, K., 2001, The use of nitrogen adsorption for the characterisation of porous materials: Colloids and Surfaces A: Physicochemical and Engineering Aspects, v. 187–188, p. 3–9, doi:10.1016/S0927-7757(01)00612-4.
- Sing, K. S. W., D. H. Everett, R. a. W. Haul, L. Moscou, R. a. Pierotti, J. Rouquérol, and T. Siemieniewska, 1982, Reporting Physisorption Data for Gas / Solid Systems with Special Reference to the Determination of Surface Area and Porosity: Pure and Applied Chemistry, v. 57, no. 4, p. 603–619, doi:10.1351/pac198557040603.
- Sing, K. S. W., and R. T. Williams, 2004, Physisorption hysteresis loops and the characterization of nanoporous materials: Adsorption Science and Technology, v. 22, no. December 2015, p. 773–782, doi:10.1260/0263617053499032.

- Slatt, R. M., and N. R. O'Brien, 2013, Microfabrics Related to Porosity Development, Sedimentary and Diagenetic Processes, and Composition of Unconventional Resource Shale Reservoirs as Determined by Conventional Scanning Electron Microscopy: Electron microscopy of shale hydrocarbon reservoirs: AAPG Memoir 102, p. 37–44, doi:10.1306/13391703M102441.
- Slatt, R. M., and N. R. O'Brien, 2011, Pore types in the Barnett and Woodford gas shales: Contribution to understanding gas storage and migration pathways in fine-grained rocks: AAPG Bulletin, v. 95, no. 12, p. 2017–2030, doi:10.1306/03301110145.
- Soeder, D. J., 2017, The Development of Natural Gas from the Marcellus Shale: Boulder, Colorado, The Geological Society of America, 143 p.
- Sondergeld, C. H., R. J. Ambrose, C. S. Rai, and J. Moncrieff, 2010, Micro-structural studies of gas shales: Society of Petroleum Engineers Unconventional Gas Conference, SPE Paper 131771, p. 17, doi:10.2118/131771-MS.
- Song, L., T. Paronish, V. Agrawal, B. Hupp, and S. Sharma, 2017, Depositional Environment and Impact on Pore Structure and Gas Storage Potential of Middle Devonian Organic Rich Shale, Northeastern West Virginia, Appalachian Basin, *in* Unconventional Resources Technology Conference (URTeC:2667397): doi:10.15530/urtec-2017-2667397.
- Strapoć, D., M. Mastalerz, A. Schimmelmann, A. Drobniak, and N. R. Hasenmueller, 2010, Geochemical constraints on the origin and volume of gas in the New Albany Shale (Devonian-Mississippian), eastern Illinois Basin: AAPG Bulletin, v. 94, no. 11, p. 1713–1740, doi:10.1306/06301009197.
- Thommes, M., K. Kaneko, A. V. Neimark, J. P. Olivier, F. Rodriguez-Reinoso, J. Rouquerol, and K. S. W. Sing, 2015, Physisorption of gases, with special reference to the evaluation of

- surface area and pore size distribution (IUPAC Technical Report): Pure and Applied Chemistry, v. 87, no. 9–10, p. 1051–1069, doi:10.1515/pac-2014-1117.
- Tian, H., L. Pan, X. Xiao, R. W. T. Wilkins, Z. Meng, and B. Huang, 2013, A preliminary study on the pore characterization of Lower Silurian black shales in the Chuandong Thrust Fold Belt, southwestern China using low pressure N₂ adsorption and FE-SEM methods: Marine and Petroleum Geology, v. 48, p. 8–19, doi:10.1016/j.marpetgeo.2013.07.008.
- Velde, B., 1996, Compaction trends of clay-rich deep sea sediments: Marine Geology, v. 133, p. 193–201.
- Walls, J. D., and E. Diaz, 2011, Relationship of shale porosity- permeability trends to pore type and organic content: Petrophysics in Tight Oil Workshop.
- Wang, G., and T. R. Carr, 2013, Organic-rich marcellus shale lithofacies modeling and distribution pattern analysis in the appalachian basin: AAPG Bulletin, v. 97, no. 12, p. 2173–2205, doi:10.1306/05141312135.
- Wang, G., Y. Ju, Z. Yan, and Q. Li, 2015, Pore structure characteristics of coal-bearing shale using fluid invasion methods: A case study in the Huainan-Huaibei Coalfield in China: Marine and Petroleum Geology, v. 62, p. 1–13, doi:10.1016/j.marpetgeo.2015.01.001.
- Wildenschild, D., and A. P. Sheppard, 2013, X-ray imaging and analysis techniques for quantifying pore-scale structure and processes in subsurface porous medium systems: Advances in Water Resources, v. 51, p. 217–246, doi:10.1016/j.advwatres.2012.07.018.
- Yu, W., K. Sepehrnoori, and T. W. Patzek, 2016, Modeling Gas Adsorption in Marcellus Shale With Langmuir and BET Isotherms.: SPE Journal, v. 21, no. 2, p. 589–600, doi:10.2118/170801-PA.
- Zagorski, W. a., G. R. Wrightstone, and D. C. Bowman, 2012, The Appalachian Basin Marcellus

Gas Play: Its History of Development, Geologic Controls on Production, and Future Potential as a World-class Reservoir, *in* AAPG Memoir 97: Shale Reservoirs-Giant Resources for the 21st Century: p. 172–200, doi:10.1306/13321465M973491.

Zhang, T., G. S. Ellis, S. C. Ruppel, K. Milliken, and R. Yang, 2012, Organic Geochemistry Effect of organic-matter type and thermal maturity on methane adsorption in shale-gas systems: *Organic Geochemistry*, v. 47, p. 120–131, doi:10.1016/j.orggeochem.2012.03.012.

Zhang, S., R. E. Klimentidis, and P. Barthelemy, 2011, Porosity and permeability analysis on nanoscale FIB-SEM 3D imaging of shale rock, *in* International Symposium of the Society of Core Analysis: p. 1–12.

Chapter III

Porosity and Storage Capacity of Middle Devonian Shale Across a Maturation Gradient

Liaosha Song, Keithan Martin, Timothy R. Carr, Payam Kavousi Ghahfarokhi

Department of Geology and Geography, West Virginia University, Morgantown, WV

Email: liaoshasong@gmail.com

Abstract

Porosity and pore size distribution (PSD) are critical reservoir parameters. Pore surface area, pore volume, PSD, and porosity were measured using subcritical nitrogen (N₂) adsorption, and helium porosimetry. The evolution of porosity in shale with increasing maturity was examined in a suite of 17 Devonian shale samples from 4 wells in the Appalachian basin of Pennsylvania and West Virginia. The thermal maturity of the tested samples covers a wide range in the hydrocarbon generation sequence from wet gas/condensate zone ($R_o = 1.16\%$) to post mature zone ($R_o = 2.79\%$). Shale samples from the Mahantango Formation and Marcellus Shale samples used in this study have total organic carbon contents from 0.41 to 7.88 wt.%. Results indicate that total organic carbon (TOC) has the strongest effect on porosity and pore structure. The presence of organic matter in shale strongly enhances the storage capacity by increasing the specific surface area and pore volume, which represents sorption storage capacity and free-gas storage capacity. Differences in porosity and pore structure have a complex relationship to thermal maturity, micro texture, mineralogy, clay content and TOC.

Keywords: porosity, pore size distribution, the Marcellus Shale, pore structure, storage capacity, shale gas reservoirs

1. Introduction

The performance of a shale reservoir depends on the pore systems for storing and releasing hydrocarbon gas. Porosity and pore size distribution are widely used to characterize pore structure (Ross and R. Mark Bustin, 2009). The pore-throat size in shale reservoirs ranges from submicron to nanometer scale, which is significantly smaller than that of conventional reservoirs (Nelson, 2009). As a result, a variety of pore sizes and fluid flow regime occur in shales, from

Darcy flow in large connected pores to slippage and Knudsen diffusion in nanometer-scale organic matter (OM) hosted pores (Javadpour, 2009; Mastalerz et al., 2013; Sondergeld et al., 2010). The heterogeneity of fine-grained strata and the wide distribution of pore sizes make it challenging to evaluate a shale reservoir. Many geologic factors have been considered to shed light on the pore structure, such as total organic carbon (TOC), mineralogy, thermal maturity, and grain assemblage (Chalmers and Marc Bustin, 2007; Ross and Marc Bustin, 2007; Ross and Bustin, 2008a; Ross and R. Marc Bustin, 2009; Chalmers et al., 2012; Kuila and Prasad, 2013).

Several shale units deposited during Middle Devonian in the Appalachian basin. The Marcellus Shale is an organic rich shale formation at the bottom section of Hamilton Group, which spans 95,000 square miles across six states in northeastern US (EIA, 2017). There is another shale formation above the Marcellus Shale, namely Mahantango Formation. The Marcellus shale was considered as a source-rock formation during the early development of gas plays in the Appalachian basin during 1930s to 1960s (Zagorski et al., 2012). The study of the Marcellus Shale as a target reservoir started with the Eastern Gas Shales Project funded by the US Department of Energy during late 1970s through the 1980s (Zagorski et al., 2012; Soeder, 2017). Early studies about the porosity and permeability of the Middle Devonian shales reveal that organic matter content and thermal maturity influence the potential productivity (Soeder, 1988; Davies et al., 1991; Luffel and Guidry, 1992). The introduction of horizontal drilling and hydraulic fracturing techniques enabled the economic production of a series of shale reservoirs including the Marcellus Shale (Zagorski et al., 2012; Soeder, 2017).

Organic matter hosted porosity has been considered as the dominant gas storage mechanism of shale hydrocarbon reservoirs (Ross and Bustin, 2009). Milliken et al. (2013) studied a set of samples at a thermal maturity between an Ro of 1.0 and 2.1% in the Marcellus Shale of northern

Pennsylvania, and found that variation of TOC is a stronger control on the character of OM-hosted pore systems than variation in thermal maturity, especially at the lower end of TOC range (~5.6 wt.%) (Milliken et al., 2013). Gu et al. (2015) investigated the porosity of Marcellus Shale from a core drilled in Centre County, Pennsylvania, USA, using ultra small-angle neutron scattering (USANS), small-angle neutron scattering (SANS), FIB-SEM, and nitrogen gas adsorption. They argue that the dominant nanometer sized pores in organic-poor, clay-rich shale samples are water-accessible sheet-like pores within clay aggregates. On the contrary, organic matter hosted pores dominate organic-rich sample (Gu et al., 2015).

Numerous studies about the evolution of organic matter hosted porosity with thermal maturation have been conducted with different methodologies, yet this question is still not well understood. Although the organic matter hosted porosity is created during thermal crack of kerogen and generation of hydrocarbon (Jarvie et al., 2007; Loucks et al., 2009; Bernard et al., 2012), maturity alone is not a reliable predictor of porosity in organic matter, and other factors such as the composition organic matter could also influence the generation of organic matter hosted porosity. Curtis et al. (2011) analyzed two Marcellus Shale samples with vitrinite reflectance of 1.1% and over 3.1%, using focused ion beam (FIB) milling and scanning electron microscopy (SEM). They found no correlation between thermal maturity and OM hosted porosity. Besides, the preservation is also an important factor, because OM is normally less resistant towards mechanical compaction (Pommer and Milliken, 2015). Mastalerz et al. (2013) examined five New Albany Shale samples with a maturity range from immature to post mature and emphasize the importance of mineralogical composition toward porosity. Instead of a linear correlation, they conclude that the evolution of OM hosted porosity follows a trough-shaped path

in response to hydrocarbon generation and migration events. A systematic study of porosity and storage capacity evolution through thermal maturation is in need.

In this study, we selected a suite of core samples from Mahantango Formation and the Marcellus Shale covering a range from wet gas (R_o 1.16%) to post mature (R_o 2.79%). The focus of this study is to get a better understanding of the evolution of porosity and storage capacity through thermal maturation.

2. Materials and Methods

2.1 Materials

Seventeen core samples were collected from four wells penetrating Mahantango and Marcellus shale units, in West Virginia and Pennsylvania (Figure 3-1, 3-2). Table 3-1 lists the samples analyzed in this research, including the formations from which they were sampled, total organic carbon (TOC), and thermal maturity (represented by vitrinite reflectance, R_o). Four samples were taken from CS1 at Clearfield County, Pennsylvania, four samples were taken from SW1 at Greene County, Pennsylvania, three samples were taken from G55, and five samples were taken from A1, West Virginia. The mudrock samples were selected to cover a range of maturities from R_o 1.16 to 2.79%, which represents a range from the condensate zone to the post-mature zone. Some samples are from the same wells and depths as the samples that were studied extensively in previous research at the Department of Geology and Geography, West Virginia University (Song et al., 2017.; Wang and Carr, 2013; Chen and Sharma, 2016). This helped us during the selection of samples in this research. Samples represent a wide range of mineralogical composition and organic-matter content, and represent the Mahantango and Marcellus shale units relatively well.

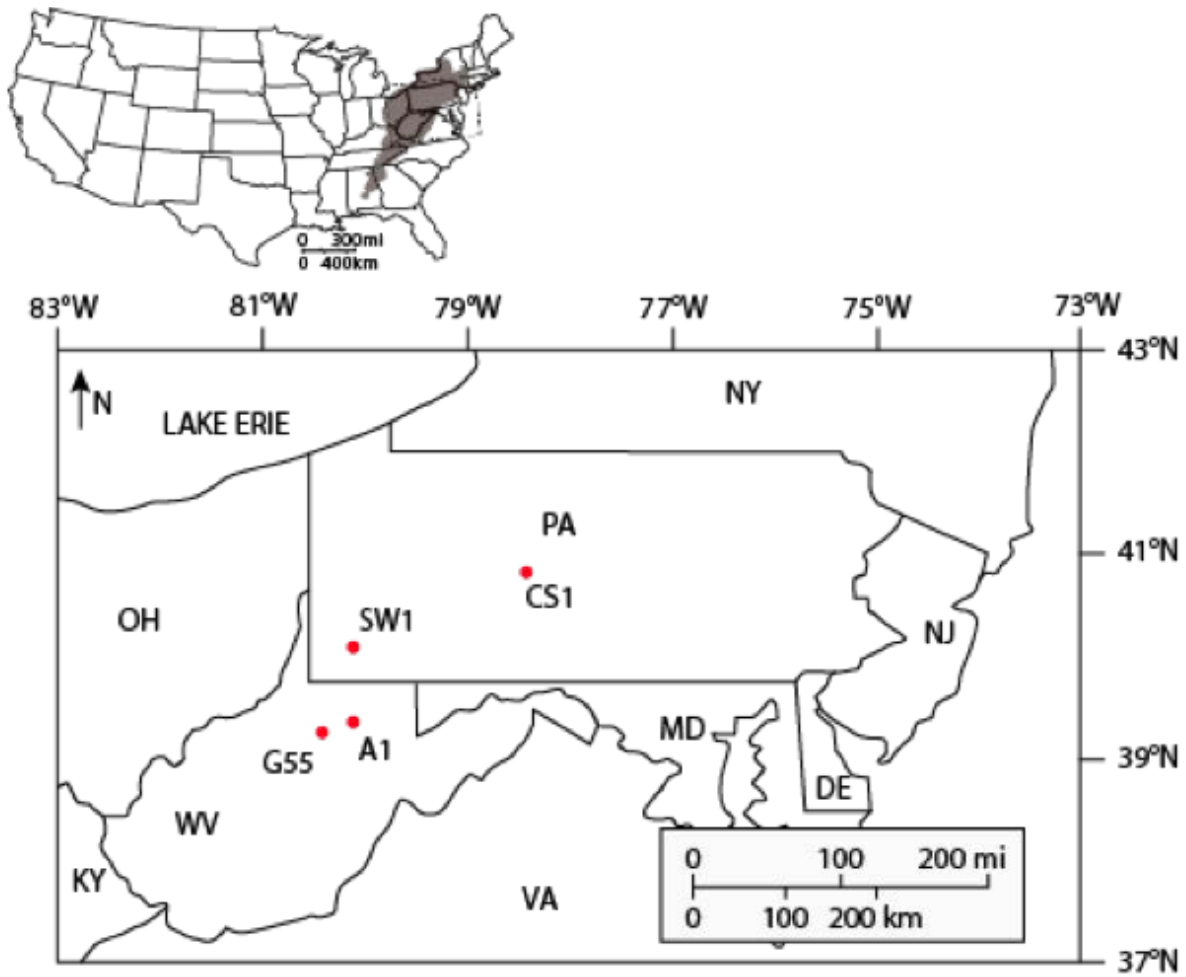


Figure 3-1. Locations of the four study wells.

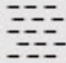
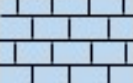





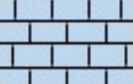
Series	Stage	Stratigraphy		Lithology	
Middle Devonian	Givetian	Geneseo Shale			
		Tully Limestone			
		Hamilton Group	Mahantango Shale		
			Marcellus Shale	Oatka	
	Purcell Limestone				
	Creek				
	Cherry Valley				
	Eifelian		Onondaga Limestone		

Figure 3-2. Stratigraphy of the study area.

Table 3-1. Vitrinite reflectance (R_o), total organic carbon (TOC) content, depth, and formation of shale samples.

Sample name	Well #	Depth (ft)	Formation	TOC (wt.%)	R_o (%)
G55-1	G55	7099.00	Mahantango	0.65	1.36
G55-2	G55	7149.50	Marcellus	4.28	1.36
G55-3	G55	7211.00	Marcellus	5.91	NA
A1-1	A1	7555.00	Mahantango	2.10	1.40
A1-2	A1	7605.00	Mahantango	2.24	1.38
A1-3	A1	7714.00	Marcellus	4.34	1.46
A1-4	A1	7734.00	Marcellus	5.84	NA
A1-5	A1	7765.00	Marcellus	5.12	1.41
CS1-1	CS1	7019.00	Mahantango	1.80	2.59
CS1-2	CS1	7070.00	Marcellus	2.33	2.67
CS1-3	CS1	7099.50	Marcellus	7.28	2.68
CS1-4	CS1	7128.00	Marcellus	4.28	2.79
CS1-5	CS1	7145.00	Marcellus	6.20	NA
SW1-1	WS1	7742.00	Mahantango	0.41	1.25
SW1-2	WS1	7852.00	Marcellus	4.66	1.16
SW1-3	WS1	7873.00	Marcellus	4.80	1.18
SW1-4	WS1	7891.00	Marcellus	7.88	NA

2.2 Subcritical Nitrogen Adsorption

Subcritical N_2 adsorption was conducted on a Micromeritics ASAP-2020 instrument at -196°C (77K). About 1 gram of shale sample was crushed with mortar and pestle until the whole mass passes through a 60-mesh sieve to prevent potential sample biasing due to sieving. Then samples were set under high-vacuum at 120°C for 24 hours to remove adsorbed water and volatile matter prior to analyses with N_2 . Forty-three relative-pressure (P/P_0) points ranging from 0.009 to 0.990 were measured on both adsorption and desorption branches. The adsorption branch of the isotherms from samples was used to obtain information about micropores (<2 nm in diameter) and mesopores (2~50 nm in diameter). The classification of pore sizes used in this article follows the classification system of the International Union of Pure and Applied

Chemistry. This classification of pore sizes has proven to be very convenient in coal and shale studies (Ross and Bustin, 2008a; Clarkson et al., 2012; Kuila and Prasad, 2013; Mastalerz et al., 2013). Specific surface area (SSA) was calculated based on Brunauer-Emmet-Teller (BET) theory (Brunauer et al., 1938). Pore volumes, and pore distributions based on Barrett-Joyner-Halenda (BJH) model, t-Plot, H-K model (Brunauer et al., 1938; Barrett et al., 1951; Sing, 2001). A detailed description of these theories and techniques can be found in Sing et al., 1982 and Thommes et al., 2015.

2.3 Porosity

The porosity was measured using the Gas Research Institute (GRI) helium porosimetry on crushed core samples (Luffel and Guidry, 1992), and was conducted by Core Laboratories in Houston, Texas. The bulk volume is determined by Archimedes' principle with mercury immersion, and grain volume is determined using Boyle's Law with helium expansion. Pore fluids were removed by Dean Stark extraction, and crushed samples (20 to 35 mesh) were dried at 110°C. Porosity is calculated based on the difference between bulk volume and grain volume.

2.4 Mineralogical Composition

Mineralogical composition is quantified with X-ray Diffraction (XRD). The samples were ground in a steel grinding container to ultrafine particle size and pressed into chemplex pellets. XRD was performed with a PANalytical X'Pert Pro X-ray Diffractometer at Shared Research Facilities of West Virginia University. The original spectra were interpreted using the X'Pert HighScore Plus Program.

2.5 Additional Data

TOC is determined with approximately 60 to 100 mg of pulverized mudrock sample in the Source Rock Analyzer (SRA) at the National Energy Technology Laboratory (NETL). Vitrinite

reflectance (R_o) was provided by Core Laboratories in Houston, TX as shared in part with a joint industry project, the Marcellus Shale Consortium.

3. Results

3.1 Mineralogy, Total Organic Carbon, and Porosity

The compositions determined via XRD demonstrate a very wide distribution in mineralogy for this sample suite (Table 3-2 and Figure 3-3). Quartz and clay minerals are the major constituents in most of the samples in this research. Sample CS1-2 was also taken from a carbonate rich layer, which contains 36.8% carbonate (calcite and dolomite). Clay minerals (dominately illite and chlorite) are dominant in most of the Mahantango samples (G55-1, A1-1, A1-2, CS1-1, and SW1-1). A1-2 is from the lower part of Mahantango Formation, and it shows nearly equal percentages of quartz and total clay, 46.6% and 40.5% respectively. The contents of different clay minerals also vary in different samples. In samples from well G55, A1, and SW1, illite and mica exceeded chlorite, whereas in well CS1 chlorite is the major clay mineral. The Union Spring Member is the most organic-rich section of the Marcellu Shale. Samples G55-3, A1-4, SW1-1, and SW1-2 show no chlorite, while sample CS1-4 with a similar organic content level with the previous mentioned four samples shows 30.6% chlorite.

Table 3-2. Mineralogy Composition of Shale Samples in Volume Percentage.

Sample #	Quartz	K-Feldspar	Plagioclase	Calcite	Dolomite	Pyrite	Kerogen	Illite & Mica	Chlorite
G55-1	36.3	0.6	5.0	3.9	0.7	0.5	1.5	33.2	18.4
G55-2	47.4	0.0	3.1	1.9	0.0	3.3	9.5	27.6	7.1
G55-3	49.8	0.0	3.0	10.1	0.0	3.9	12.9	20.3	0.0
A1-1	37.3	0.7	5.5	0.0	0.0	2.4	4.8	33.8	15.5
A1-2	46.2	0.0	4.4	0.7	0.0	2.9	5.1	27.7	12.8
A1-3	33.1	0.0	4.1	5.5	1.9	8.4	10.0	37.0	0.0
A1-3	53.3	0.0	2.9	1.7	1.4	4.1	12.8	23.9	0.0
A1-4	57.8	0.0	2.2	3.3	1.6	5.9	11.5	17.8	0.0
CS1-1	37.8	0.7	5.4	0.3	0.8	0.6	4.1	18.4	32.1
CS1-2	24.8	0.5	2.5	32.0	3.4	2.7	5.3	9.1	19.7
CS1-3	29.9	0.5	4.8	0.5	0.3	5.8	16.0	10.7	31.5
CS1-4	32.9	0.0	4.0	11.7	1.5	6.9	10.0	7.5	25.5
CS1-5	35.1	0.6	4.5	2.3	0.8	4.6	13.8	7.8	30.6
SW1-1	37.1	1.5	5.7	4.0	2.6	0.3	0.6	35.4	12.8
SW1-2	41.9	0.7	4.7	2.3	1.5	4.3	10.4	31.1	3.1
SW1-3	35.9	1.1	5.9	8.3	0.6	8.8	11.1	28.3	0.0
SW1-4	49.4	0.6	3.2	11.4	0.9	6.0	17.2	11.3	0.0

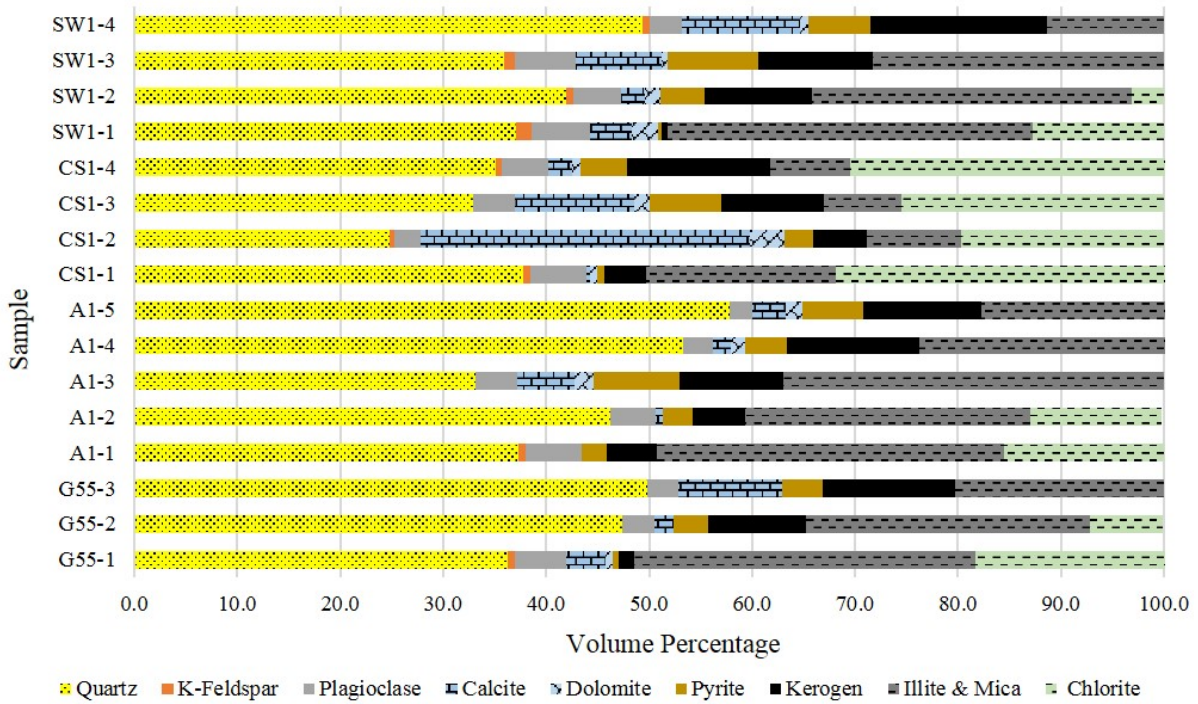


Figure 3-3. Mineralogical composition of shale samples in volume percentage, data from Table 3-2.

The TOC ranges from 0.41 to 2.24% in samples from Mahantango Formation. While in the Marcellus Shale, it ranges from 1.94 to 7.88%. Generally, the TOC of Marcellus Shale is significantly higher than Manhantango Formation, and that of lower Marcellus (Union Springs Member) is higher than the upper Marcellus (Oakta Creek Member).

Helium porosimetry was employed to provide comparative values for grain density, bulk sample density, and total porosity (Table 3-3). The porosity ranges from 1.95% for sample A1-2 to 7.56% for sample G55-2.

Table 3-3. Bulk density, grain density, and GRI porosity of shale samples.

Sample #	Bulk Density (g/cm³)	Grain Density (g/cm³)	GRI Porosity (%)
G55-1	2.65	2.75	4.33
G55-2	2.48	2.66	7.56
G55-3	2.39	2.56	7.32
A1-1	2.66	2.77	4.66
A1-2	2.70	2.74	1.95
A1-3	2.52	2.69	7.00
A1-4	2.47	2.61	6.06
A1-5	2.46	2.60	6.04
CS1-1	2.63	2.77	6.06
CS1-2	2.62	2.75	5.77
CS1-3	2.59	2.83	9.32
CS1-4	2.60	2.76	6.97
CS1-5	2.61	2.73	5.92
SW1-1	2.70	2.78	3.61
SW1-2	2.55	2.68	5.77
SW1-3	2.53	2.67	6.22
SW1-4	2.45	2.63	7.41

3.2 Nitrogen Adsorption

N₂ adsorption at -196°C is used to investigate pore volume and pore surface area. Both adsorption and desorption branches were collected, and the adsorption branch is used for calculating the surface area and pore volume. All samples exhibit similar isotherm and hysteresis loops (Figure 3-4). All the isotherms are classified as type IV with hysteresis loops according to IUPAC classification, indicating the existence of meso-porosity and slit-shape pores (Sing and Williams, 2004; Thommes et al., 2015). Among all the samples, Marcellus samples show better capability of adsorbing nitrogen than Mahantango samples (Figure 3-4). Sample A1-4 exhibits the highest capacity of nitrogen adsorption. According to IUPAC, 1985, the N₂ adsorption isotherms of all the samples in this research are type IV with type H4 hysteresis (Figure 3-4). The presence of a hysteresis loops is usually attributed to capillary condensation in mesopore

structures ($2\text{nm} < \text{pore size} < 50\text{nm}$) (Sing et al., 1982; Sing, 2001; Sing and Williams, 2004; Thommes et al., 2015), which in this case indicates the existence of mesopores in shale reservoir. Moreover, the H4 hysteresis loops are mainly associated with narrow slit-like pores which have both meso-porosity and microporosity (Sing et al., 1982).

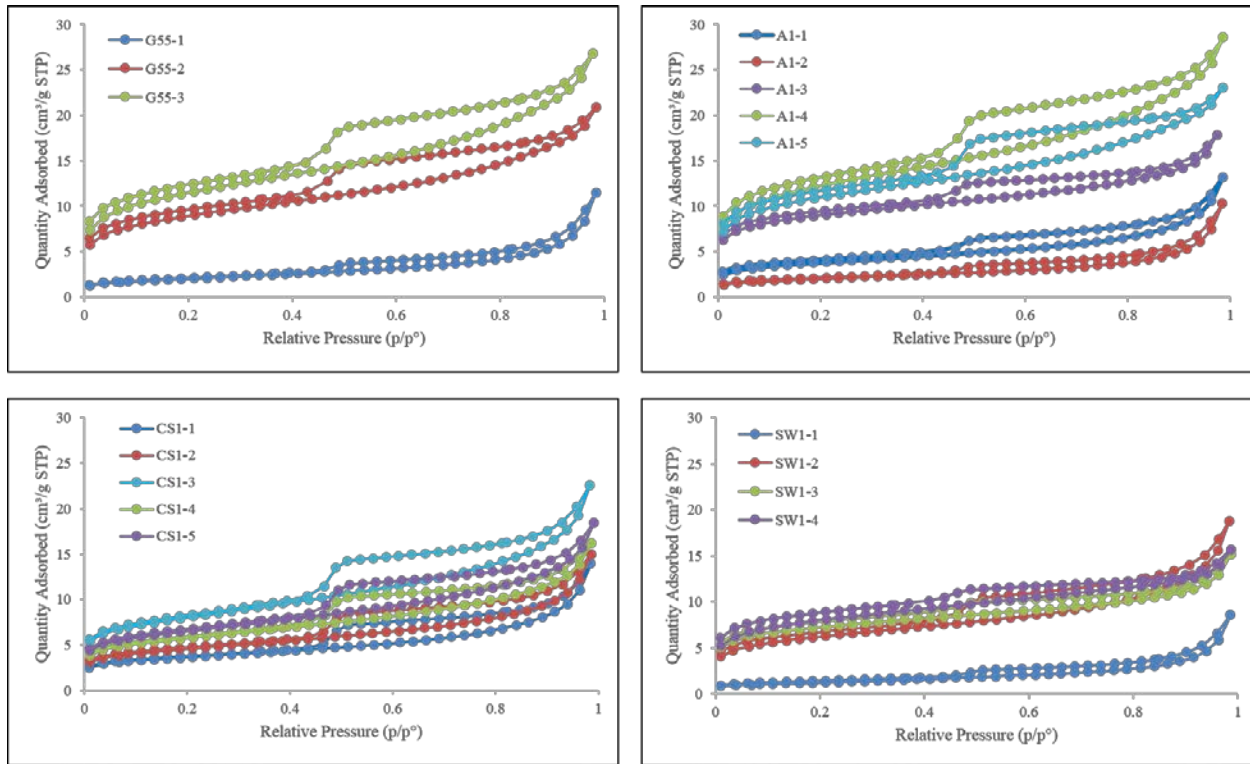


Figure 3-4. Nitrogen adsorption isotherms of samples.

BET specific surface area (SSA), BJH pore volume, t-plot pore volume, BJH pore diameter, and average pore width are calculated from N_2 adsorption analysis (Table 3-4), and the results show a wide range of distribution. The average SSA of Mahantango is $8.98 \text{ m}^2/\text{g}$, while the average SSA of Marcellus is $29.63 \text{ m}^2/\text{g}$. The average BJH pore volume of Mahantango is $0.018 \text{ cm}^3/\text{g}$, while the average pore volume of Marcellus is $0.032 \text{ cm}^3/\text{g}$. Overall, the pore volume does not change as significantly as pore surface area, mainly because smaller pores (pore size

smaller than 5 nm) does not contribute very much to pore volume, but make a significant difference in the pore surface area (Song et al., in prep). The smallest specific surface area in this research is 4.2921 m²/g from sample SW1-1, and the highest SSA is 43.6434 m²/g from sample A1-4. The micropore volume is represented by the t-plot volume. The Mahantango samples have smaller micropore volumes, while Marcellus samples has larger micropore volumes.

Table 3-4. Pore structure parameters determined via N₂ adsorption.

Sample	S_{BET} (m²/g)	V_{BJH} (cm³/g)	V_{t-plot} (cm³/g)	Average pore width (nm)	Median Pore Size (nm)
G55-1	7.0648	0.0181	0.0003	10.0809	37.1455
G55-2	31.8860	0.0313	0.0026	4.0523	3.9583
G55-3	40.9633	0.0401	0.0034	4.0476	3.9385
A1-1	13.4741	0.0214	0.0012	6.0467	15.7122
A1-2	7.0968	0.0164	0.0006	8.9877	36.5020
A1-3	32.0093	0.0318	0.0049	3.4521	2.3615
A1-4	43.6434	0.0429	0.0036	4.0530	3.9630
A1-5	39.1090	0.0393	0.0042	3.6391	2.8217
CS1-1	12.9714	0.0227	0.0017	6.6517	18.2136
CS1-2	16.2535	0.0245	0.0018	5.7011	12.0847
CS1-3	28.4174	0.0373	0.0029	4.9206	6.7659
CS1-4	20.4252	0.0268	0.0021	4.9221	6.7808
CS1-5	25.1049	0.0309	0.0025	4.9290	6.8475
SW1-1	4.2921	0.0134	0.0005	12.3459	46.1250
SW1-2	22.1421	0.0308	0.0021	5.2434	10.4812
SW1-3	25.8305	0.0268	0.0039	3.6213	2.8385
SW1-4	28.5299	0.0271	0.0030	3.4026	2.2826

Pore size distributions reveal that the shale pore structure displays different patterns (Figure 3-5). The least organic-rich sample (SW1-1, TOC: 0.41%) shows almost no micro porosity. The rest of Mahantango samples exhibit similar characteristics, but with higher amount of micropores as TOC increases (Figure 3-5A). Marcellus samples demonstrate much more pore space

comparing to Mahantango, especially in the micropore section. Sample G55-2, G55-3, A1-3, A1-4, and A1-5 exhibit similar PSD, with decent amount of pores between 4 to 10 nm. These 5 samples also show the largest SSA. In the Marcellus Shale, most of the pore space are within 10 nm pore width, while in Mahantango Formation, the majority of the pores are larger than 10 nm. Low thermal maturity Marcellus samples SW1-3 and SW1-4 show limited mesopore compared with other organic rich samples (Figure 3-5).

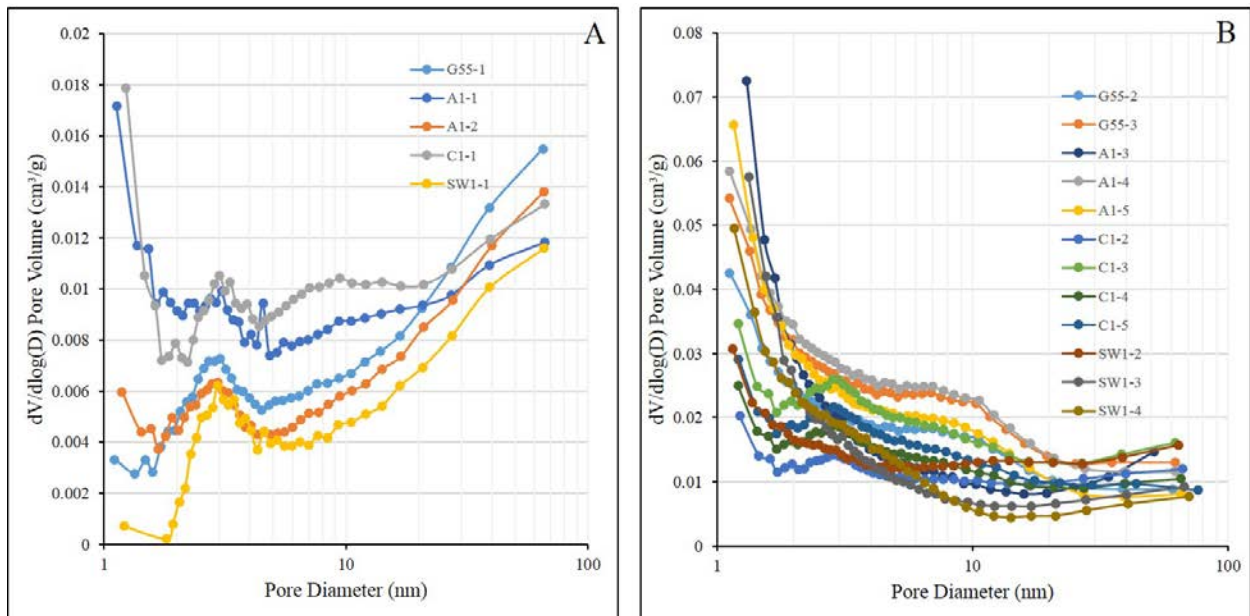


Figure 3-5. Pore size distribution of samples from Mahantango and Marcellus Formations, A: Mahantango, B: Marcellus.

4. Discussion

4.1 Relationship between pore structure parameters

Shale samples with smaller pores have larger specific surface area and pore volume. Table 3-4 illustrates a general negative relationship between specific surface area and pore size (average pore width, median pore size). Pore volume and pore size show the same negative correlation (Table 3-4). The porosity value in this research as determined by the GRI method shows a negative correlation between porosity and pore size (Figure 3-6). All samples show an increase in pore volume and surface area with decreasing pore size.

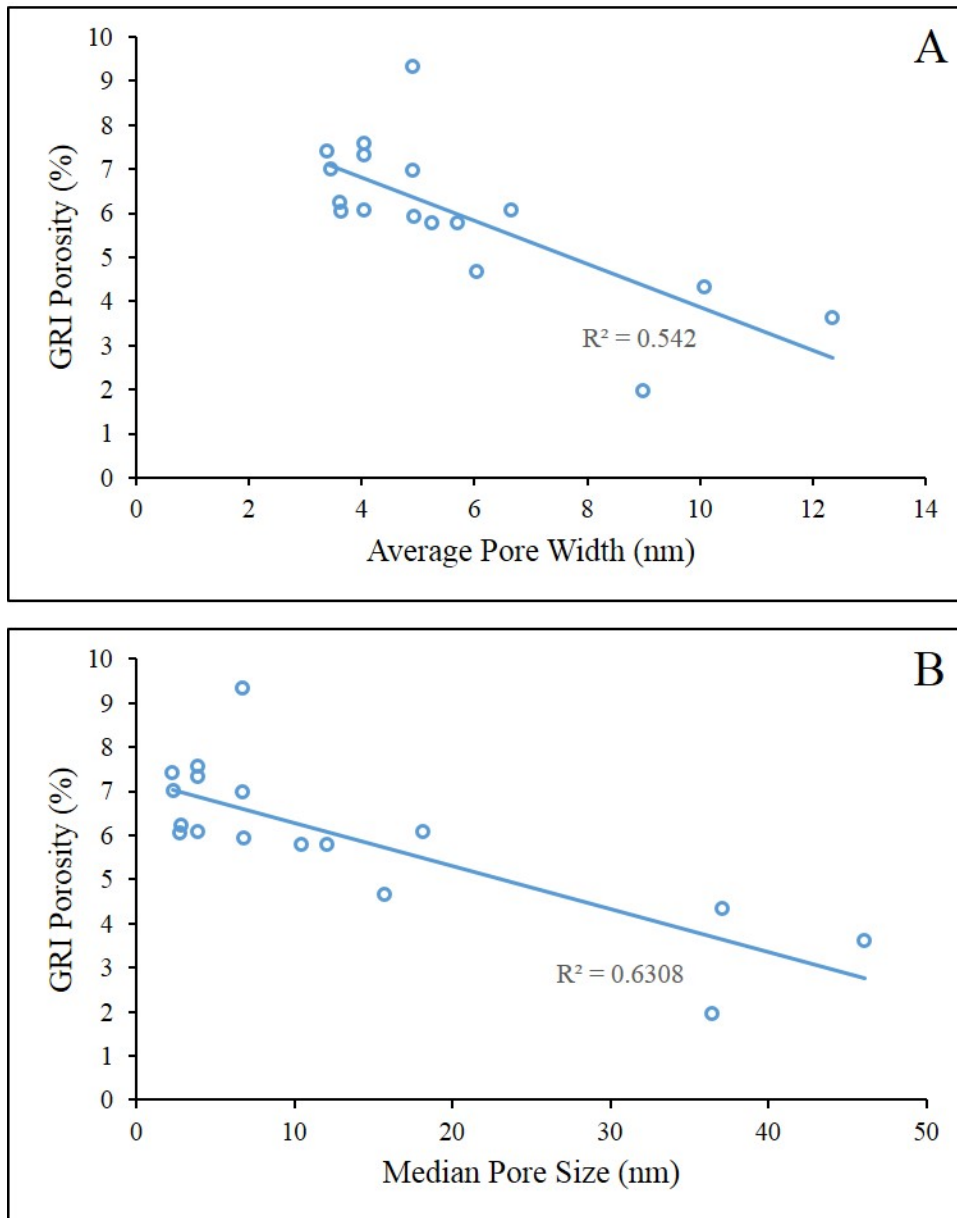


Figure 3-6. Relationships between total organic carbon (TOC) content and (A) average pore width, and (B) median pore size.

4.2 Relationships between pore structure and TOC

The influences of organic matter upon the pore structure are demonstrated in Figure 3-7. From Mahantango Formation to Marcellus Formation, there is a significant increase in storage

capacity, both in adsorption state (specific surface area), and free-gas state (pore volume). The least organic-rich sample SW1-1 (TOC 0.41%) shows the least specific surface area and pore volume, and the largest pore size (Table 3-4). In this sample with negligible organic matter, most of the pores are hosted by non-organic minerals. The increase in specific surface area and pore volume appears to be attributed to the increasing TOC, and the development of organic matter hosted pores (Chalmers et al., 2012; Loucks et al., 2012; Milliken et al., 2013). Overall, good correlations have been found between TOC and specific surface area and pore volume (Figure 3-7), and porosity (Figure 3-8B). The increase of TOC also is related to a decrease in pore size (Figure 3-8A). This argument agrees with previous research on porosity development in other shale units (Bustin et al., 2009; Chalmers et al., 2012; Clarkson et al., 2012; Loucks et al., 2012; Mosher et al., 2013; Tian et al., 2013; Yu et al., 2016). At the lower TOC side, all the samples show a similar range of specific surface area and pore volume. As TOC increases, samples from different wells react differently to the enrichment of TOC. Samples from well G55 and A1 show a better storage capacity than SW1 and CS1.

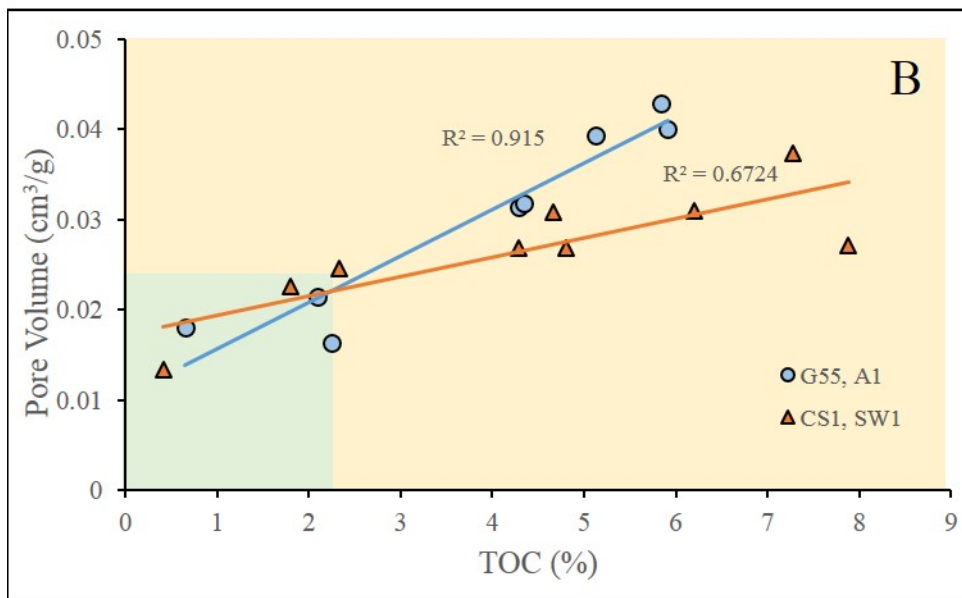
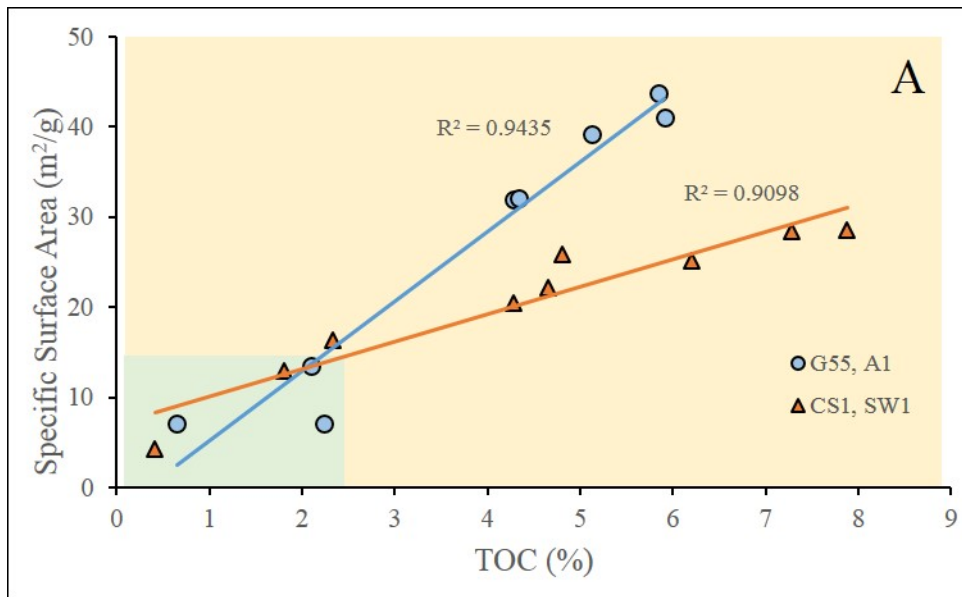


Figure 3-7. Relationship between specific surface area, pore volume, and TOC. Data points in green shadow are from Mahanantango Fm., while yellow shadow covers the Marcellus samples.

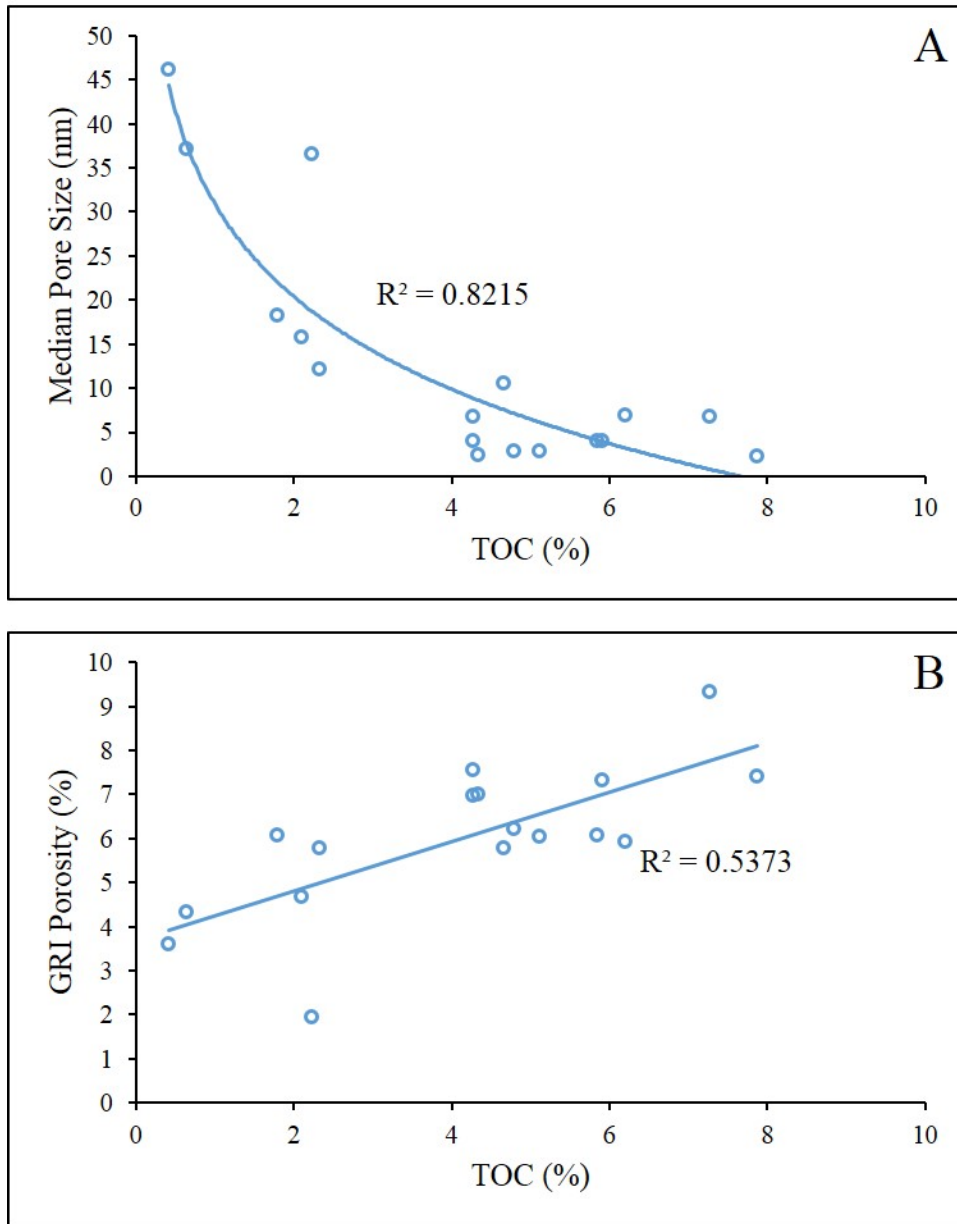


Figure 3-8. Relationship between TOC and (A) median pore size, and (B) GRI porosity.

4.3 Relationships between pore structure and minerals

In this research, no correlation was observed between carbonate or quartz content and specific surface area. Figure 3-9 shows a negative correlation between content of clay minerals and the storage capacity. Pure clay minerals have been found to have large specific surface area

(Saidian et al., 2016). For illite, the BET SSA is usually in the order of 100 m²/g, and the BET SSA of kaolinite and chlorite typically stays in the order of 10 m²/g (Saidian et al., 2015). However, on those clay rich samples (Table 3-2, Figure 3-3), the contribution to the SSA and pore volume is not observed. This phenomenon may be attributed to the accessibility of the pore space. This result agrees with Milliken et al. (2013)'s research (Milliken et al., 2013) that the Marcellus Shale is an *organic matter-hosted pore system*. Organic matter shows the most significant control on the storage capacity than minerals.

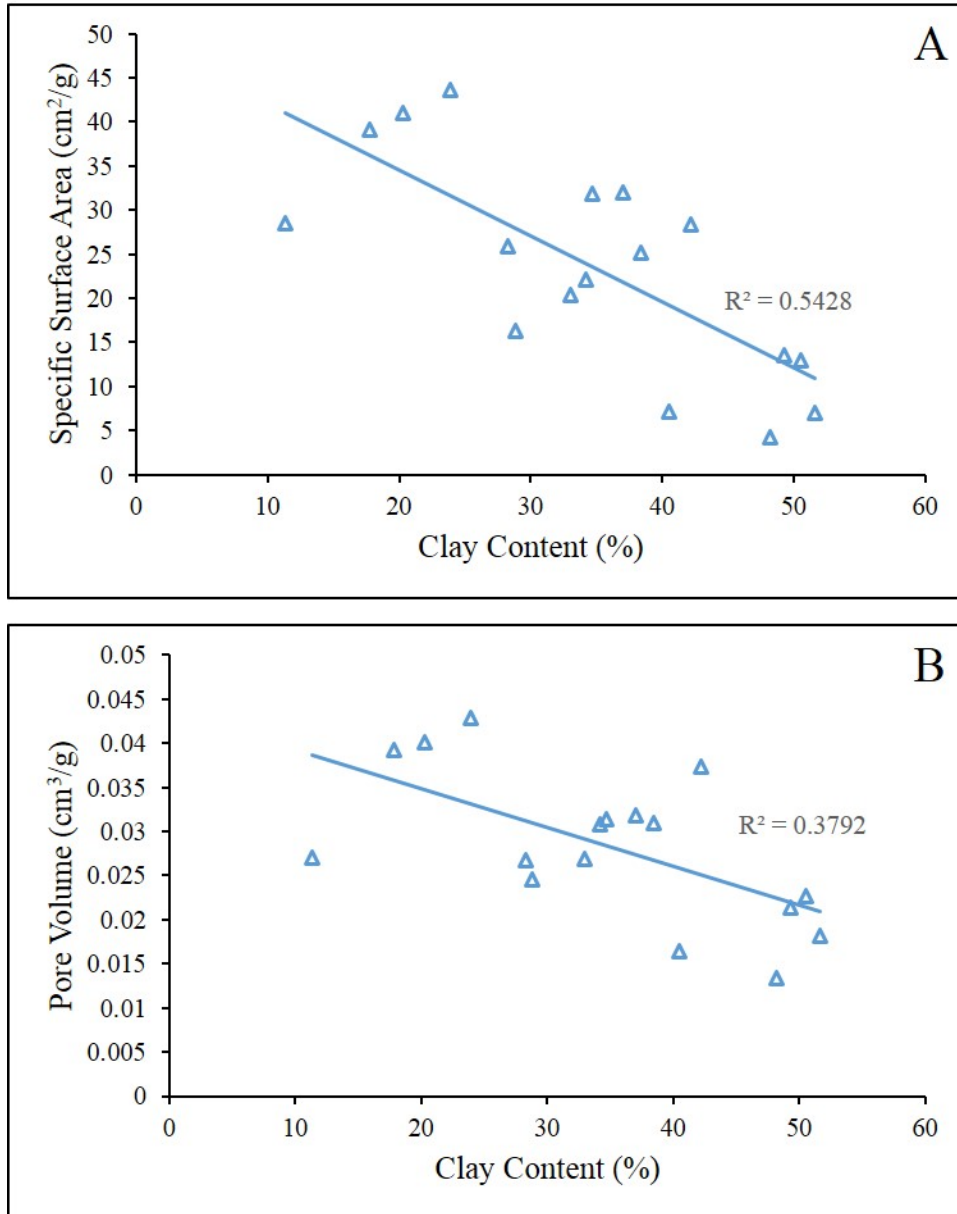


Figure 3-9. Relationships between clay content and (A) specific surface area, and (B) pore volume.

4.4 The relationship between thermal maturity and pore structure

Thermal maturity also plays a very important but complex role in evaluating the storage capacity of shales. Figure 3-10 shows the results of SSA involve with vitrinite reflectance. The

samples in this research cover a thermal maturity ranging from the late oil window (well SW1), to the dry gas window (G55, A1), ending in the post-mature zone (CS1). Under every single thermal maturity zone, we notice a significant strong positive correlation between TOC and SSA in both Mahantango and Marcellus samples. Given a similar TOC level, samples in the dry gas window shows the highest SSA, and samples from the post-mature zone shows the least. Our observation supports the ideas that porosity is altered during maturation, and organic matter is largely responsible for porosity changes because of the transformation of its kerogen and bitumen into hydrocarbons and other liquids. Also, the storage capacity can be reduced when it gets into the post mature zone.

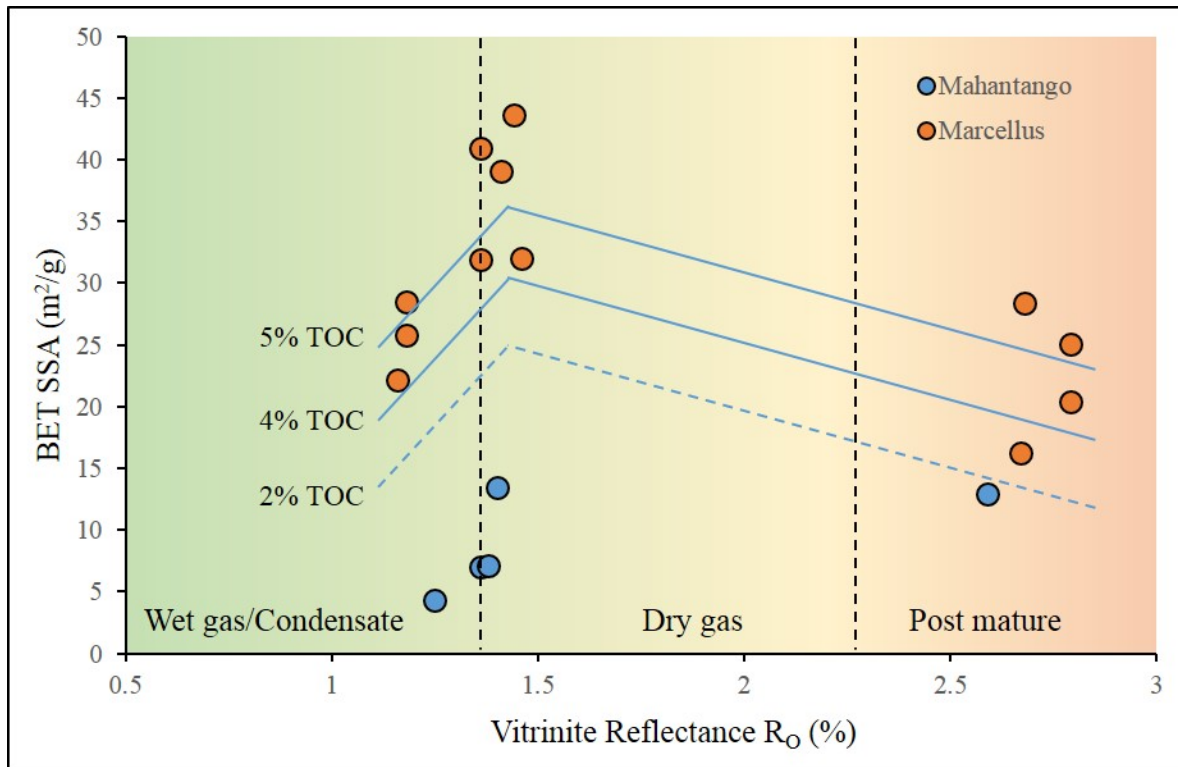


Figure 3-10. Relationship between thermal maturity (represented by vitrinite reflectance) and specific surface area.

Conclusions

The SSA, pore volume, and pore size were measured for four wells penetrating the Mahantango Formation and the Marcellus Shale from West Virginia and Pennsylvania. The thermal maturity of the tested samples covers a wide range in the hydrocarbon generation sequence from 1.16 to 2.79 % R_o . Also, samples have a wide range of TOC, clay content and type. The following conclusions based on the results in this study are drawn:

1. The presence of organic matter in shale strongly enhances the storage capacity by increasing the specific surface area and pore volume;
2. As TOC increases, average and median pore sizes decrease;
3. Carbonate and quartz do not show any correlation with porosity, specific surface area, and pore volume;
4. Organic matter has more significant influence on specific surface area and pore volume than clay content. A negative correlation is found between clay content and specific surface area and pore volume. We suspect the accessibility of the pore space within clay minerals has been blocked.
5. The development of organic matter pores is altered during thermal maturation. Shales in dry gas window show highest specific surface area and pore volume. Samples from post-matured zone show a reduced range of storage capacity under the same TOC level.

Reference Cited:

- Adesida, A. G., I. Y. Akkutlu, D. E. Resasco, and C. S. Rai, 2011, SPE 147397 Kerogen Pore Size Distribution of Barnett Shale using DFT Analysis and Monte Carlo Simulations: SPE Annual Technical Conference and Exhibition, p. 1–14, doi:10.2118/147397-MS.
- Ambrose, R. J., D. Energy, R. C. Hartman, and W. Labs, 2010, SPE 131772 New Pore-scale Considerations for Shale Gas in Place Calculations: doi:10.2118/131772-MS.
- Anovitz, L. M., and D. R. Cole, 2015, Characterization and Analysis of Porosity and Pore Structures: Reviews in Mineralogy and Geochemistry, v. 80, p. 61–164, doi:10.2138/rmg.2015.80.04.
- Bai, B., M. Elgmati, H. Zhang, and M. Wei, 2013, Rock characterization of Fayetteville shale gas plays: Fuel, v. 105, p. 645–652, doi:10.1016/j.fuel.2012.09.043.
- Barrett, E. P., L. G. Joyner, and P. P. Halenda, 1951, The determination of pore volume and area distributions in porous substances. I. computations from nitrogen isotherms: Journal of the American Chemical Society, v. 73, no. 1, p. 373–380, doi:10.1021/ja01145a126.
- Bennett, R. H., N. R. O. Brien, M. H. Hulbert, O. S. Directorate, N. Oceanographic, O. S. Directorate, and N. Oceanographic, 1991, Determinants of clay microfabric signatures- Processes and mechanisms, *in* Microstructure of fine-grained sediments: New York, Springer-Verlag, p. 5–32.
- Bernard, S., L. Brown, R. Wirth, A. Schreiber, H.-M. Schulz, B. Horsfield, A. C. Aplin, and E. J. Mathia, 2013, FIB-SEM and TEM Investigations of an Organic-rich Shale Maturation Series from the Lower Toarcian Posidonia Shale, Germany: Nanoscale Pore System and Fluid-rock Interactions: Electron microscopy of shale hydrocarbon reservoirs: AAPG Memoir 102, p. 53–66, doi:10.1306/13391705M1023583.

- Bohacs, K. M., Q. R. Passey, M. Rudnicki, W. L. Esch, and O. R. Lazar, 2013, The Spectrum of Fine-Grained Reservoirs from “Shale Gas” to “Shale Oil”/ Tight Liquids : Essential Attributes, Key Controls, Practical Characterization: IPTC 2013: International Petroleum Technology Conference, no. Figure 1, p. 1–16, doi:10.2523/16676-MS.
- Boyce, M., A. Yanni, and T. Carr, 2010, Depositional control of organic content in the Middle Devonian Marcellus interval of West Virginia and Western Pennsylvania: Critical Assessment of ..., p. 3–6.
- Brunauer, S., P. H. Emmett, and E. Teller, 1938, Adsorption of Gases in Multimolecular Layers: Journal of the American Chemical Society, v. 60, no. 1, p. 309–319, doi:citeulike-article-id:4074706\rdoi: 10.1021/ja01269a023.
- Bustin, R. M., A. M. M. Bustin, B. Columbia, X. Cui, and D. J. K. Ross, 2008, SPE 119892 Impact of Shale Properties on Pore Structure and Storage Characteristics.
- Bustin, R. M., a Bustin, D. Ross, G. Chalmers, V. Murthy, C. Laxmi, and X. Cui, 2009, Shale Gas Opportunities and Challenges *: Search and Discovery Articles, v. 40382.
- Carr, T. R. et al., 2016, The Marcellus Shale Energy and Environment Laboratory (MSEEL)*, in AAPG Eastern Section Meeting, Lexington, Kentucky.
- Chalmers, G. R. L., and R. Marc Bustin, 2007, On the effects of petrographic composition on coalbed methane sorption: International Journal of Coal Geology, v. 69, no. 4, p. 288–304, doi:10.1016/j.coal.2006.06.002.
- Chalmers, G. R. L., D. J. K. Ross, and R. M. Bustin, 2012, Geological controls on matrix permeability of Devonian Gas Shales in the Horn River and Liard basins, northeastern British Columbia, Canada: International Journal of Coal Geology, v. 103, p. 120–131, doi:10.1016/j.coal.2012.05.006.

- Chen, R., and S. Sharma, 2017, Linking the Acadian Orogeny with organic-rich black shale deposition: Evidence from the Marcellus Shale: *Marine and Petroleum Geology*, v. 79, p. 149–158, doi:10.1016/j.marpetgeo.2016.11.005.
- Chen, R., and S. Sharma, 2016, Role of alternating redox conditions in the formation of organic-rich interval in the Middle Devonian Marcellus Shale , Appalachian Basin , USA: *Palaeogeography, Palaeoclimatology, Palaeoecology*, v. 446, p. 85–97, doi:10.1016/j.palaeo.2016.01.016.
- Chen, R., S. Sharma, T. Bank, D. Soeder, and H. Eastman, 2015, Comparison of isotopic and geochemical characteristics of sediments from a gas- and liquids-prone wells in Marcellus Shale from Appalachian Basin, West Virginia: *Applied Geochemistry*, v. 60, p. 59–71, doi:10.1016/j.apgeochem.2015.01.001.
- Clarkson, C. R., J. M. Wood, S. E. Burgis, S. D. Aquino, and M. Freeman, 2012, Nanopore-structure analysis and permeability predictions for a tight gas siltstone reservoir by use of low-pressure adsorption and mercury-intrusion techniques: *SPE Reservoir Evaluation & Engineering*, v. 15, no. 6, p. 648–661, doi:10.2118/155537-PA.
- Crain, E. R., and D. Holgate, 2014, A 12-Step program to reduce uncertainty in kerogen-rich reservoirs: *Canadian Well Logging Society*, v. i, no. Spring, p. 10–16.
- Culligan, K. A., D. Wildenschild, B. S. B. Christensen, W. G. Gray, and M. L. Rivers, 2006, Pore-scale characteristics of multiphase flow in porous media : A comparison of air – water and oil – water experiments: *Advances in Water Resources*, v. 29, p. 227–238, doi:10.1016/j.advwatres.2005.03.021.
- Culligan, K. A., D. Wildenschild, B. S. B. Christensen, W. G. Gray, M. L. Rivers, and A. F. B. Tompson, 2004, Interfacial area measurements for unsaturated flow through a porous

- medium: *Water Resources Research*, v. 40, no. W12413, p. 1–12,
doi:10.1029/2004WR003278.
- Curtis, M. E., and R. J. Ambrose, 2011, Investigation of the relationship between organic porosity and thermal maturity in the Marcellus Shale, *in* SPE Conference: p. 4pp,
doi:10.2118/144370-ms.
- Curtis, M. E., C. H. Sondergeld, R. J. Ambrose, and C. S. Rai, 2012, Microstructural investigation of gas shales in two and three dimensions using nanometer-scale resolution imaging: *AAPG Bulletin*, v. 96, no. 4, p. 665–677, doi:10.1306/08151110188.
- Deirieh, A., 2016, *From Clay Slurries to Mudrocks : A Cryo-SEM Investigation of the Development of the Porosity and Microstructure*: Massachusetts Institute of Technology, 226 p.
- Desbois, G., J. L. Urai, and P. A. Kukla, 2009, Morphology of the pore space in claystones – evidence from BIB/FIB ion beam sectioning and cryo-SEM observations: *eEarth Discussions*, v. 4, no. 1, p. 1–19, doi:10.5194/eed-4-1-2009.
- Dilks, A., and S. C. Graham, 1985, Quantitative Mineralogical Characterization of Sandstones by Back-scattered Electron Image Analysis: *Journal of Sedimentary Petrology*, v. 55, no. 3, p. 347–355.
- Dong, T., and N. B. Harris, 2013, Pore Size Distribution and Morphology in the Horn River Shale, Middle and Upper Devonian, Northeastern British Columbia, Canada: *Electron microscopy of shale hydrocarbon reservoirs: AAPG Memoir 102*, p. 67–80,
doi:10.1306/13391706M1023584.
- Driskill, B., J. Walls, J. DeVito, and S. W. Sinclair, 2013, Applications of SEM Imaging to Reservoir Characterization in the Eagle Ford Shale, South Texas, U.S.A., *in* *Electron*

- microscopy of shale hydrocarbon reservoirs: AAPG Memoir 102: p. 115–136,
doi:10.1306/13391709M1023587.
- EIA, U. S., 2018, Annual Energy Outlook 2018 with projections to 2050 Table of contents:
Washington, DC, 74 p.
- Erdman, N., and N. Drenzek, 2013, Integrated Preparation and Imaging Techniques for the
Microstructural and Geochemical Characterization of Shale by Scanning Electron
Microscopy: Electron microscopy of shale hydrocarbon reservoirs: AAPG Memoir 102, p.
7–14, doi:10.1306/13391700M1023581.
- Espitalie, J., G. Deroo, and F. Marquis, 1985, La pyrolyse Rock-Eval et ses applications.
Deuxième partie.: Revue de l'Institut Français du Pétrole, v. 40, no. 6, p. 755–784,
doi:10.2516/ogst:1985045.
- Ettensohn, F. R., and T. R. Lierman, 2012, Large-scale Tectonic Controls on the Origin of
Paleozoic Dark-shale Source-rock Basins: Examples from the Appalachian Foreland Basin,
Eastern United States: AAPG Bulletin, v. 100, no. January 2012, p. 95–124,
doi:10.1306/13351549M1003529.
- Fishman, N. S., J. L. Ridgley, D. K. Higley, M. L. W. Tuttle, and D. L. Hall, 2012, Ancient
Microbial Gas in the Upper Cretaceous Milk River Formation, Alberta and Saskatchewan:
A Large Continuous Accumulation in Fine-grained Rocks Neil: Shale Reservoirs —Giant
Resources for the 21st Century: AAPG Memoir 97, v. 97, p. 258–289,
doi:10.1306/13321471M973493.
- Gallagher, N. C. J., and G. L. Wise, 1981, A Theoretical Analysis of the Properties of Median Fi
hers: IEEE Transactions on acoustic, speech, and signal processing, v. 29, no. 6, p. 1136–
1141.

- Giffin, S., R. Littke, J. Klaver, and J. L. Urai, 2013, Application of BIB-SEM technology to characterize macropore morphology in coal: *International Journal of Coal Geology*, v. 114, p. 85–95, doi:10.1016/j.coal.2013.02.009.
- Hemes, S., G. Desbois, J. L. Urai, M. De Craen, and M. Honty, 2013, Variations in the morphology of porosity in the Boom Clay Formation: Insights from 2D high resolution BIB-SEM imaging and Mercury injection Porosimetry: *Geologie en Mijnbouw/Netherlands Journal of Geosciences*, v. 92, no. 4, p. 275–300, doi:doi:10.1017/S0016774600000214.
- Hemes, S., G. Desbois, J. L. Urai, B. Schröppel, and J. O. Schwarz, 2015, Multi-scale characterization of porosity in Boom Clay (HADES-level, Mol, Belgium) using a combination of X-ray u-CT, 2D BIB-SEM and FIB-SEM tomography: *Microporous and Mesoporous Materials*, v. 208, p. 1–20, doi:10.1016/j.micromeso.2015.01.022.
- Houben, M. E., G. Desbois, and J. L. Urai, 2014, A comparative study of representative 2D microstructures in Shaly and Sandy facies of Opalinus Clay (Mont Terri, Switzerland) inferred from BIB-SEM and MIP methods: *Marine and Petroleum Geology*, v. 49, p. 143–161, doi:10.1016/j.marpetgeo.2013.10.009.
- Houben, M. E., G. Desbois, and J. L. Urai, 2013, Pore morphology and distribution in the Shaly facies of Opalinus Clay (Mont Terri, Switzerland): Insights from representative 2D BIB-SEM investigations on mm to nm scale: *Applied Clay Science*, v. 71, p. 82–97, doi:10.1016/j.clay.2012.11.006.
- Huang, J., T. Cavanaugh, and B. Nur, 2013, An Introduction to SEM Operational Principles and Geologic Applications for Shale Hydrocarbon Reservoirs: *Electron microscopy of shale hydrocarbon reservoirs: AAPG Memoir 102*, p. 1–6, doi:10.1306/13391699M1023580.
- Jarvie, D. M., R. J. Hill, T. E. Ruble, and R. M. Pollastro, 2007, *Unconventional shale-gas*

- systems: The Mississippian Barnett Shale of north-central Texas as one model for thermogenic shale-gas assessment: *AAPG Bulletin*, v. 91, no. 4, p. 475–499, doi:10.1306/12190606068.
- Katz, A. J., and A. H. Thompson, 1985, Fractal Sandstone Pores: Implications for Conductivity and Pore Formation: *Physical Review Letters*, v. 54, no. 12, p. 1325–1328.
- Kelly, S., H. El-sobky, C. Torres-verdín, and M. T. Balhoff, 2016, Advances in Water Resources Assessing the utility of FIB-SEM images for shale digital rock physics: *Advances in Water Resources*, v. 95, p. 302–316, doi:10.1016/j.advwatres.2015.06.010.
- Klaver, J., G. Desbois, R. Littke, and J. L. Urai, 2015, BIB-SEM characterization of pore space morphology and distribution in postmature to overmature samples from the Haynesville and Bossier Shales: *Marine and Petroleum Geology*, v. 59, p. 451–466, doi:10.1016/j.marpetgeo.2014.09.020.
- Klaver, J., G. Desbois, J. L. Urai, and R. Littke, 2012, BIB-SEM study of the pore space morphology in early mature Posidonia Shale from the Hils area, Germany: *International Journal of Coal Geology*, v. 103, p. 12–25, doi:10.1016/j.coal.2012.06.012.
- Ko, L. T., R. G. Loucks, K. L. Milliken, Q. Liang, T. Zhang, X. Sun, P. C. Hackley, S. C. Ruppel, and S. Peng, 2017, Controls on pore types and pore-size distribution in the Upper Triassic Yanchang Formation , Ordos Basin , China : Implications for pore-evolution models of lacustrine mudrocks: *Interpretation*, v. 5, no. 2, p. 127–148, doi:10.1190/INT-2016-0115.1.
- Kuila, U., and M. Prasad, 2013, Specific surface area and pore-size distribution in clays and shales: *Geophysical Prospecting*, v. 61, no. 2, p. 341–362, doi:10.1111/1365-2478.12028.
- Lash, G. G., and D. R. Blood, 2014, Organic matter accumulation, redox, and diagenetic history

- of the Marcellus Formation, southwestern Pennsylvania, Appalachian basin: *Marine and Petroleum Geology*, v. 57, no. November, p. 244–263,
doi:10.1016/j.marpetgeo.2014.06.001.
- Lash, G. G., and T. Engelder, 2011, Thickness trends and sequence stratigraphy of the Middle Devonian Marcellus Formation, Appalachian Basin: Implications for Acadian foreland basin evolution: *AAPG Bulletin*, v. 95, no. 1, p. 61–103, doi:10.1306/06301009150.
- Lazar, R., K. Bohacs, R. Klimentidis, M. Dumitrescu, and J. Ottmann, 2016, An SEM Study of Porosity in the Eagle Ford Shale of Texas—Pore Types and Porosity Distribution in a Depositional and Sequence-stratigraphic Context: *The Eagle Ford Shale: A renaissance in U.S. oil production: AAPG Memoir 110*, p. 167–186, doi:10.1306/13541961M1103589.
- Lazar, O. R., K. M. Bohacs, J. H. S. Macquaker, J. Schieber, and T. M. Demko, 2015, Capturing Key Attributes of Fine-Grained Sedimentary Rocks In Outcrops, Cores, and Thin Sections: Nomenclature and Description Guidelines: *Journal of Sedimentary Research*, v. 85, no. 3, p. 230–246.
- Loucks, R. G., R. M. Reed, S. C. Ruppel, and U. Hammes, 2012, Spectrum of pore types and networks in mudrocks and a descriptive classification for matrix-related mudrock pores: *AAPG Bulletin*, v. 96, no. 6, p. 1071–1098, doi:10.1306/08171111061.
- Loucks, R. G., R. M. Reed, S. C. Ruppel, and D. M. Jarvie, 2009, Morphology, Genesis, and Distribution of Nanometer-Scale Pores in Siliceous Mudstones of the Mississippian Barnett Shale: *Journal of Sedimentary Research*, v. 79, no. 12, p. 848–861,
doi:10.2110/jsr.2009.092.
- Luffel, D. L., and F. K. Guidry, 1992, New Core Analysis Methods for Measuring Reservoir Rock Properties of Devonian Shale, *in* SPE Annual Technical Conference and Exhibition:

p. 1184–1190, doi:10.2118/20571-PA.

Mastalerz, M., A. Schimmelmann, A. Drobniak, and Y. Chen, 2013, Porosity of Devonian and Mississippian New Albany Shale across a maturation gradient: Insights from organic petrology', gas adsorption, and mercury intrusion: AAPG Bulletin, v. 97, no. 10, p. 1621–1643, doi:10.130/04011312194.

Matthew, B. L., and T. R. Carr, 2009, Lithostratigraphy and Petrophysics of the Devonian Marcellus Interval in West Virginia and Southwestern Pennsylvania.

Milliken, K. L., and R. J. Day-Stirrat, 2013, Cementation in mudrocks: Brief review with examples from cratonic basin mudrocks: AAPG Memoir, v. 103, p. 133–150, doi:10.1306/13401729H5252.

Milliken, K. L., R. J. Day-Stirrat, P. K. Papazis, and C. Dohse, 2012, Carbonate Lithologies of the Mississippian Barnett Shale, Fort Worth Basin, Texas: Shale reservoirs—Giant resources for the 21st century, p. 290–321, doi:10.1306/13321473M97252.

Milliken, K. L., W. L. Esch, R. M. Reed, and T. Zhang, 2012, Grain assemblages and strong diagenetic overprinting in siliceous mudrocks, Barnett Shale (Mississippian), Fort Worth Basin, Texas: AAPG Bulletin, v. 96, no. 8, p. 1553–1578, doi:10.1306/12011111129.

Milliken, K. L., L. T. Ko, M. Pommer, and K. M. Marsaglia, 2014, Sem Petrography of Eastern Mediterranean Sapropels: Analogue Data For Assessing Organic Matter In Oil and Gas Shales: Journal of Sedimentary Research, v. 84, no. 11, p. 961–974, doi:10.2110/jsr.2014.75.

Milliken, K. L., and T. Olson, 2016, Amorphous and Crystalline Solids as Artifacts in SEM Images: p. 1–8, doi:10.1306/13592013M112252.

Milliken, K. L., and R. M. Reed, 2010, Multiple causes of diagenetic fabric anisotropy in weakly

- consolidated mud , Nankai accretionary prism , IODP Expedition 316: *Journal of Structural Geology*, v. 32, no. 12, p. 1887–1898, doi:10.1016/j.jsg.2010.03.008.
- Milliken, K. L., M. Rudnicki, D. N. Awwiller, and T. Zhang, 2013, Organic matter-hosted pore system, Marcellus Formation (Devonian), Pennsylvania: *AAPG Bulletin*, v. 97, no. 2, p. 177–200, doi:10.1306/07231212O48.
- Mosher, K., J. He, Y. Liu, E. Rupp, and J. Wilcox, 2013, Molecular simulation of methane adsorption in micro- and mesoporous carbons with applications to coal and gas shale systems: *International Journal of Coal Geology*, v. 109–110, p. 36–44, doi:10.1016/j.coal.2013.01.001.
- Nole, M., H. Daigle, K. L. Milliken, and M. Prodanovic, 2016, A method for estimating microporosity of fine-grained sediments and sedimentary rocks via scanning electron microscope image analysis: *Sedimentology*, v. 63, no. 6, p. 1507–1521, doi:10.1111/sed.12271.
- Olson, E., 2012, The Importance of Sample Preparation when Measuring Specific Surface Area: *Journal of GXP Compliance*, v. 16, no. 3, p. 52~62.
- Otsu, N., 1979, A Threshold Selection Method from Gray-Level Histograms: *IEEE Transactions on Systems, Man, and Cybernetics*, v. 19, no. 1, p. 62–66, doi:10.1109/TSMC.1979.4310076.
- Passey, Q. R., K. M. Bohacs, W. L. Esch, R. E. Klimentidis, and S. K. Sinha, 2012, My source rock is now my reservoir - geologic and petrophysical characterization of shale-gas reservoirs: *Search and Discovery*, v. 80231, no. 80231, p. 47pp.
- Phansalkart, N., S. More, A. Sabale, and M. Joshi, 2011, Adaptive Local Thresholding for Detection of Nuclei in Diversity Stained Cytology Images, *in International Conference on*

Communications and Signal Processing: p. 218–220.

Pommer, M., and K. Milliken, 2015, Pore types and pore-size distributions across thermal maturity, Eagle Ford Formation, southern Texas: AAPG Bulletin, v. 99, no. 9, p. 1713–1744, doi:10.1306/03051514151.

Reed, R. M., R. G. Loucks, and S. C. Ruppel, 2014, Comment on “ Formation of nanoporous pyrobitumen residues during maturation of the Barnett Shale (Fort Worth Basin) ” by Bernard et al . (2012): International Journal of Coal Geology, v. 127, p. 111–113, doi:10.1016/j.coal.2013.11.012.

Ross, D. J. K., and R. M. Bustin, 2008a, Characterizing the shale gas resource potential of Devonian-Mississippian strata in the Western Canada sedimentary basin: Application of an integrated formation evaluation: AAPG Bulletin, v. 92, no. 1, p. 87–125, doi:10.1306/09040707048.

Ross, D. J. K., and R. M. Bustin, 2008b, Characterizing the shale gas resource potential of Devonian-Mississippian strata in the Western Canada sedimentary basin: Application of an integrated formation evaluation: AAPG Bulletin, v. 92, no. 1, p. 87–125, doi:10.1306/09040707048.

Ross, D. J. K., and R. M. Bustin, 2009, The importance of shale composition and pore structure upon gas storage potential of shale gas reservoirs: Marine and Petroleum Geology, v. 26, no. 6, p. 916–927, doi:10.1016/j.marpetgeo.2008.06.004.

Ross, D. J. K., and R. M. Bustin, 2009, The importance of shale composition and pore structure upon gas storage potential of shale gas reservoirs: Marine and Petroleum Geology, v. 26, no. 6, p. 916–927, doi:10.1016/j.marpetgeo.2008.06.004.

Ross, D. J. K., and R. Marc Bustin, 2007, Impact of mass balance calculations on adsorption

capacities in microporous shale gas reservoirs: *Fuel*, v. 86, no. 17–18, p. 2696–2706,
doi:10.1016/j.fuel.2007.02.036.

Sageman, B. B., A. E. Murphy, J. P. Werne, C. A. Ver Straeten, D. J. Hollander, and T. W. Lyons, 2003, A tale of shales: The relative roles of production, decomposition, and dilution in the accumulation of organic-rich strata, Middle-Upper Devonian, Appalachian basin: *Chemical Geology*, v. 195, no. 1–4, p. 229–273, doi:10.1016/S0009-2541(02)00397-2.

Saidian, M., L. J. Godinez, and M. Prasad, 2016, Effect of clay and organic matter on nitrogen adsorption specific surface area and cation exchange capacity in shales (mudrocks): *Journal of Natural Gas Science and Engineering*, v. 33, p. 1095–1106,
doi:10.1016/j.jngse.2016.05.064.

Saidian, M., L. J. Godinez, and M. Prasad, 2015, Effect of Clay and Organic Matter on Nitrogen Adsorption Specific Surface Area and Cation Exchange Capacity in Shales (Mudrocks): *Annual Logging Symposium*, v. 56, p. 1–16.

Sauvola, J., and M. Pietikainen, 2000, Adaptive document image binarization: *Pattern recognition*, v. 33, p. 225–236.

Schieber, J., 2010, Common Themes in the Formation and Preservation of Intrinsic Porosity in Shales and Mudstones - Illustrated with Examples Across the Phanerozoic: *SPE Unconventional Gas Conference*, p. 10, doi:10.2118/132370-MS.

Schieber, J., 2013, SEM Observations on Ion-milled Samples of Devonian Black Shales from Indiana and New York: The Petrographic Context of Multiple Pore Types: *Electron microscopy of shale hydrocarbon reservoirs: AAPG Memoir 102*, no. April 2010, p. 153–172, doi:10.1306/13391711M1023589.

Schindelin, J. et al., 2012, Fiji: an open source platform for biological image analysis.: *Nature*

- Methods, v. 9, no. 7, p. 676–682, doi:10.1038/nmeth.2019.Fiji.
- Schindelin, J., C. T. Rueden, M. C. Hiner, and K. W. Eliceiri, 2015, The ImageJ ecosystem: An open platform for biomedical image analysis: *Molecular Reproduction and Development*, v. 82, no. 7–8, p. 518–529, doi:10.1002/mrd.22489.
- Schneider, J., P. B. Flemings, R. J. Day-Stirrat, and J. T. Germaine, 2011, Insights into pore-scale controls on mudstone permeability through resedimentation experiments: *Geology*, v. 39, no. 11, p. 1011–1014, doi:10.1130/G32475.1.
- Schneider, C. a, W. S. Rasband, and K. W. Eliceiri, 2012, NIH Image to ImageJ: 25 years of image analysis: *Nature Methods*, v. 9, no. 7, p. 671–675, doi:10.1038/nmeth.2089.
- Sezgin, M., and B. Sankur, 2004, Survey over image thresholding techniques and quantitative performance evaluation: *Journal of Electronic Imaging*, v. 13, no. 1, p. 146–168, doi:10.1117/1.1631316.
- Sing, K., 2001, The use of nitrogen adsorption for the characterisation of porous materials: *Colloids and Surfaces A: Physicochemical and Engineering Aspects*, v. 187–188, p. 3–9, doi:10.1016/S0927-7757(01)00612-4.
- Sing, K. S. W., D. H. Everett, R. a. W. Haul, L. Moscou, R. a. Pierotti, J. Rouquérol, and T. Siemieniewska, 1982, Reporting Physisorption Data for Gas / Solid Systems with Special Reference to the Determination of Surface Area and Porosity: *Pure and Applied Chemistry*, v. 57, no. 4, p. 603–619, doi:10.1351/pac198557040603.
- Sing, K. S. W., and R. T. Williams, 2004, Physisorption hysteresis loops and the characterization of nanoporous materials: *Adsorption Science and Technology*, v. 22, no. December 2015, p. 773–782, doi:10.1260/0263617053499032.
- Slatt, R. M., and N. R. O'Brien, 2013, *Microfabrics Related to Porosity Development*,

- Sedimentary and Diagenetic Processes, and Composition of Unconventional Resource Shale Reservoirs as Determined by Conventional Scanning Electron Microscopy: Electron microscopy of shale hydrocarbon reservoirs: AAPG Memoir 102, p. 37–44, doi:10.1306/13391703M102441.
- Slatt, R. M., and N. R. O'Brien, 2011, Pore types in the Barnett and Woodford gas shales: Contribution to understanding gas storage and migration pathways in fine-grained rocks: AAPG Bulletin, v. 95, no. 12, p. 2017–2030, doi:10.1306/03301110145.
- Soeder, D. J., 2017, The Development of Natural Gas from the Marcellus Shale: Boulder, Colorado, The Geological Society of America, 143 p.
- Sondergeld, C. H., R. J. Ambrose, C. S. Rai, and J. Moncrieff, 2010, Micro-structural studies of gas shales: Society of Petroleum Engineers Unconventional Gas Conference, SPE Paper 131771, p. 17, doi:10.2118/131771-MS.
- Song, L., T. Paronish, V. Agrawal, B. Hupp, and S. Sharma, 2017, Depositional Environment and Impact on Pore Structure and Gas Storage Potential of Middle Devonian Organic Rich Shale, Northeastern West Virginia, Appalachian Basin, in Unconventional Resources Technology Conference (URTeC:2667397): doi:10.15530/urtec-2017-2667397.
- Strapoć, D., M. Mastalerz, A. Schimmelmann, A. Drobniak, and N. R. Hasenmueller, 2010, Geochemical constraints on the origin and volume of gas in the New Albany Shale (Devonian-Mississippian), eastern Illinois Basin: AAPG Bulletin, v. 94, no. 11, p. 1713–1740, doi:10.1306/06301009197.
- Thommes, M., K. Kaneko, A. V. Neimark, J. P. Olivier, F. Rodriguez-Reinoso, J. Rouquerol, and K. S. W. Sing, 2015, Physisorption of gases, with special reference to the evaluation of surface area and pore size distribution (IUPAC Technical Report): Pure and Applied

- Chemistry, v. 87, no. 9–10, p. 1051–1069, doi:10.1515/pac-2014-1117.
- Tian, H., L. Pan, X. Xiao, R. W. T. Wilkins, Z. Meng, and B. Huang, 2013, A preliminary study on the pore characterization of Lower Silurian black shales in the Chuandong Thrust Fold Belt, southwestern China using low pressure N₂ adsorption and FE-SEM methods: *Marine and Petroleum Geology*, v. 48, p. 8–19, doi:10.1016/j.marpetgeo.2013.07.008.
- Velde, B., 1996, Compaction trends of clay-rich deep sea sediments: *Marine Geology*, v. 133, p. 193–201.
- Walls, J. D., and E. Diaz, 2011, Relationship of shale porosity- permeability trends to pore type and organic content: *Petrophysics in Tight Oil Workshop*.
- Wang, G., and T. R. Carr, 2013, Organic-rich marcellus shale lithofacies modeling and distribution pattern analysis in the appalachian basin: *AAPG Bulletin*, v. 97, no. 12, p. 2173–2205, doi:10.1306/05141312135.
- Wang, G., Y. Ju, Z. Yan, and Q. Li, 2015, Pore structure characteristics of coal-bearing shale using fluid invasion methods: A case study in the Huainan-Huaibei Coalfield in China: *Marine and Petroleum Geology*, v. 62, p. 1–13, doi:10.1016/j.marpetgeo.2015.01.001.
- Wildenschild, D., and A. P. Sheppard, 2013, X-ray imaging and analysis techniques for quantifying pore-scale structure and processes in subsurface porous medium systems: *Advances in Water Resources*, v. 51, p. 217–246, doi:10.1016/j.advwatres.2012.07.018.
- Yu, W., K. Sepehrnoori, and T. W. Patzek, 2016, Modeling Gas Adsorption in Marcellus Shale With Langmuir and BET Isotherms.: *SPE Journal*, v. 21, no. 2, p. 589–600, doi:10.2118/170801-PA.
- Zagorski, W. a., G. R. Wrightstone, and D. C. Bowman, 2012, *The Appalachian Basin Marcellus Gas Play: Its History of Development, Geologic Controls on Production, and Future*

Potential as a World-class Reservoir, *in* AAPG Memoir 97: Shale Reservoirs-Giant Resources for the 21st Century: p. 172–200, doi:10.1306/13321465M973491.

Zhang, T., G. S. Ellis, S. C. Ruppel, K. Milliken, and R. Yang, 2012, Organic Geochemistry Effect of organic-matter type and thermal maturity on methane adsorption in shale-gas systems: *Organic Geochemistry*, v. 47, p. 120–131, doi:10.1016/j.orggeochem.2012.03.012.

Zhang, S., R. E. Klimentidis, and P. Barthelemy, 2011, Porosity and permeability analysis on nanoscale FIB-SEM 3D imaging of shale rock, *in* International Symposium of the Society of Core Analysis: p. 1–12.

Chapter IV

The Pore Structural Evolution of Mudrock: A Case Study of the Mahantango and Marcellus Shales, Appalachian Basin

Liaosha Song, Timothy R. Carr

Department of Geology and Geography, West Virginia University, Morgantown, WV

Email: liaoshasong@gmail.com

Abstract

The generation and primary migration of hydrocarbons in organic-rich shale leaves void space in organic matter, which is the porosity associated with organic matter commonly observed under scanning electron microscopy (SEM). In this study, Devonian black shale core samples were collected from three wells penetrating the organic-lean shale of the Mahantango Formation and the organic-rich Marcellus Shale in Pennsylvania and West Virginia. Pyrolysis, ion milled SEM and low-pressure nitrogen adsorption analysis were conducted to investigate the organic richness and the properties of the pore system (including porosity, pore volume, specific surface area, and pore size distribution). The black shale samples have total organic carbon (TOC) values from 0.65% to 8.90%. Vitrinite reflectance (R_o) values in the range of 1.36% to 2.89% represent a maturity spectrum covering the wet-gas to post-mature zones.

In general, the pore system is composed of organic matter-hosted pores and mineral-hosted pores. However, the dominant pore types and pore sizes vary stratigraphically across lithology and abundance of organic matter. All the organic matter observed in this study shows an amorphous occurrence. Pore space between mineral grains (both silt-size and clay-size) can be filled by organic matter, which contains secondary porosity generated by thermal cracking of kerogen. Mineral-hosted pores are concentrated in organic-lean samples in which secondary organic matter could not fill most of the primary pore space. The destruction of primary mineral-hosted pores and the generation of secondary organic matter-hosted pores were observed.

The BET specific surface area ranges from 4.10 m²/g to 47.58 m²/g and the micropore (pore width < 2nm) surface area estimated by the t-plot method ranges from 0 to 25.422 m²/g. TOC values show positive correlations with the porosity, specific surface area, and micropore volume and surface area. Increasing thermal maturity correlates with a significant decrease of

pore volume and surface area, primarily through diminishing or vanishing of micropores. The richness, depositional environment, and thermal maturity of organic matter in organic-rich Devonian shale can be effective parameters for evaluation of reservoir quality and upscaling the appraisal.

Keywords: porosity, pore size distribution, Marcellus Shale, SEM

Introduction

The pore systems and fluid flow networks in mudrock reservoirs composed of nanometer- to micrometer-scale connected pores and fractures, which provides the natural permeability pathways for the hydrocarbon flow (Javadpour, 2009; Curtis et al., 2010; Loucks et al., 2012; Bohacs et al., 2013). The pore systems accounting for both storing and releasing hydrocarbons have a critical impact on the producibility of shale reservoirs (Mastalerz et al., 2013). The integration of ion milling with SEM allows scientists to directly view pores hosted by organic matter (OM) and minerals in organic-rich mudstone (Davies et al., 1991; Desbois et al., 2009; Diaz et al., 2010; Loucks et al., 2009, 2012; Curtis et al., 2010; Chalmers et al., 2012; Milner et al., 2010; Passey et al., 2010; Schieber, 2010, 2013; Lu et al., 2011; Slatt and O'Neal, 2011;). Heterogeneity in the pore systems and the porosity evolution has been studied extensively and related to the burial history and the grain assemblages (e.g. Loucks et al., 2009, 2012, Milliken et al., 2013, 2014; Ko et al., 2017).

Most of the primary porosity between and within grains at deposition is destroyed because of compaction, cementation, and infill of primary porosity by ductile secondary OM, especially within organic-rich mudrocks (Velde, 1996; Desbois et al., 2009; Milliken and Reed, 2010; Kitty

L. Milliken et al., 2012; Loucks et al., 2012; Milliken et al., 2014; Pommer and Milliken, 2015). Primary pores are mainly hosted by minerals, and primary pores hosted by kerogen and other OM are only in trace amounts (Loucks et al., 2009; Fishman et al., 2012; Milliken et al., 2014; Reed et al., 2014; Pommer and Milliken, 2015). The preservation of primary pores largely relies on rigid grains that shelter pores from compaction (Desbois et al., 2009; Milliken and Reed, 2010; Schneider et al., 2011; Schieber, 2013; Milliken et al., 2014).

For petrographic observation, Schieber (2013) used the term amorphous organic matter to describe the OM that is intimately intermingled with minerals (clay and silt size), and is squeezed in the interstitial spaces between mineral grains, and lacks any characteristic morphology, as oppose to structured organic matter (such as Tasmanites). Milliken et al. (2014) suggests using the term “detrital OM” to describe particulate OM detritus present at the time of deposition. Also, the term “secondary OM” is used to describe pore-filling OM generated as a product of burial diagenesis, which is the bituminous material released by kerogen maturation. In this research, all the OM observed is categorized as secondary OM.

OM-hosted pores are observed in samples with thermal maturities generally greater than $R_o \sim 0.6\%$, the onset of peak oil generation, and have been described extensively as a component of mudrock reservoirs (Loucks et al., 2009; Ambrose et al., 2010; Curtis et al., 2012; Passey et al., 2012). Milliken et al. (2013) argue that in the Marcellus Shale, from the wet gas window ($R_o \sim 1.0\%$) to the dry gas window ($R_o \sim 2.1\%$), the abundance of OM is the major factor that influences the size and volume of OM-hosted pores. Thermal maturity, on the other hand, does not influence the pore system significantly. Former studies have reported that heterogeneity of OM types or maceral types influences the development of OM-hosted pores (Loucks et al., 2012; Driskill et al., 2013; Milliken and Day-Stirrat, 2013).

Quantitative characterization of different pore-structure attributes (e.g. porosity, pore-size distribution, specific surface area, and so forth) is crucial in modeling geophysical, petrophysical and fluid-flow behavior of porous media. Generally, porosity is the most common parameter for pore-structure and reservoir properties. However, porosity does not provide specific information on the geometric details of the pore structure. Pore-size distribution (PSD) of a porous media, on the other hand, quantifies the relative pore volumes associated with different pore sizes, which is also linked to elastic moduli and permeability of porous medium (Kuila and Prasad, 2013).

Low-pressure nitrogen adsorption (also refer to as BET test) is widely used to investigate the pore-size distribution of a wide variety of porous materials, and it is useful for characterizing mesopores (pore diameters between 2 and 50nm) and macropores (pore diameters >50nm) (Chalmers and Marc Bustin, 2007; Ross and Bustin, 2008b; Bustin et al., 2009; Strapoć et al., 2010; Chalmers et al., 2012; Clarkson et al., 2012; Kuila and Prasad, 2013; Mastalerz et al., 2013; Wang et al., 2015; Saidian et al., 2016).

This study characterizes pore system of mudrocks using two-dimensional SEM and BET test, and integrates this data with organic richness, thermal maturity, and lithology to evaluate the mineral- and OM-hosted pores. In addition, results are upscaled using well log data to develop a new technique for mapping pore-system characteristics in organic-rich mudrock across the Appalachian Basin. Core samples come from three wells with a wide spectrum of thermal maturity (R_o from 1.36% to 2.89%). The focus of this study is to gain insight into controls on porosity, pore types, and pore-size distribution across a range of organic richness, thermal maturity, and lithology, results of which will be upgraded to well logs.

Geologic Setting

The Marcellus Shale spans 95,000 square miles (246,000km²) across six states in northeastern U.S., which makes it the most extensive shale-gas play in North America (Carr et al., 2011). The Marcellus Shale is located in the lower portion of Hamilton Group, middle Devonian, and it is overlain by Tully Limestone and Mahantango Formation. The Cherry Valley Limestone Member divided the Marcellus into an upper shale (Oatka Creek Member) and lower shale (Union Springs Member). The Marcellus Shale is a distal marine mudstone within a westward-prograding foreland succession deposited in the Appalachian basin, which has been interpreted as a periodically deepening basin tied to tectonics and climate during the Acadian orogeny (Matthew and Carr, 2009; Boyce et al., 2010; Lash and Engelder, 2011; Ettensohn and Lierman, 2012; Zagorski et al., 2012; Milliken and Day-Stirrat, 2013; Wang and Carr, 2013; Carr et al., 2016; Song et al., 2017).

Core-samples and well log data from 3 wells were used in this study. Well CS1 is located in Clearfield County, Pennsylvania; Well A1 is located in Taylor County, West Virginia; Well G55 is located in Harrison County, West Virginia (Figure 4-1). Core samples used in this study come from lower portion of Mahantango Formation and the entire Marcellus Shale, which is the most organic-rich interval. Total organic carbon (TOC) of the three wells were computed based on bulk density and Schmoker Method (Schmoker, 1981), and calibrated with TOC data obtained from pyrolysis of core samples.

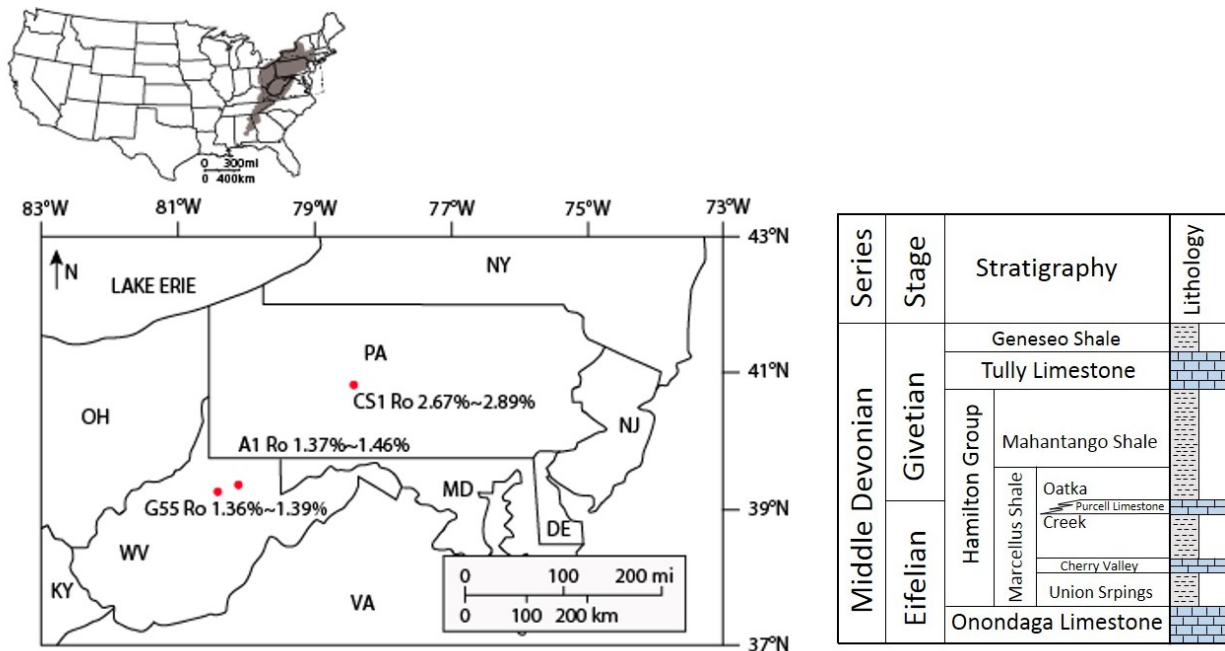


Figure 4-1. Locations and thermal maturity (as of vitrinite reflectance, Ro) of the three study wells, and the stratigraphic column of Middle Devonian in study area.

Methods

Sampling

Thirty-two core plugs were obtained from three wells in West Virginia and Pennsylvania penetrating Mahantango and Marcellus formations, including twenty-one samples from dry gas zone (Well A1 and G55; Ro 1.36%~1.41%), and eleven samples from post mature zone (Well CS1; Ro 2.67% ~2.89%). Total organic carbon (TOC) of the selected sample ranges from 0.08% to 6.83% (results in weight percent). Samples range in depth from 7015.00 ft. to 7778.15 ft. (2166 to 2349 m).

Table 4-1. Sample locations, Formations, and total organic carbon (TOC).

Well #	Depth (ft)	Formation	TOC (%)
G55	7078.1	Mahantango	3.72
G55	7084.1	Mahantango	3.19
G55	7113.5	Mahantango	0.17
G55	7122.4	Mahantango	0.21
G55	7128.75	Marcellus	4.05
G55	7135.3	Marcellus	3.33
G55	7141.25	Marcellus	2.31
G55	7162.45	Marcellus	4.53
G55	7201.1	Marcellus	6.22
G55	7217.4	Marcellus	6.77
A1	7547.3	Mahantango	1.43
A1	7591.4	Mahantango	0.08
A1	7620.1	Mahantango	0.27
A1	7677.65	Marcellus	2.68
A1	7688.5	Marcellus	3.02
A1	7702.65	Marcellus	2.64
A1	7720.65	Marcellus	5.66
A1	7729.5	Marcellus	6.83
A1	7740.45	Marcellus	4.81
A1	7753.3	Marcellus	4.13
A1	7778.15	Marcellus	2.15
CS1	7015	Mahanganto	1.62
CS1	7036	Mahanganto	1.96
CS1	7058.45	Marcellus	2.15
CS1	7069.25	Marcellus	2.71
CS1	7082.4	Marcellus	2.96
CS1	7092.92	Marcellus	3.1
CS1	7114.5	Marcellus	3.07
CS1	7124.75	Marcellus	2.81
CS1	7133.75	Marcellus	2.83
CS1	7136.85	Marcellus	2.87
CS1	7148.7	Marcellus	3.28

SEM

For this study, the core samples were ion-polished at Ingrain's Digital Rock Physics lab with Gatan Ilion+ Argon Ion polishing system. No conductive coatings were applied to the milled surfaces. An area approximately 1 millimeter by 500 micrometers is polished. A 2D SEM overview image is taken with a field of view of approximately 750 micrometers (Figure 4-2). The red rectangle within the overview indicates the smaller field of view for the 2D SEM. Approximately 10 locations per sample were imaged with Carl Zeiss SEM systems at a low-beam energy of 1 keV. Both backscatter electron (BSE) and secondary electron (SE2) detectors are used to capture images. Images from Well A1 and G55 were taken at resolution of approximately 15 nm per pixel, while images from Well CS1 were taken at resolution of 10 nm per pixel. All samples were viewed perpendicular to bedding (Figure 4-2C). SE2 SEM images are used in this study, since SE2 electrons include both compositional and topographical information (Huang et al., 2013). SEM images were processed with ImageJ and Fiji (Schindelin et al., 2012, 2015; Schneider et al., 2012). A median filter was applied before quantification to reduce the noise on the images (Gallagher and Wise, 1981; Culligan et al., 2004, 2006; Kelly et al., 2016; Nole et al., 2016).

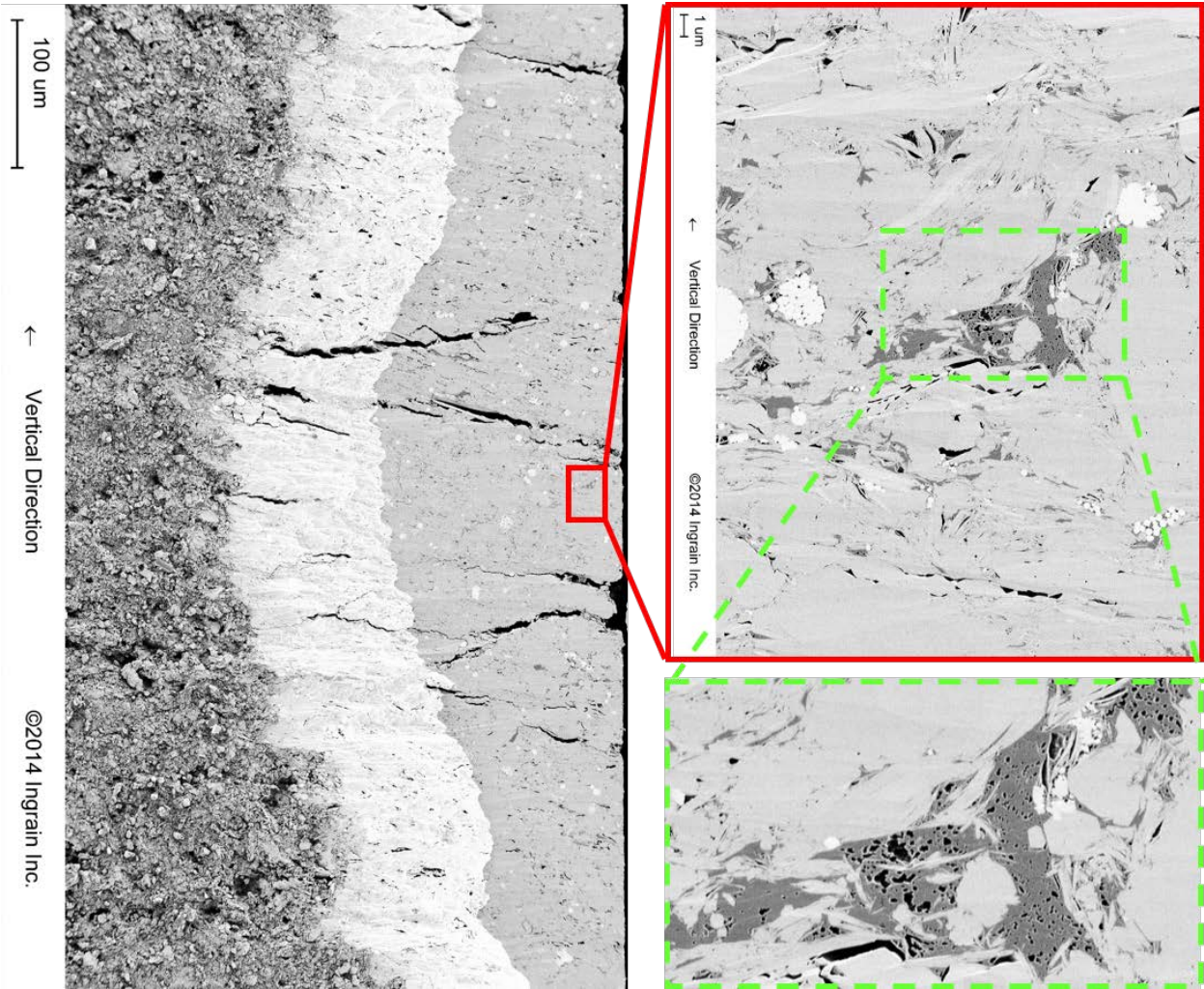


Figure 4-2. Imaging workflow (sample from well CS1, 7136.85 ft., %R_o=2.79).

Table 4-2. Results of TOC measurements and vitrinite reflectance (R_o).

Well ID	Depth(ft)	TOC(wt. %)	R _o (%)
CS1	7019	1.80	2.59
CS1	7070	2.67	2.67
CS1	7099.5	7.28	2.68
CS1	7128	4.38	2.79
CS1	7155.5	8.25	2.89
A1	7555	2.10	1.40
A1	7605	2.24	1.38
A1	7655	1.94	1.37
A1	7714	4.34	1.46
A1	7752	4.62	1.40
A1	7765	5.12	1.41
G55	7099	0.65	1.36
G55	7149.5	4.28	1.36
G55	7200	2.21	1.39

On SEM images, high density materials (e.g. pyrite) is generally depicted in a bright white color; minerals with densities between 2 to 3 g/cc will be light grey; organic matter will be in dark grey because of the low atomic number, and pore space will be black (Curtis et al., 2012) (Figure 4-2). By setting thresholds of the gray-scale values of SEM images, high density materials (e.g. pyrite), medium density materials (e.g. clay, silica, carbonate particles), OM, and pore space were segmented out (Figure 4-3) (Song et al., under review). We documented pores based on their differences in size, shape, complexity, and location.

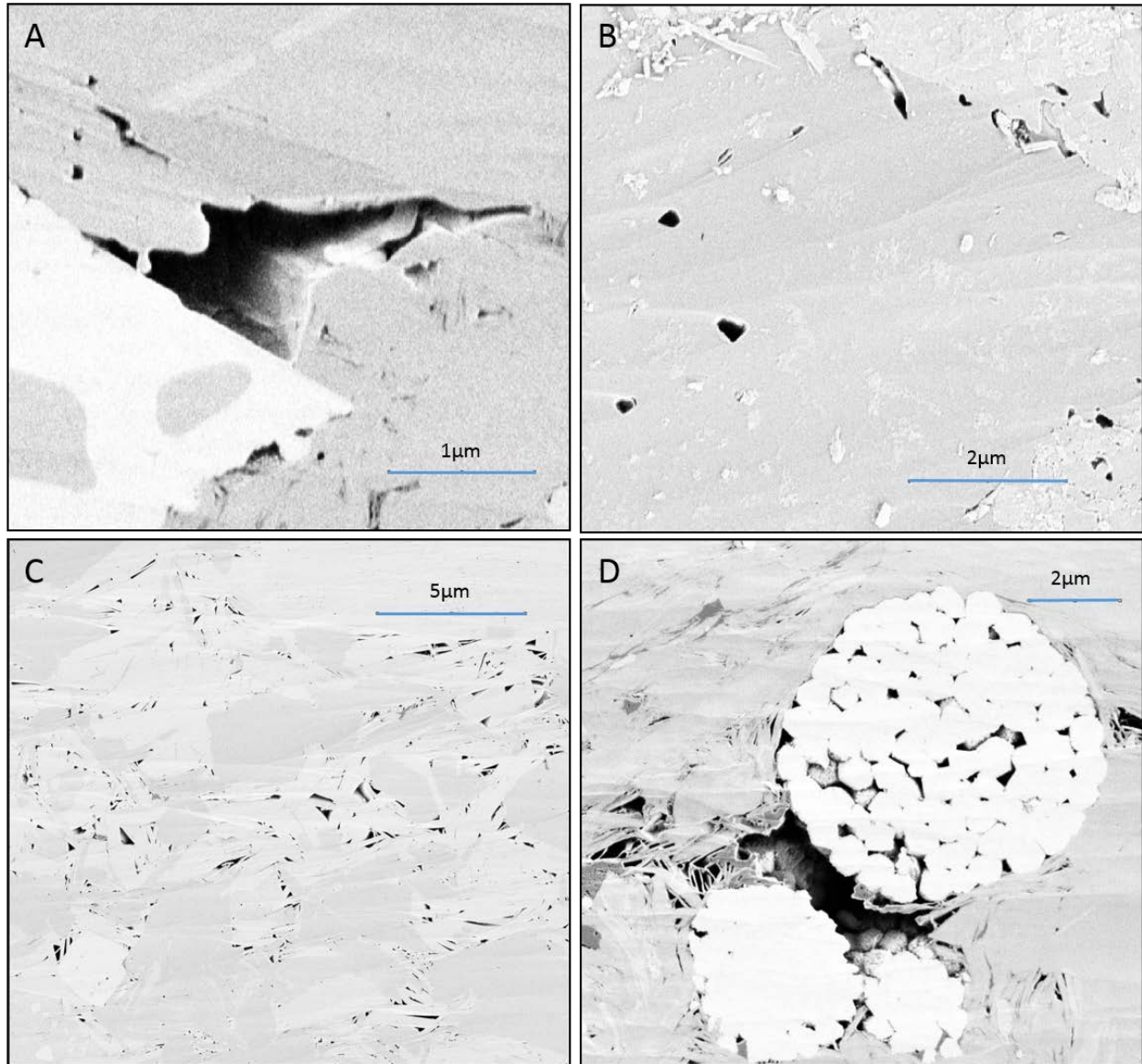


Figure 4-3. Types of mineral-hosted pores. A) Inter-particle pores, samples from well CS1, 7133.75 ft. (2174.37m); B) Intra-particle pores, sample from well A1, 7702.65 ft. (2347.77m); C) Inter-particle pores hosted by clay platelets, sample from well A1, 7620.10 ft. (2322.61); D) Inter- and Intra-particles hosted by pyrite framboids, sample from well CS1, 7082.40 ft. (2058.72m).

SEM-visible porosity, \emptyset_{SEM} , is defined as pore area divide by whole area of a single SEM image. Also, organic matter (OM) and porosity in OM were calculated from digitalized SEM images with the same method. Advanced image processing software (ImageJ and JMicroVision) were utilized for segmenting and analyzing the SEM images quantitatively. Transformation ratio (TR) is used to describe the extent of development of OM pores, which is porosity in organic matter divided by whole area OM covered and the voids in it. $TR = \text{Porosity in OM} / (\text{OM} + \text{Porosity hosted by OM})$.

Due to the differences in illumination of SEM images and, we cannot use a unified series of thresholds to digitalize all the SEM images (Song et al., under review). Bai et al., 2013 also found that porosity measurement was sensitive to the threshold value (in their research, porosity changed from 14% to 49% when threshold increased from 42 to 54) (Bai et al., 2013). An automated workflow was utilized to segment the pores and OM from SEM images (Song et al., under review). The workflow is introduced in detail in Chapter One.

Subcritical Nitrogen Adsorption

Subcritical N₂ adsorption was conducted on a Micromeritics ASAP-2020 instrument at -196⁰C (77K). Approximately 1 gram of shale sample was crushed with mortar and pestle until the whole mass passed through a 60-mesh sieve to prevent potential sample biasing due to sieving. Then samples were set under high-vacuum apparatus at 120⁰C for 24 hours to remove adsorbed water and volatile matter before analyses with N₂. 43 relative-pressure (P/P₀) points ranging from 0.009 to 0.990 were measured on both adsorption and desorption branches (see details in Chapter III). Adsorption branch of the isotherms were used to obtain information about micropores (<2 nm in diameter) and mesopores (2~50 nm in diameter). The classification of pore sizes used in this article follows the classification system of the International Union of Pure and

Applied Chemistry. This classification of pore sizes has proven to be very convenient in coal and shale studies (Bustin et al., 2008; Clarkson et al., 2012; Mastalerz et al., 2013, Kuila 2013, 2016). Specific surface area (SSA) was calculated based on Brunauer-Emmet-Teller (BET) theory (Brunauer et al., 1938). Pore volumes, and pore distributions based on Barrett-Joyner-Halenda (BJH) model, t-Plot, H-K model (Barrett et al., 1951; Sing, 2001).

X-ray Fluorescence (XRF)

X-ray Fluorescence (XRF) was conducted on every sample and had been converted to weight percent of quartz and feldspar, clay, and carbonate to study the heterogeneity and influence of the mineral frameworks on pore structure and SEM-visible porosity (Table 4-3). XRF analysis of these samples were also performed by Ingrain's Digital Rock Physics Lab.

TOC Calculated from Petrophysical Well-logs

TOC was determined using approximately 60 to 100 mg of pulverized mudrock sample in the Source Rock Analyzer (SRA) at the National Energy Technology Laboratory (NETL), Morgantown, West Virginia. Vitrinite reflectance (R_o) was provided by Core Laboratories in Houston, TX as part with a joint industry project, the Marcellus Shale Consortium. Based on the comparison with logs from the same wells, the SRA TOC is strongly correlated with Uranium concentration (in ppm) from spectral gamma ray of cores (Figure 4-4). The TOC of the thirty-two core plugs were determined with the model developed from well logs (Figure 4-4) and results are listed in Table 4-1.

Table 4-3. XRF analysis (normalized to mineralogical composition) of Mahantango Formation and Marcellus Shale.

Well #	Core Depth (ft)	Quartz and Felspar (%)	Clay (%)	Carbonate (%)	Bulk Density (g/cm ³)
CS1	7015.00	31	65	4	2.59
CS1	7036.00	32	63	6	2.56
CS1	7058.45	26	71	3	2.54
CS1	7069.25	26	66	8	2.50
CS1	7082.40	28	69	3	2.61
CS1	7092.92	44	54	2	2.57
CS1	7114.50	39	52	8	2.51
CS1	7124.75	36	60	4	2.53
CS1	7133.75	38	53	9	2.53
CS1	7136.85	30	46	25	2.56
CS1	7148.70	36	60	5	2.50
A1	7547.30	36	63	0	2.63
A1	7591.40	33	63	4	2.69
A1	7620.10	27	56	18	2.77
A1	7677.65	36	64	1	2.62
A1	7688.50	30	69	0	2.58
A1	7702.65	32	67	1	2.52
A1	7720.65	60	38	3	2.46
A1	7729.50	50	44	6	2.40
A1	7740.45	38	60	2	2.45
A1	7753.30	45	46	8	2.47
A1	7778.15	5	3	93	2.66
G55	7078.10	49	50	1	2.36
G55	7084.10	50	47	3	2.46
G55	7113.50	34	63	3	2.66
G55	7122.40	31	65	4	2.64
G55	7128.75	37	60	3	2.46
G55	7135.30	36	63	1	2.51
G55	7141.25	32	49	19	2.59
G55	7162.45	32	57	11	2.48
G55	7201.10	42	56	2	2.36
G55	7217.40	44	33	23	2.40

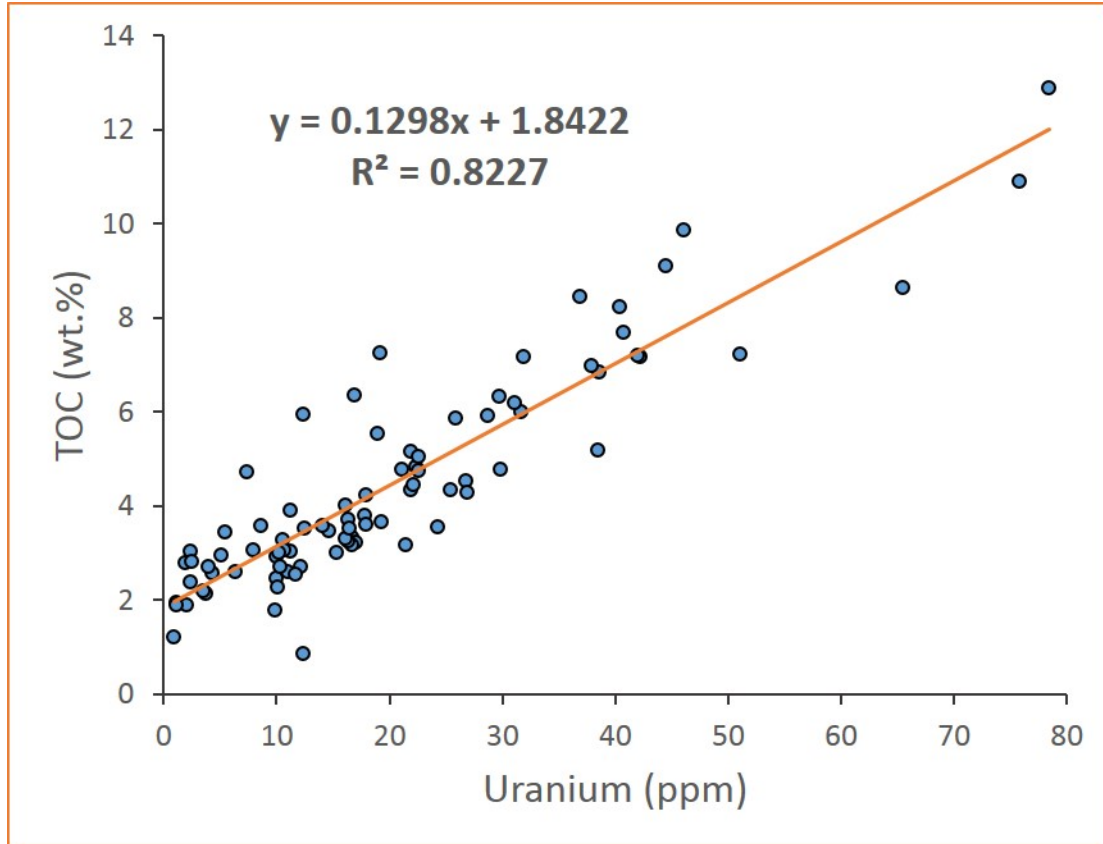


Figure 4-4. Correlation between source rock analysis (SRA) TOC and Uranium from spectral gamma ray from core scanning.

Results

Total Organic Carbon and Thermal Maturity

Generally, the TOC of Marcellus Shale is higher than that of the Mahantango Formation, and that of lower shale unit of the Marcellus is higher than upper Marcellus shale unit. TOC values for the Mahantango Formation range from 0.08 to 3.72 %, with an average value of 1.41%, and the values of the Marcellus Shale are from 2.15 to 6.83 % with an average value of 3.69 %. TOC values show an overall increase with depth through the Marcellus Shale.

The average vitrinite reflectance value for the six samples in well A1 is 1.40% (depth ranges from 7555 ft. [2303m] to 7765 ft. [2367m]), indicating thermal maturity in the present day dry gas zone. The average vitrinite reflectance value for four samples in well G55 is 1.37% (depth ranges from 7053 ft. [2150m] to 7200 ft. [2195m]), indicating thermal maturity in the present-day condensate/wet gas zone. The average vitrinite reflectance value for five samples in well CS1 is 2.67% (depth ranges from 7019 ft. [2139m] to 7155.5 ft. [2181m]), indicating thermal maturity in post-mature dry-gas zone.

Mineral-hosted pores

Mineral-hosted pores are ubiquitous throughout Mahantango and Marcellus formations (Figure 4-3). These pores are formed by both depositional and diagenetic processes (Loucks et al., 2012). Pores are also affected by mineralogy, arrangement, size, and sorting of grains (Loucks et al., 2012), and composition and maturity of OM (Schieber, 2013). Mineral hosted pores can be subdivided into inter-particle (Figure 4-3 A, C) and intra-particle pores (Figure 4-3 B, D), and they define the framework of the pore system. Figure 4-3 C illustrates triangular pore spaces defined by randomly oriented clay mineral platelets. They were well-preserved in some clay-rich layers, where supported by rigid grains that could protect from mechanical compaction. These triangular pores are usually in the hundreds of nanometers size-range. Intergranular pores hosted by quartz, feldspar, mica, and carbonate grains are also common in the studied samples, and the size of these pores is from hundreds of nanometers to a few micrometers.

Dissolved moldic porosity is developed in carbonate, some of which are recognizable bioclasts (Figure 4-5 A). Some of the moldic porosity is filled with OM (yellow arrows), others are unfilled (blue arrows). Schieber (2013) argued that the presence of dissolved carbonate-margins was associated with organic acids (phenolic and carboxylic acids) during late diagenetic

stages (Schieber, 2013). In every well, mineral-hosted porosity, pore size distribution, and types show substantial heterogeneity. However, the overall abundance of mineral-hosted pores decreases with burial depth. Abundance and distribution of clay minerals and OM are major factors that control mineral-hosted porosity.

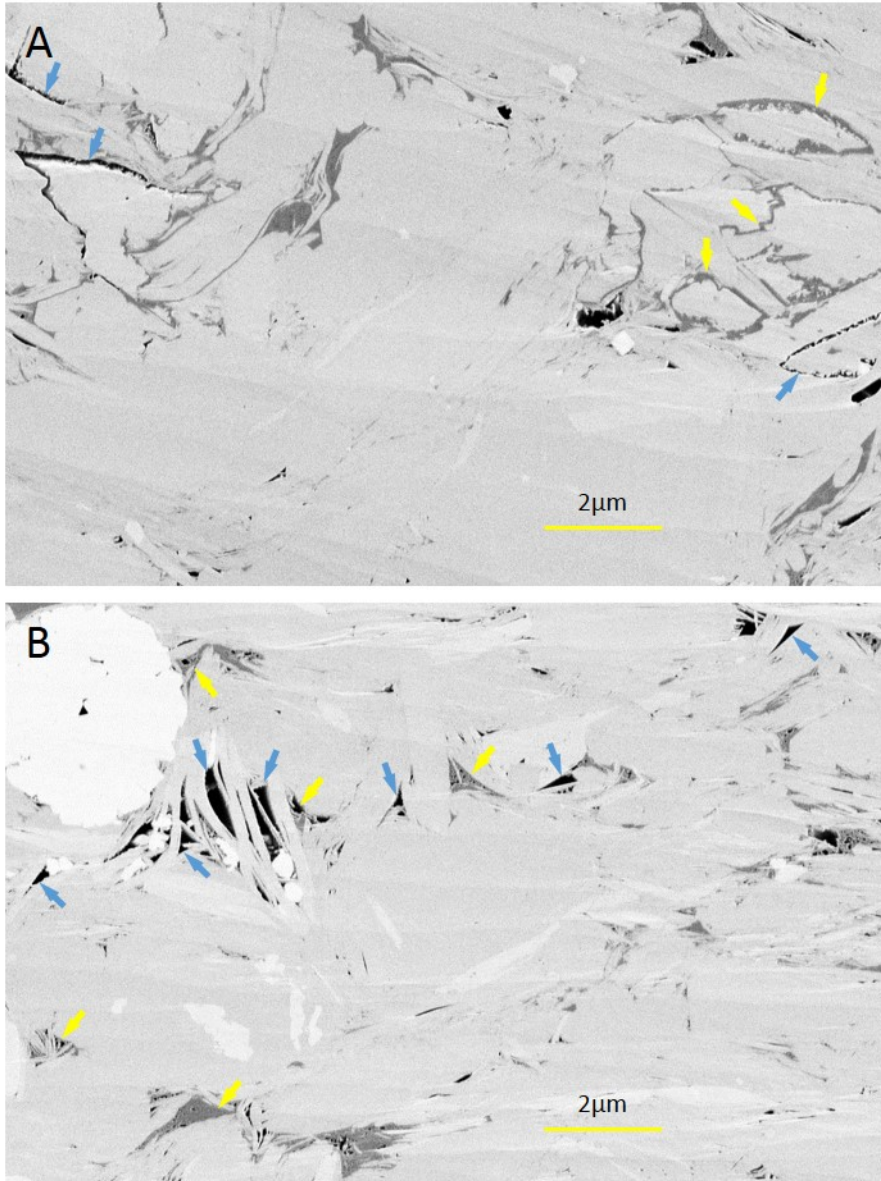


Figure 4-5. A) Dissolution pores along margins of carbonate grains. Blue arrows point to dissolution porosity, and yellow arrows point to original dissolution porosity filled by secondary OM. Sample from well CS1, 7114.50 ft. (2168.50m). B) Triangular pores hosted by clay platelets (phyllosilicate grains). Blue arrows point to inter-particle porosity (phyllosilicate porosity), yellow arrows point to phyllosilicate porosity filled by secondary OM. Sample from well CS1, 7036.00 ft. (2144.57m).

OM-hosted pores

OM hosted pores occur in most samples, and range from tens to hundreds of nanometers. All the OM in our samples is amorphous OM (Schieber, 2013), or secondary OM (Pommer and Milliken, 2015). No structured OM has been identified in any of the samples. Three types of pores have been observed within OM: (1) spongy pores, (2) bubble pores, and (3) complex pores. Spongy pores (Figure 4-6) are the most common OM-hosted pore type in the Marcellus Shale. Spongy pores are large amount of tiny pores with a similar pore-size. Complex pores (Figure 4-6) are also very common. Complex pores are OM pores that include mineral-matrix forming a complex pore network, which are OM pores in contact with mineral surfaces of the rock matrix. Their shape varies, and their size can be from tens of nanometers to about a micrometer. Bubble pores (Figure 4-6) feature a bubble shape with curvature, and a bright edge. Bubble pores can be hundreds of nanometers in diameter. The shape and texture of bubble pores suggest that they were formed in fluid phase, and are likely being remnant bitumen (Bernard et al., 2013; Schieber, 2013; Pommer and Milliken, 2015). Bubble pores are very rare in the Marcellus Shale. Fractures in OM or between OM and minerals are also observed, and could be attributed to pressure release or shrinkage of OM during sample preparation. Fractured OM can hardly exist in an in-situ condition/subsurface before fracture stimulation. However, after reservoir simulation, they can exist and strongly enhance the permeability by connecting the smaller pores. Observed fracture OM porosity size varies, but usually are 50 to 100 nm wide and as long as several micrometers.

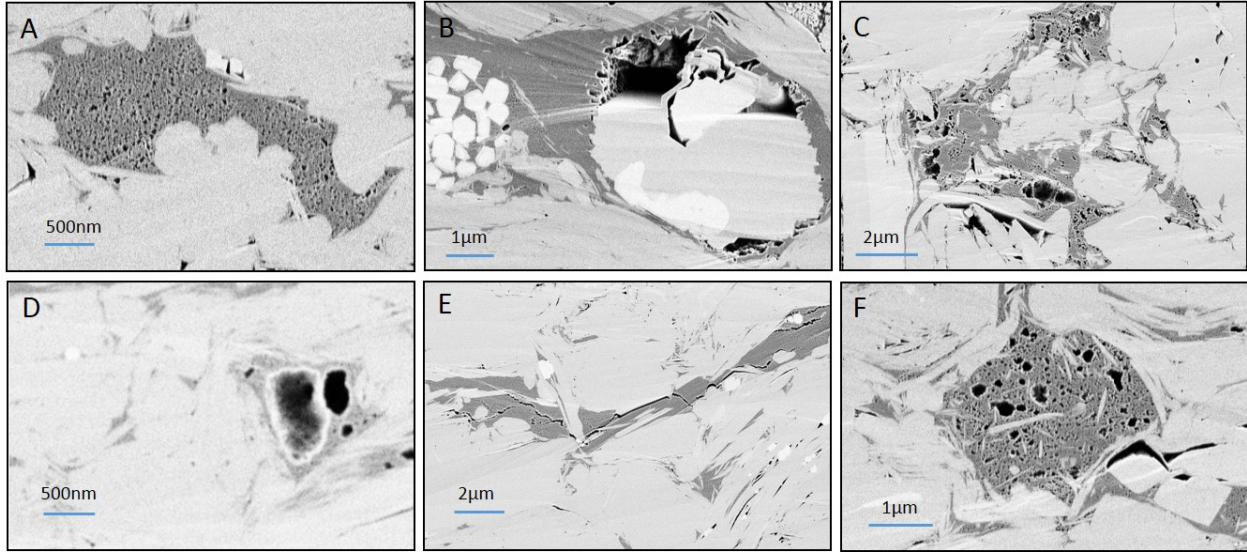


Figure 4-6. OM pore types. A) Spongy pores within a piece of secondary OM, sample from well CS1, 7133.75 ft. (2174.37m); B) Complex OM pores hosted by OM associated with minerals, porous nature of OM is demonstrated by the inner structure of OM. Sample from well CS1, 7058.45 ft. (2151.42m); C) OM pores within secondary OM. Pore size varies significantly. Sample from well G55, 7141.25 ft. (2176.65m); D) Bubble porosity hosted by OM. Sample from well A1, 7720.65 ft. (2353.25m); E) Open fractures within OM and minerals, sample from well A1, 7547.30 ft. (2300.42m); F) OM pores within secondary OM. Pore size varies significantly. Sample from well CS1, 7114.50 ft. (2168.50m).

Compaction

Mechanical compaction altered the pore structure significantly. Yet some pores are preserved next to the compaction-resistant grains or voids between them (Figure 4-7).

Compaction has been observed in the following scenarios:

- 1) Deformation of ductile grains, often occurred next to rigid grains (Figure 4-7A, C), resulted in deformation of secondary OM in between,
- 2) Parallel alignment of clay grains near rigid grains (Figure 4-7B),
- 3) Rigid grains holding triangular pore-spaces between clay platelets (Figure 4-7D), and
- 4) Preservation of inter-particle pores between rigid grains (Figure 4-3 A, C, D).

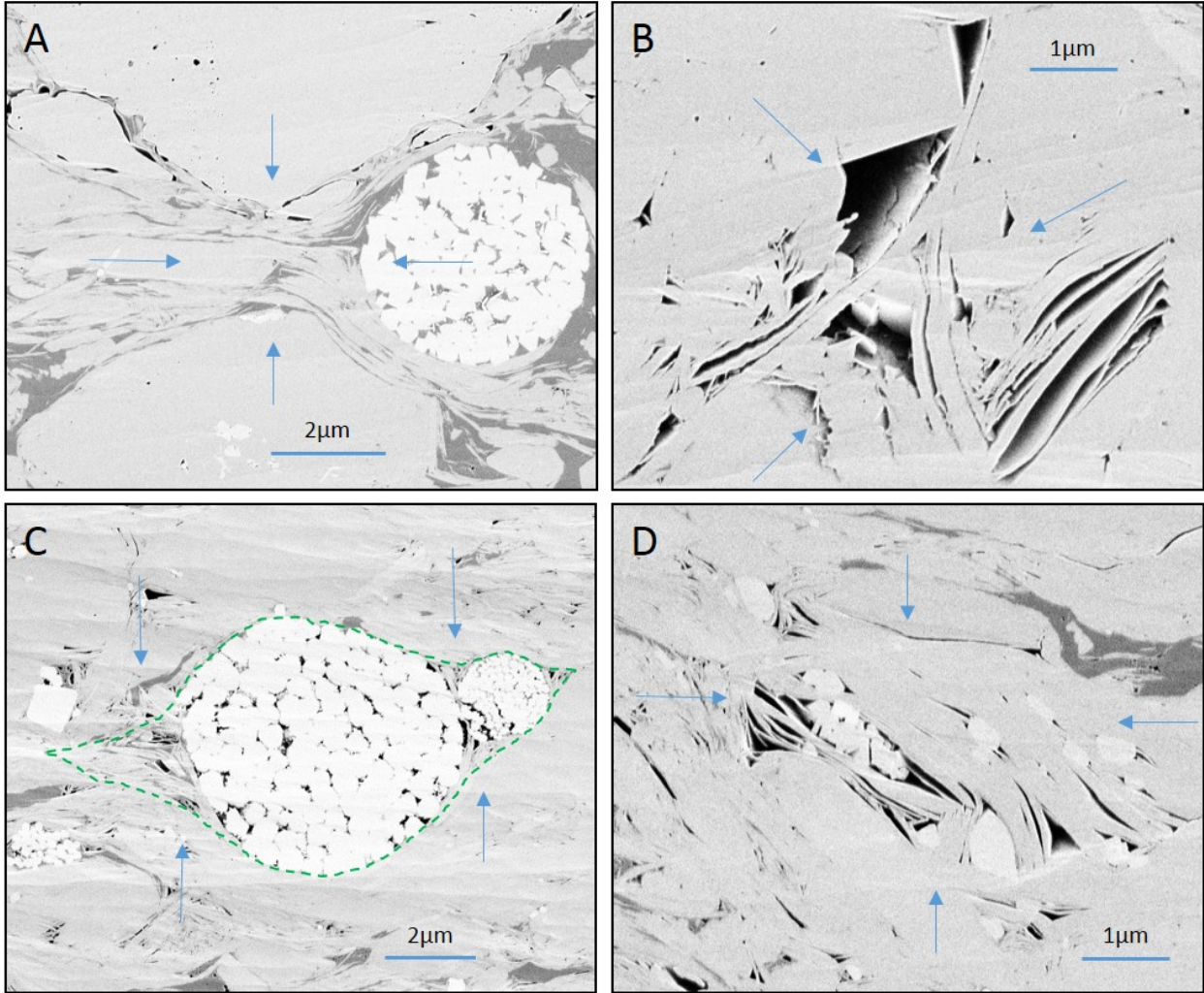


Figure 4-7. Images demonstrating compaction. A) Clay and mica bend around pyrite framboid and other mineral grains. Sample from well A1, 7729.50 ft. (2355.95m). B) Compactional bending of clays around more rigid grains. Sample from well G55, 7141.25 ft. (2176.65m). C) Clays bend around pyrite framboids, green dash line marking the pressure surrounding pyrite framboids. Sample from well CS1, 7082.40 ft. (2158.72m). D) compression of a vertically oriented phyllosilicate grain produced pores because of splits between phyllosilicate sheets. Sample from well CS1, 7133.75 ft. (2174.37m).

Stratigraphic distribution of pore micro-textures

Four pore micro-textures are identified from our samples. They are affected by both mineral matrix and OM. Within each well, mineral-hosted pore volume, size distribution, and pore types show substantial heterogeneity. However, the abundance and distribution of OM and clay minerals are major controls on pore textures.

Clay-rich matrices have porosity dominated by clay mineral-hosted pores comprising large portions of the bulk volume (Figure 4-8C). This type of reservoir is typically found in the middle section of Mahantango Formation, where the OM is less than 1%. The magnitude of mineral-hosted porosity and pore size is positively correlated with clay abundance. Most of the pores are hosted by the clay particles, and are mostly triangular shape, and of a similar size (Figure 4-8C).

In the lower section of Mahantango Formation and upper Marcellus Shale, the pore system is made up of both OM-hosted pores and mineral-hosted pores. Pore size and pore shape vary significantly (Figure 4-8B).

Organic-rich horizons were observed in the middle and lower Marcellus shale units in two wells (G55 and A1). The TOC value of these horizons is higher than 4.5%. In these horizons, most of the pores hosted by the mineral matrix have been filled with secondary OM content (Figure 4-8A). The porosity observed and segmented from SEM images is the lowest in these organic-rich Marcellus shale units.

There are several carbonate-rich horizons developed in Marcellus Formation. The pore structure in the carbonate rich horizons consists of only a few isolated intra-particle pores between the carbonate grains, and the OM content is much lower compare to other non-carbonate layers (Figure 4-8D).

Table 4-4. Porosity Measurement from digitalized Scanning Electron Microscopy (SEM)

Images. OM: organic matter, TR: transformation ratio.

Well ID	Depth (ft)	Porosity %	OM	Porosity in OM	TR
CS1	7015.00	1.2395	2.8321	0.4507	0.137291
CS1	7036.00	0.6998	2.6815	0.2339	0.080229
CS1	7058.45	1.5851	6.2865	0.1421	0.022104
CS1	7069.25	1.431	5.8885	0.1296	0.021535
CS1	7082.40	1.2918	4.3947	0.3177	0.067418
CS1	7092.92	1.088	5.6891	0.285	0.047706
CS1	7114.50	1.427	5.9014	0.9344	0.136692
CS1	7124.75	1.5003	3.7709	0.417	0.099573
CS1	7133.75	2.7583	5.4442	0.7568	0.122045
CS1	7136.85	1.6257	4.2847	0.2947	0.064353
CS1	7148.70	1.0406	5.307	0.2082	0.03775
A1	7547.30	0.5257	3.6659	0.2243	0.057658
A1	7591.40	0.2662	1.0063	0.0191	0.018627
A1	7620.10	0.5747	1.0042	0.0186	0.018185
A1	7677.65	0.3516	5.0943	0.0853	0.016468
A1	7688.50	0.2737	7.8699	0.093	0.011679
A1	7702.65	0.5629	7.5662	0.1367	0.017747
A1	7720.65	0.4903	13.5197	0.2623	0.019032
A1	7729.50	0.1205	20.7355	0.0349	0.00168
A1	7740.45	0.2863	11.9881	0.0921	0.007624
A1	7753.30	0.2963	12.0997	0.1413	0.011543
A1	7778.15	0.4313	6.1643	0.1055	0.016827
G55	7078.10	0.6191	15.1776	0.3426	0.022074
G55	7084.10	1.2767	8.7827	0.7373	0.077447
G55	7113.50	0.6798	1.2191	0.0204	0.016458
G55	7122.40	0.6283	1.6785	0.0266	0.0156
G55	7128.75	0.8514	6.6431	0.1967	0.028758
G55	7135.30	0.7219	3.5223	0.2877	0.075512
G55	7141.25	1.2211	2.7886	0.207	0.069101
G55	7162.45	0.5204	5.7171	0.1711	0.029058
G55	7201.10	0.6754	13.2502	0.3569	0.026229
G55	7217.40	0.4349	15.6849	0.0994	0.006297

Table 4-5. Porosity, OM, porosity in OM, and transformation ratio (TR) of four pore-micro-
texture-facies.

Organic Rich				
	Porosity (%)	OM (%)	Porosity in OM	TR
Mean	0.4175	14.6365	0.1899	0.0135
Max	0.6754	20.7355	0.3569	0.0262
Min	0.1205	11.9881	0.0349	0.0017
Organic Lean				
	Porosity (%)	OM (%)	Porosity in OM	TR
Mean	1.1207	5.3394	0.3198	0.06
Max	2.7583	8.7827	0.9344	0.1373
Min	0.2737	2.7886	0.0853	0.0117
Clay Rich				
	Porosity (%)	OM (%)	Porosity in OM	TR
Mean	0.57	1.52	0.06	0.03
Max	0.7	2.68	0.23	0.08
Min	0.27	1	0.02	0.02
Carbonate Rich				
	Porosity (%)	OM (%)	Porosity in OM	TR
	0.43	6.16	0.11	0.02

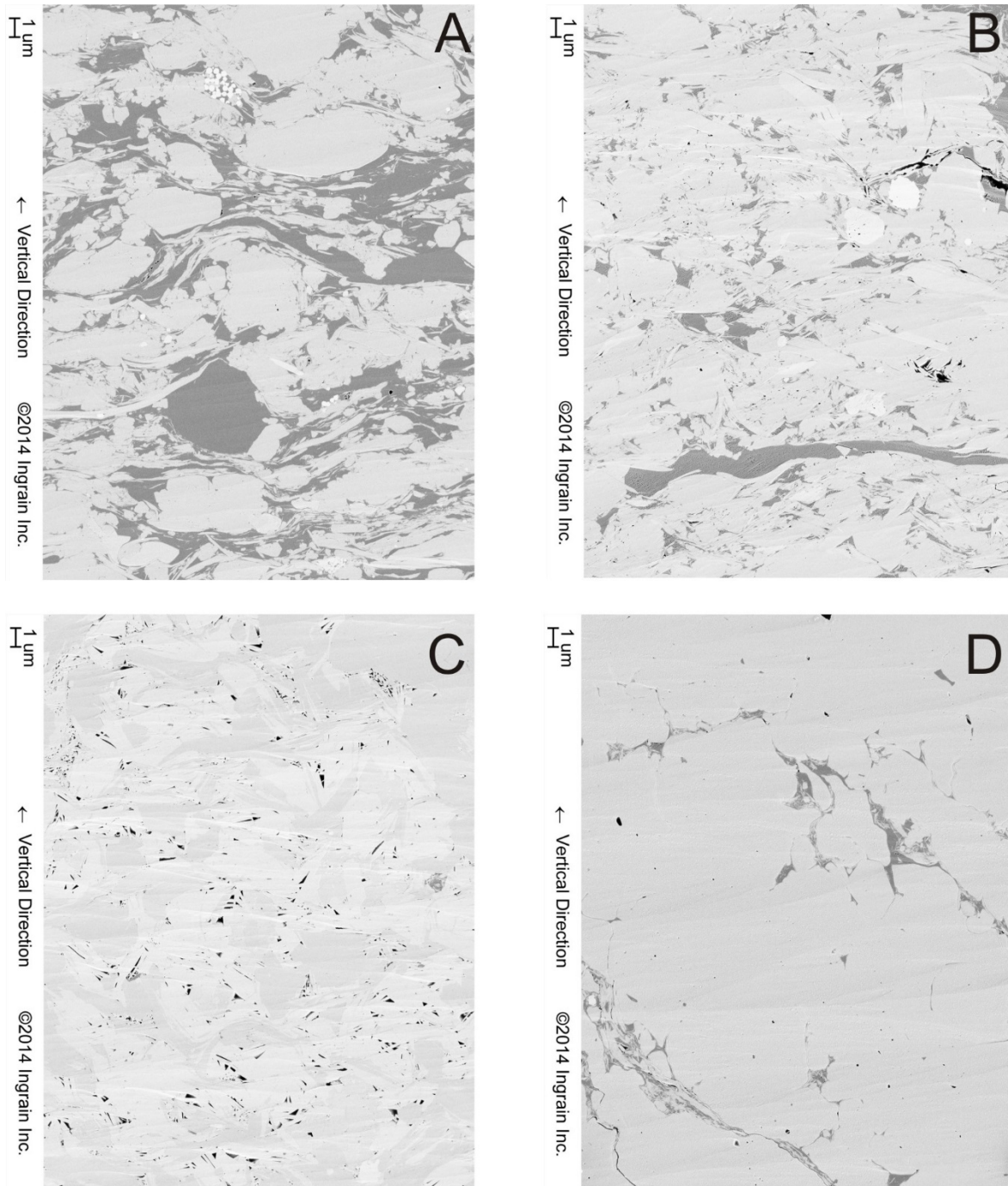


Figure 4-8. Typical SEM images for four different pore micro-facies in the Marcellus Shale. A: organic rich, sample from well A1, 7729.50 ft.; B: organic lean, sample from well G55, 7084.10 ft.; C: clay rich, sample from well A1, 7620.10 ft.; D: carbonate rich, sample from well A1, 7778.15 ft.

Pore surface area, pore volume, and pore size distribution

BET specific surface area (SSA), BJH pore volume, and pore size distribution in the Mahantango and Marcellus were determined by subcritical nitrogen adsorption analysis (see details in Chapter III) (Table 4-4, Figure 4-9). The PSD results from nitrogen adsorption shows substantial variation with mineralogy and organic content. Samples with higher TOC show significantly larger amount of smaller pores (pore size < 5nm) (Figure 4-9). Organic content shows a strong positive correlation with both SSA and pore volume (Figure 4-10).

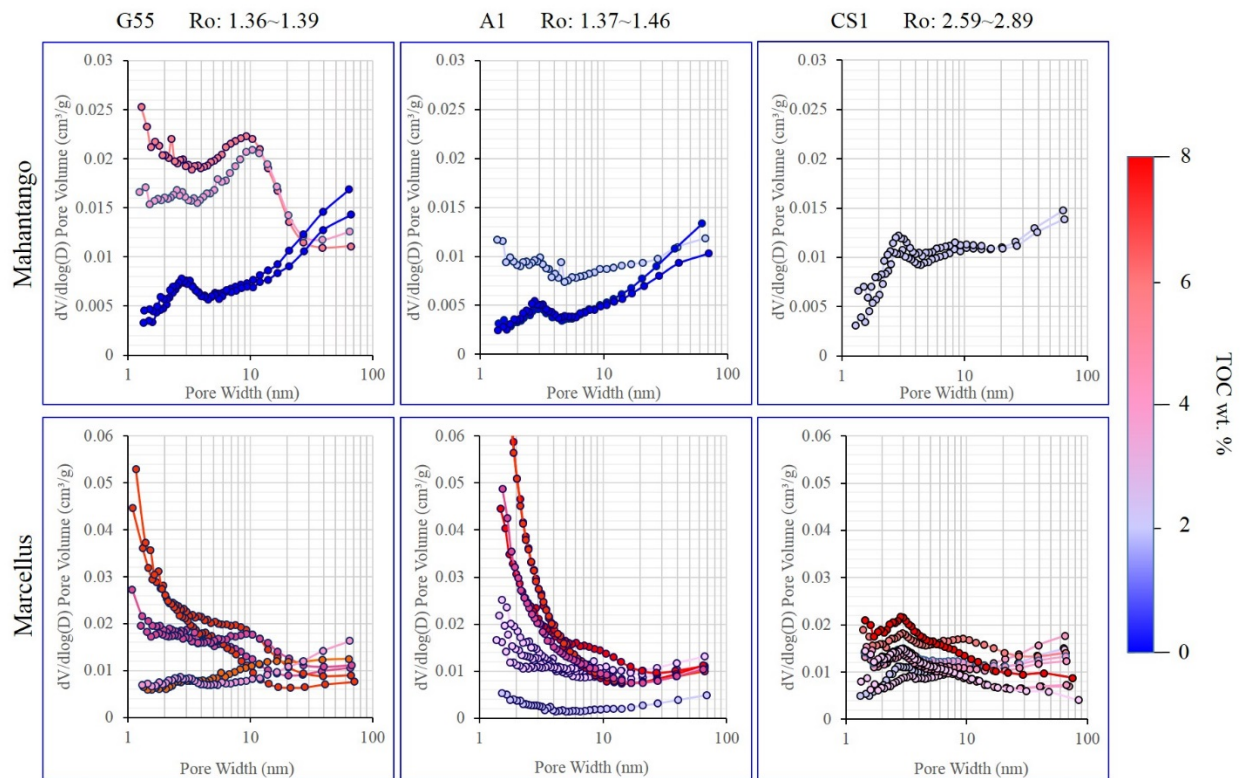


Figure 4-9. Pore size distribution from BET analyses calculated by BJH model. Data series are color coded by TOC value of the sample. Warmer color represents higher TOC.

Table 4-6. Test results of subcritical nitrogen adsorption. Specific surface area (SSA) is based on BET model, micropore area and volume are based on t-plot method, and pore volume is based on BJH model.

Well #	Core Depth	BET SSA (m ² /g)	Micropore Area (m ² /g)	Micropore Volume (cm ³ /g)	BJH Pore Volume (cm ³ /g)
G55	7078.10	29.09	4.0252	0.001651	0.037573
G55	7084.10	22.43	1.7668	0.00069	0.033389
G55	7113.50	7.82	0.9366	0.000413	0.019997
G55	7122.40	8.27	1.1564	0.000504	0.018888
G55	7128.75	23.36	2.8235	0.00115	0.03233
G55	7135.30	10.60	0.3003	0.000089	0.021914
G55	7141.25	10.51	1.2105	0.00051	0.021757
G55	7162.45	23.94	3.6507	0.001513	0.02957
G55	7201.10	33.17	6.2917	0.002597	0.037619
G55	7217.40	32.15	7.5904	0.00317	0.032029
A1	7547.30	13.47	2.9135	0.001241	0.021396
A1	7591.40	5.75	1.2198	0.000534	0.014412
A1	7620.10	5.41	0.854	0.000377	0.013893
A1	7677.65	20.35	6.4096	0.002748	0.025313
A1	7688.50	20.47	6.3455	0.002718	0.024386
A1	7702.65	17.41	4.2973	0.001818	0.024192
A1	7720.65	34.42	10.4729	0.004455	0.036452
A1	7729.50	46.97	19.2261	0.008246	0.042674
A1	7740.45	44.85	18.0088	0.007729	0.041304
A1	7753.30	32.37	11.5764	0.004955	0.032259
A1	7778.15	4.42	1.4649	0.000626	0.00714
CS1	7015.00	9.89	0.8381	0.000381	0.02215
CS1	7036.00	12.26	1.9438	0.000852	0.023407
CS1	7058.45	11.21	1.242	0.000551	0.023166
CS1	7069.25	15.53	3.745	0.001624	0.020434
CS1	7082.40	17.42	4.5674	0.001985	0.028831
CS1	7092.92	11.91	2.3431	0.000996	0.022793
CS1	7114.50	22.44	5.0918	0.002189	0.032929
CS1	7124.75	14.98	3.5893	0.001557	0.01968
CS1	7133.75	17.44	4.1508	0.001799	0.026916
CS1	7136.85	17.12	4.627	0.00201	0.025637
CS1	7148.70	16.13	3.9258	0.001703	0.021272
CS1	7145.00	23.50	5.6754	0.002462	0.030931
CS1	7154.75	34.77	8.3233	0.00361	0.04567

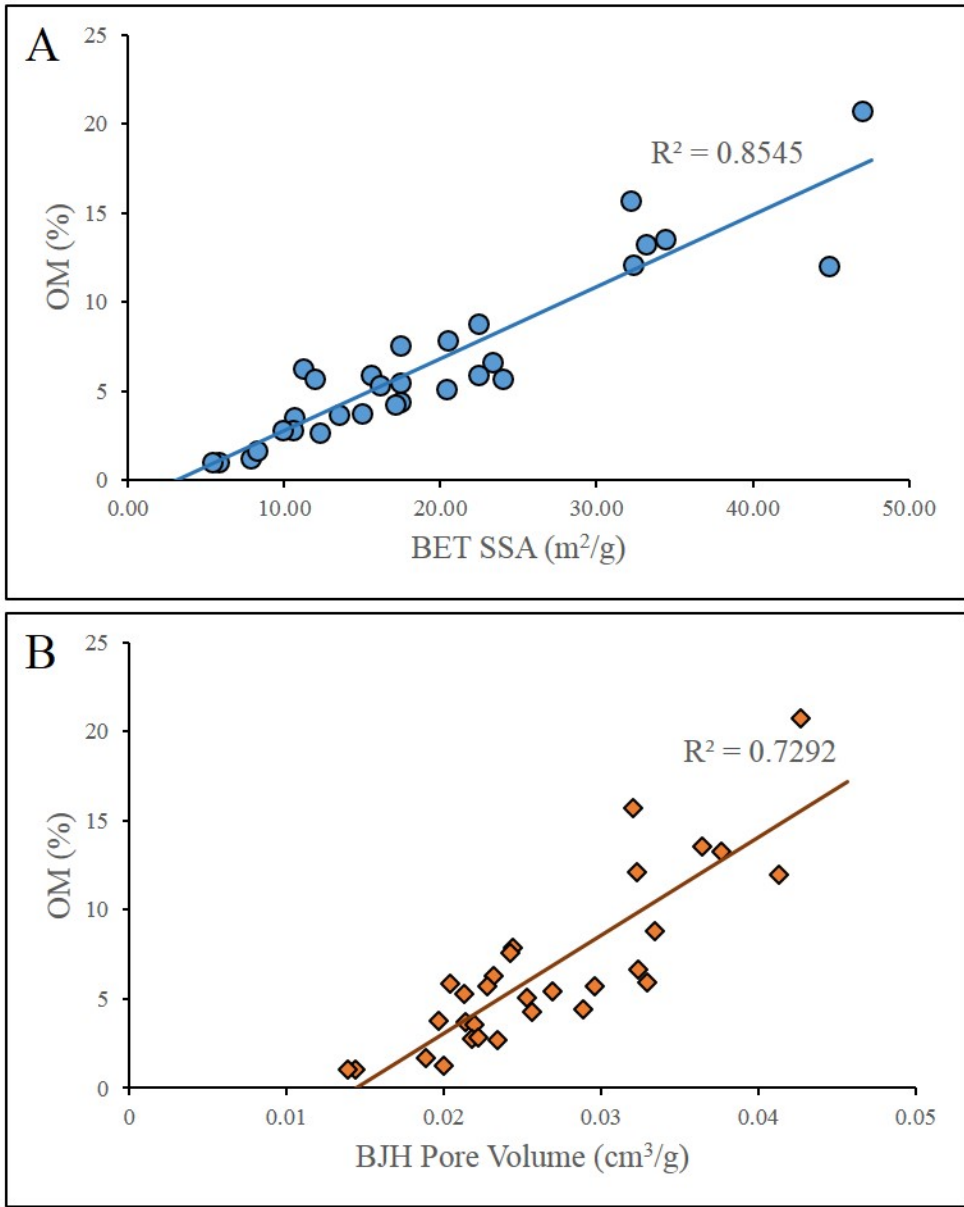


Figure 4-10. OM recognized from SEM images plots against BET specific surface area (SSA) and BJH pore volume.

Discussion

Data validation

The heterogeneity in mudstone and the limited size of SEM view add substantial uncertainty to the image-quantification results. In this research, we applied a semi-automated and objective workflow (Song et al., under review). However, error and sample bias derived from size limitation of SEM view is inevitable. To test the feasibility of our methodology, the percent of OM is compared to bulk weight percent TOC (Figure 4-11). The result shows a strong positive correlation between TOC and OM, and a strong negative correlation between bulk density and OM, which suggests that the integrated methodology of SEM imaging and digitizing provide an adequate representation of the porosity and PSD in the sample volumes.

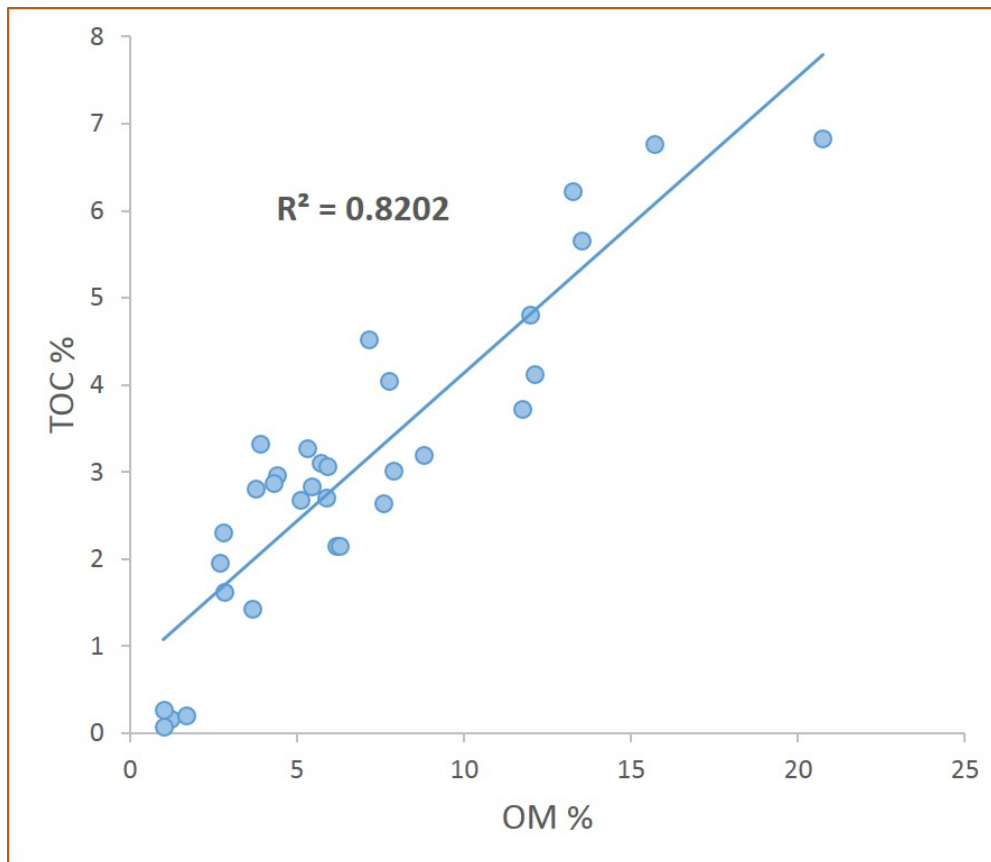


Figure 4-11. Total organic carbon (TOC) in weight percentage plotted against organic matter (OM) recognized from SEM images. The strong positive correlation indicates a good representativeness of the SEM images.

Mineralogy and Porosity

When muddy detritus was deposited, the primary porosity could be 80 to 90%, but compaction, dewatering, and cementation destroys most of the primary porosity (Schieber, 2013).

The mineral composition of formations controls the preservation of primary porosity and potential secondary porosity development in mudrocks. In fact, the majority of SEM-visible porosity is contributed by the mineral framework, which are usually inter-particle, intra-particle, or carbonate-dissolution pores (Figure 4-3), and the size of these pores ranges from several hundred nanometers to more than a micrometer. The mineral frameworks in the Hamilton Group (Mahantango Formation and Marcellus Shale) consists of a mixture of clay minerals (mainly illite, small portion of chlorite in Mahantango and Upper Marcellus), quartz grains, carbonate grains (dolomite and calcite), and pyrite. Within all of them, clay particles are the most active component of pore-development in mudrock reservoirs (also see Schieber 2013, “phyllosilicate framework pores”). Pyrite frameboids are also very ubiquitous. They can host isolated intra-particle pores, or be loosely clustered to form porosity connected to the whole pore-system.

Compaction-resistant pressure shadows adjacent to mechanically competent grains (e.g. quartz, feldspar, dolomite, calcite, and pyrite) help preserve the pore space between clay-particles (Schieber, 2013). However, during thermal maturation, in organic-rich intervals, liquid OM can fill these primary pores in the mineral frameworks, which decreases the overall porosity until the OM starts to generate hydrocarbons. It also implies that those filled primary porosity were inter-connected by nature, and that the nano-porous secondary OM may be inter-connected. Based on our observations, nearly all the porous OM are intermingled with mineral particles. During the diagenetic and maturation processes, most of primary porosity is destroyed by compaction, cementation, and occlusion by OM (Loucks et al., 2012; Milliken et al., 2012). On the other hand, secondary porosity, like pores in OM and dissolution pores on the edges of carbonate grains, are better preserved.

Migration pathways through blocks bounded by hydraulic fractures are of great importance to continued shale gas production. Micro-fractures in OM represent a key control for gas transfer from the shale matrix to the fractures (natural or artificial) and strongly affect the “matrix” permeability, and affect the potential for commercial gas production from mudrock.

Organic Matter and Porosity

The inter-connecting network of OM and porosity in OM has been shown through SEM imaging of 3D organic-shale volumes (Sondergeld et al., 2010; Curtis et al., 2012). TOC has been considered as one of the most important parameters of shale reservoirs, and TOC has a positive correlation with physical properties of formations (Passey et al., 2012; Bohacs et al., 2013; Milliken and Day-Stirrat, 2013). Previous studies find that there is a positive correlation between TOC and bulk porosity as acquired by Gas Research Institute (GRI) method (Luffel and Guidry, 1992, Song et al., in prep).

SEM integrated with ion milling provide a direct observation of OM in mudrock reservoir. In this dataset, the occurrence of OM is amorphous, and it fills the pre-existing pore spaces hosted by mineral frameworks. The distribution of OM demonstrates that magnitude of porosity loss through OM filling is significant. Secondary OM occupies spaces similar in morphology and size to phyllosilicate pores, and dissolution pores on the edge of carbonates grains. In addition, secondary OM coats euhedral pyrite crystals and fills inter-particle pores. The pore-filling OM also provides the potential connectivity of pre-existing pores hosted by mineral frameworks, and for inter-connectivity of particulate OM and OM-hosted pores. In some cases, OM was not observed filling all the inter-particle pores (Figure 4-3). Two possible explanations are 1) shortage of OM that could not fill all the pores, and 2) unfilled mineral-hosted pores are not inter-connected. The preference of OM-filling implies a better connectivity. OM-hosted pores

within this inter-connected OM is enhanced compared to pores within particulate OM. Larger OM-hosted pores occur within samples with greater amounts of rigid grains and correspondingly larger intergranular volumes, where pores have a better chance to be preserved within OM (Pommer and Milliken, 2015).

Large pieces of OM with minimum amount of SEM visible porosity were observed in the most organic-rich samples A1-7729.50 ft. and G55-7217.40 ft. (Figure 4-8, Figure 4-12). The OM volumetric percentage of these two samples are 20.74% and 15.68% respectively, and OM-hosted pore composes 3.5% and 9.9% of the whole pore system. Digitized SEM images results show that there is a negative correlative between OM volumetric percentage and SEM visible porosity (Figure 4-13), as previous noticed by research conducted by Millken et al., 2013. However, the results from BET analysis tell a completely different story. Figure 4-10 shows that with increasing TOC, pore surface area and volume increases significantly. The X axis intercepts of Figure 10 A and B indicate the pore surface area and pore volume with zero OM. BET results demonstrates that significant pores volumes are present in those very organic-rich samples, while SEM images indicate that these organic-rich samples with most of the OM are non-porous (Figure 4-13). The negative correlation between OM and TR seems to indicate that in the organic-rich samples, less OM has been transformed to pores (Figure 4-14). One possible explanation is the size of these pores is below the resolution of SEM. In this study, the resolution of our SEM images is 10 to 15 nm. Whereas the majority of the pore system as measured by BET test is smaller than 5nm. Milliken et al. (2013) argued that in the highest TOC samples, over 90% of the pores were below the size of imaging by SEM.

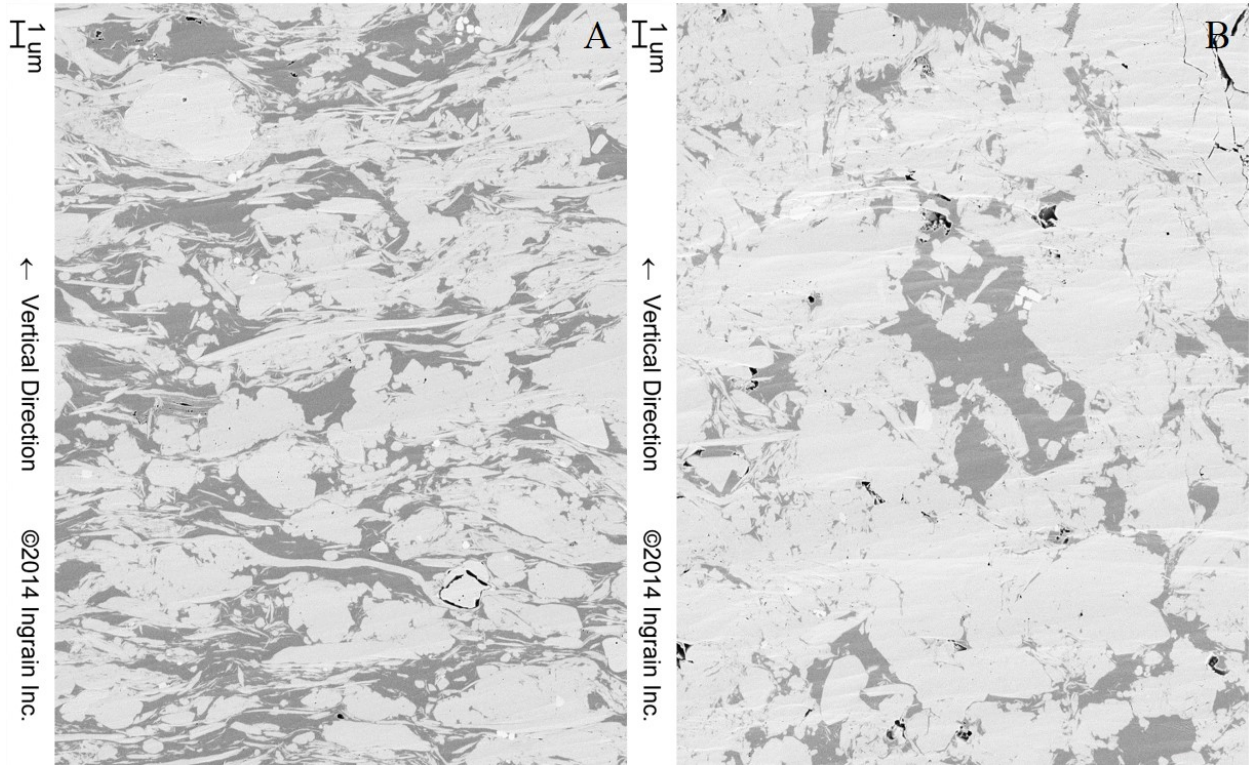


Figure 4-12. SEM images illustrating large pieces of OM with no SEM-visible porosity. Sample A came from well A1, 7729.50 ft., and sample B came from well G55 7217.40 ft.

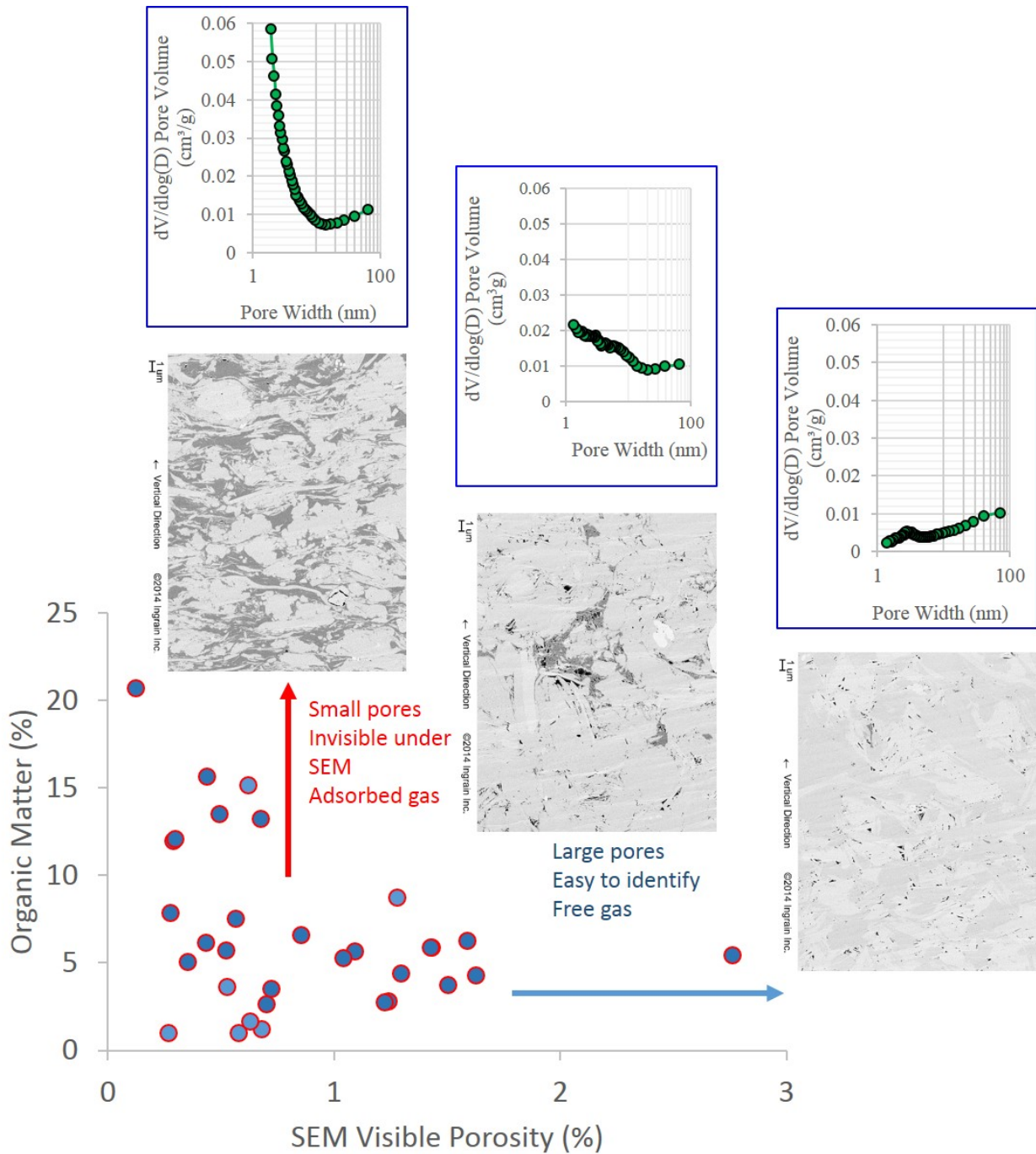


Figure 4-13. Negative correlation between SEM-visible porosity and organic matter. As richness of OM increases, less pores are visible under SEM. However, BET analysis shows that organic-rich samples have substantial amount of pores smaller than 10 nm.

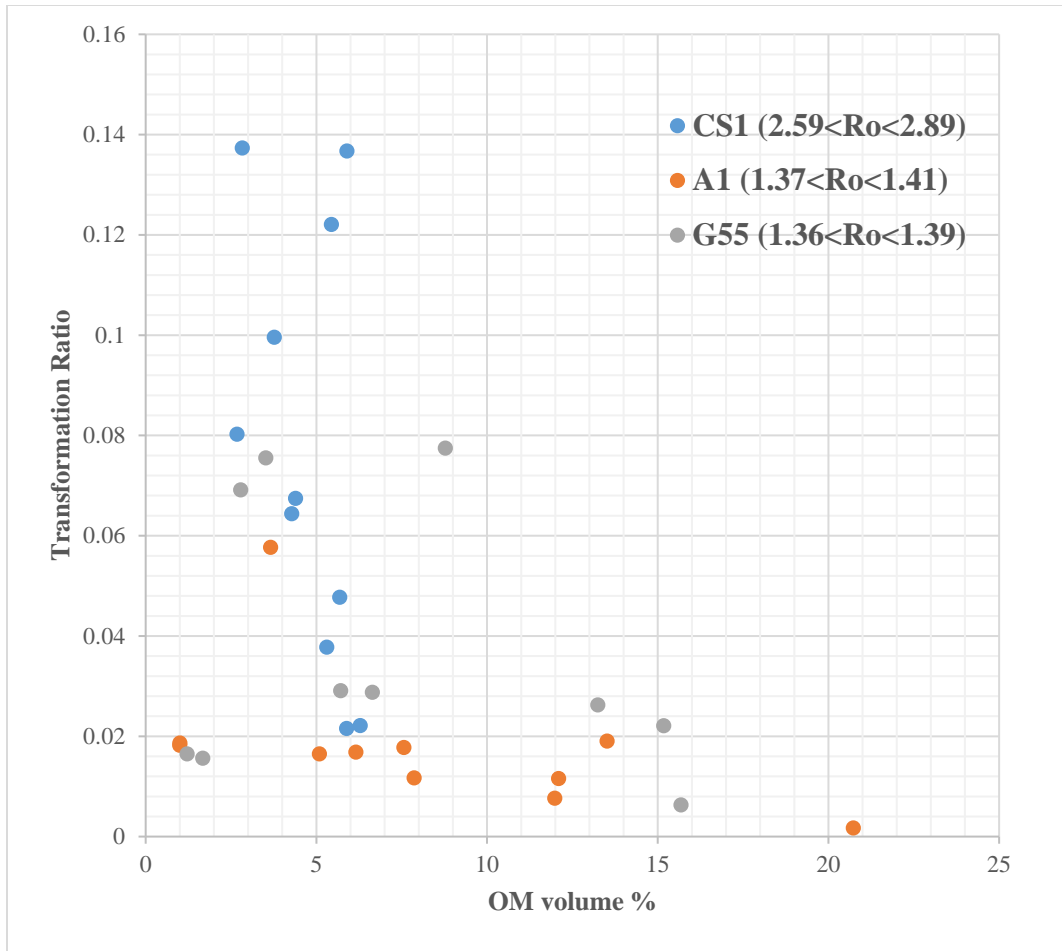


Figure 4-14. The correlation between transformation ratio (TR) and OM volume%. TR is defined as porosity in organic matter divided by whole area OM covered and the voids in it. We use this index to describe the extent of development of OM pores. Notice the weak negative correlation between them.

Unlike SEM-resolvable pores, which are preserved by compaction-resistant grains, the preservation mechanism for smaller OM-hosted pores is unclear. Abnormal pore pressure has a potential to be the reason. High-pore-pressure has been reported in the Marcellus Shale, and it

shows a positive effect on the productivity of shale-gas reservoir (Zagorski et al., 2012).

Depending on the pore pressure, amorphous pore-filling OM could potentially accommodate additional strain as a consequence of volume loss during compaction and after expulsion of mobile bitumen and volatiles, especially in OM-rich samples (Pommer and Milliken, 2015).

A piece of OM that is not porous on the scanned surface, but this image also captures some of the inner structure of the OM, and it is porous on the side featuring the complex pore (Figure 4-6 B). This is a good example about the limitation of SEM investigation of OM-hosted porosity. Resolution is not the only limitation, and requires further research.

In summary, the generation mechanism of OM-hosted pores can be concluded by two steps: (1) compaction, cementation, and infill of pore space with secondary OM are destructive of primary, mineral-hosted porosity; (2) secondary porosity within OM is generated during and after hydrocarbon generation. Pore-shaped spaces occupied by OM suggests that compaction plays a significant role at the preservation of OM-hosted pores.

Stratigraphic Distribution of Pores

Similarities have been noticed in the pore types and morphology in specific horizons. We categorized these similarities into four pore-micro-texture facies, namely clay-rich, organic-lean, organic-rich, and carbonate-rich. The stratigraphic distribution of pore structure in the Mahantango, upper Marcellus, and lower Marcellus is strongly affected by heterogeneity of mineral composition.

Samples from clay-rich reservoirs contain pore system dominated by relatively large, primary, clay-hosted pores (Figure 4-8 C). The stacking pattern of the grain assemblage strongly impacts the porosity and pore size. This type of horizon is observed in the middle section of

Mahantango Formation. The TOC of this pore-micro-texture facies is less than 1%. Although it has the least OM, clay rich beds yield the highest TR. Clay particles tend to form triangle shaped pore space, which can be a shelter for OM pores from the mechanical compaction.

Organic-lean pore-micro-texture facies is the background depositional texture in this study. It has been found in both Mahantango and Marcellus formations. The TOC of this facies type is typically less than 4.5%. Negative correlation between OM porosity and OM suggests that OM is susceptible to compaction, especially during early diagenesis, because OM behaves in a ductile manner (Milliken et al., 2014; Pommer and Milliken, 2015). Pore-filling secondary OM occurs in all the samples. Numerous pores occur on the interface of OM and minerals. Pommer and Milliken, 2015 studied OM-mineral interface pores in Eagle Ford Shale, and attributed the genesis of this pore type to three mechanisms, including: (1) primary inter-particle pores between OM and mineral particles; (2) partial infill of primary pores by ductile detrital OM; and (3) partial infill of pores by mobilized secondary OM.

Organic-rich pore-micro-texture facies are found in the lower Marcellus, with a TOC higher than 4.5%. Large pieces of OM with no SEM visible porosity are common in this type of horizons (Figure 4-12). The porosity resolved in the SEM images, OM-hosted porosity, TR are all very low. Due to the high OM content, the OM-hosted pores received less support from the compaction-resistant mineral-frameworks, thus large OM-hosted pores would not likely be preserved. Mineral-hosted pores were destroyed by abundant secondary OM that filled the primary pores. BET analyses which can resolve porosity below the resolution of the SEM indicates that these organic-rich samples have very high pore surface area and pore volume compared to other samples from the other pore-micro-texture facies with porosity resolvable by

SEM images. The highly organic-rich pore-micro-texture facies of lower Marcellus has better adsorption capacity and free-gas-storage capacity in numerous small pores less than 10nm.

A small amount of OM can still be found in the carbonate-rich pore-micro-texture facies. However, most of the OM is non-porous from SEM images and as measured by BET Pore surface area and pore volume are both low in this type of horizon.

Throughout the Hamilton Group, clay and silica are major building blocks for the formation, except for scattered limestone horizons (Figure 4-1). Yet clay platelets-hosted pores are only well preserved in the middle section of Mahantango shale. Burial, compaction and filling with OM are obvious reasons. Rigid, compaction-resistant grains help maintain the triangular openings between lattice frameworks of clay platelets. So, the initial depositional fabric has a strong influence on the developing diagenetic fabric parameters (Schieber, 2013). Schieber, 2013 argues that the clay lattice frameworks could be explained by deposition of clays from flocculation. In addition, the initial random stacking of clays are easy to be flattened by compaction (Bennett et al., 1991; Schieber, 2013) without support from the compaction-resistant grains.

In addition to initial depositional fabric, secondary OM filling the pre-existing pores is another major destructive mechanism for clay-hosted pores. In the organic-lean samples, the secondary OM only partially filled the clay framework pores (Figure 4-4), whereas in the organic-rich horizons, OM filled most of the pre-existing mineral-hosted pores. The initial amount of organic matter in a shale will place limits on the amount of secondary OM that can be generated and available to fill mineral-hosted pores. In addition, even in the most organic-rich

samples, there still are some unfilled mineral-hosted pores, which can be attributed to the initial connectivity of the mineral-hosted pore system.

Thermal Maturity and Development of OM Hosted Pores

The amorphous occurrence of OM within mineral-hosted pores can be explained by the thermal maturation and migration of bitumen. When kerogen going through increasing thermal maturity, it may first be converted to bitumen that fill the pore space between minerals. After hydrocarbon is generated and expelled from bitumen, the residual OM can either being preserved, or destroyed by compaction.

The nature of OM-hosted pores is that during thermal maturation, generation and primary migration of hydrocarbons left behind is an organic residue that texturally resembles a sponge, consisting of a matrix of organic material with abundant tiny foam pores and superimposed larger bubble pores (Schieber, 2013). The beginning of this process is the initiation of hydrocarbon generation (Loucks et al., 2009, 2012; Chalmers and Bustin, 2007; Milliken et al., 2013; Mastalerz et al., 2013; Schieber, 2010, 2013; Valenza et al., 2013). Schieber, 2013 noted that, well developed OM porosity should be occur only within organic-rich shales that have reached the gas window or approximately greater than 1.1%Ro.

The samples in this study cover a thermal maturity range from wet gas to post mature zone. The results of the BET analyses indicate a pore structure change has been found. From the Mahantango Formation through to the lower member of the Marcellus Shale, TOC increases along with a significant increase in pore smaller than 5 nm. In the Marcellus Shale, from wet gas zone (well G55) to dry gas zone (well A1), the number of pores with size between 1 to 3 nm also increases significantly. When it comes to the post mature zone sampled in well CS1, most of the

pores smaller than 3nm were not observed. As discussed earlier, those very small pores are mostly OM-hosted pores. This observation suggests that from wet gas to dry gas zone, a large number of 1-to-3-nm pores are generated. When the OM reaches higher thermal maturation in the post mature zone, 1-to-3-nm pores aggregate and form bigger pores. This provides an explanation for the lower pore surface area of samples from well CS1, since smaller pores contribute more to the surface area than bigger pores (Song et al., in prep).

Sponge Model, Mechanism of OM-porosity Development

The development of OM-porosity is a complex function of depositional setting, the origin of OM, thermal history, mineral composition, and compaction history (Bohacs et al., 2013; Milliken et al., 2013; Schieber, 2013). A possible scenario is proposed for development of OM-porosity in the Marcellus Shale. When the formation is heated to the oil window, OM-porosity starts to develop because of the thermal cracking of kerogen and expulsion of liquids and volatiles. Pore space in organic material may generate from one spot in a single piece of kerogen, and grow into a relatively large discrete pore; in contrast hydrocarbon generation from many location in organic material would produce a sponge-like network of OM-hosted pores. In the Appalachian basin, the increase in thermal maturity and pressure is the result of deeper burial of the organic-rich Middle Devonian shale units. The OM (some mixture of kerogen, bitumen, pyrobitumen or even char) hosted porosity will suffer from heavier mechanical compaction. Regions with higher TOCs will be compressed, and hydrocarbons will be expelled more completely because of less support from compaction-resistant mineral-frameworks, and greater OM connectivity. As a result, these regions will show lower OM porosities in the larger pore sizes. On the other hand, regions with lower TOCs may get more support from rigid mineral

frameworks, and compactional expulsion of the hydrocarbon will be inhibited to some extent. So they will show more OM porosity in larger pore sizes.

Mapping sorption storage capacity and free-gas storage capacity from well logs

The positive correlation between TOC and specific surface area, and the negative correlation between bulk density and pore volume in the Middle Devonian Mahantango and Marcellus formations is observed (Figure 4-15). Using these relationships and the TOC and bulk density estimated from well logs and calibrated to the core data, a continuum specific surface area and pore volume predictions can be estimated and mapped across the basin (Figure 4-16, 4-17). Specific surface area and pore volume represent sorption storage capacity and free-gas storage capacity, respectively. The results show the significant storage capacity changes through different horizons and different wells. The sorption capacity is strongly affected by the richness of organic matter as indicated by the gamma-ray response. In the Marcellus Shale, three organic rich horizons are noticed in West Virginia from bottom to the top, with the top horizon being less organic rich compare to the lower horizons. While in Ohio, there are only two organic rich horizons located at the top and bottom of Marcellus Shale. Well CS1 from Pennsylvania only contains one organic-rich horizons at the bottom. The free-gas storage capacity is affected by the porosity. The well from eastern Ohio has the lowest thermal maturity, in wet gas zone and the highest porosity. Moving eastward into the deeper portions of the Appalachian basin and into the dry gas zones represented by cross-section from A to A' shows a decreasing trend of porosity (Figure 4-17). While maturity appears to have a significant impact this trend may also be related to changes in lithology and depositional environment and increased influx of detrital sediments.

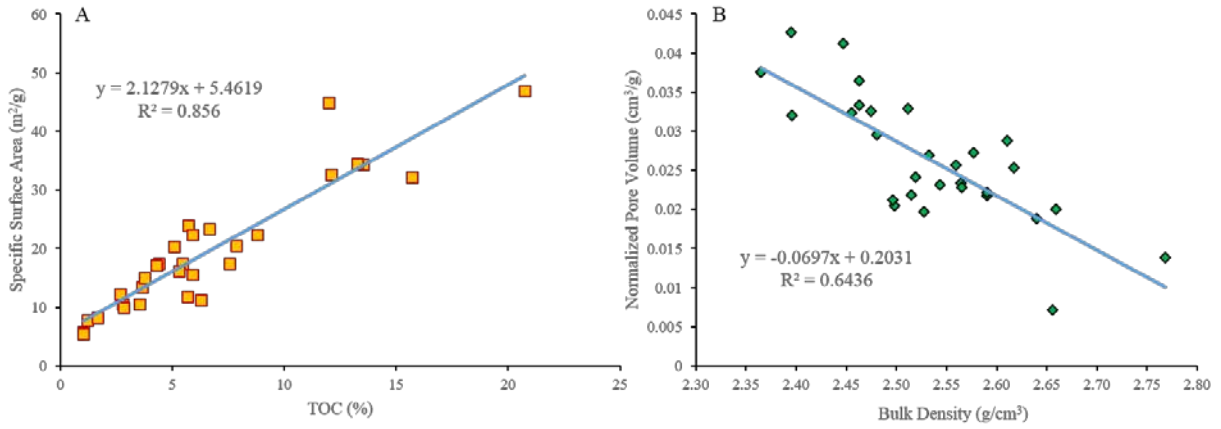


Figure 4-15. A) Positive correlation between TOC and BET specific surface area; B) negative correlation between bulk density and normalized pore volume.

Sorption Storage Capacity: Surface Area

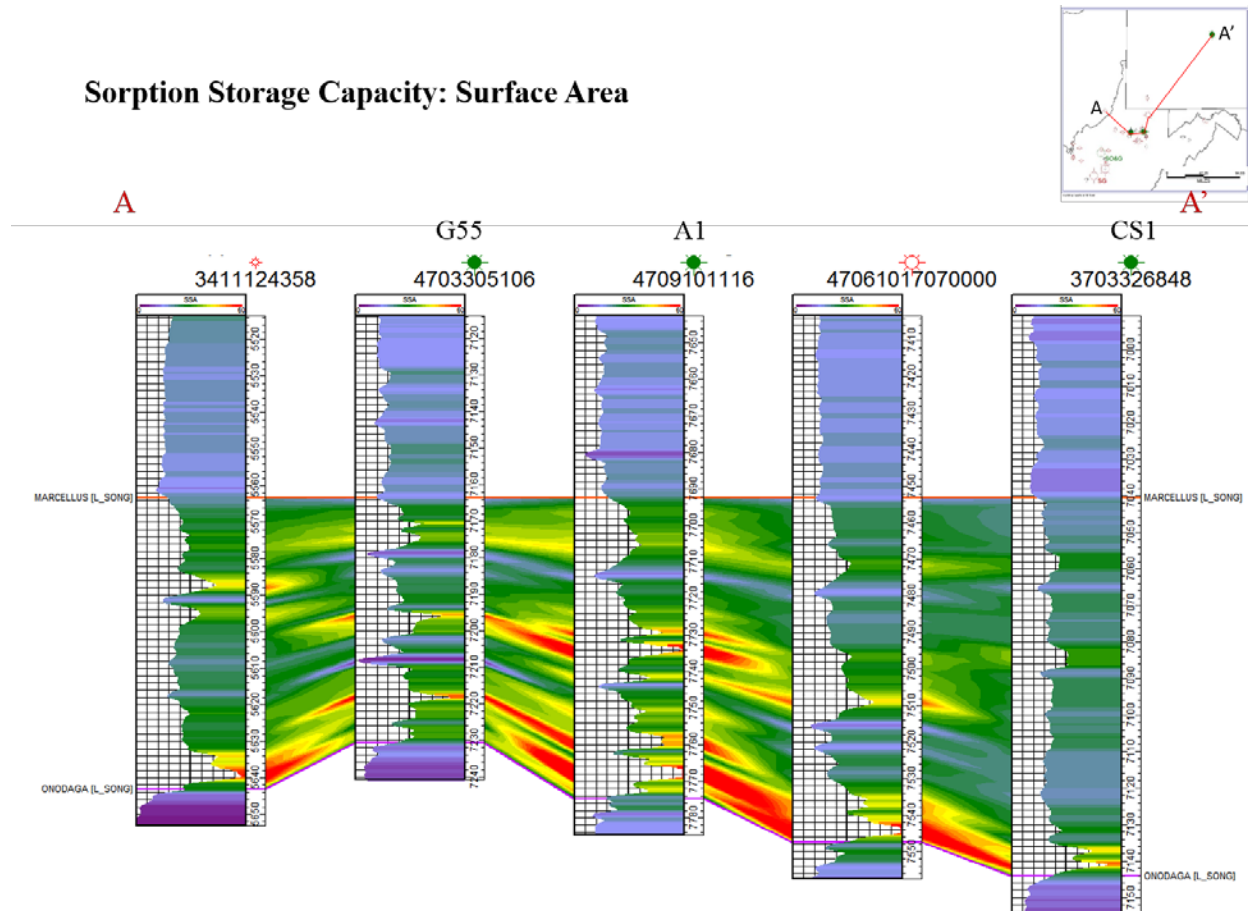


Figure 4-16. Cross-section illustrating the sorption storage capacity change through different horizons in the Marcellus Shale.

Free-gas Storage Capacity: pore volume

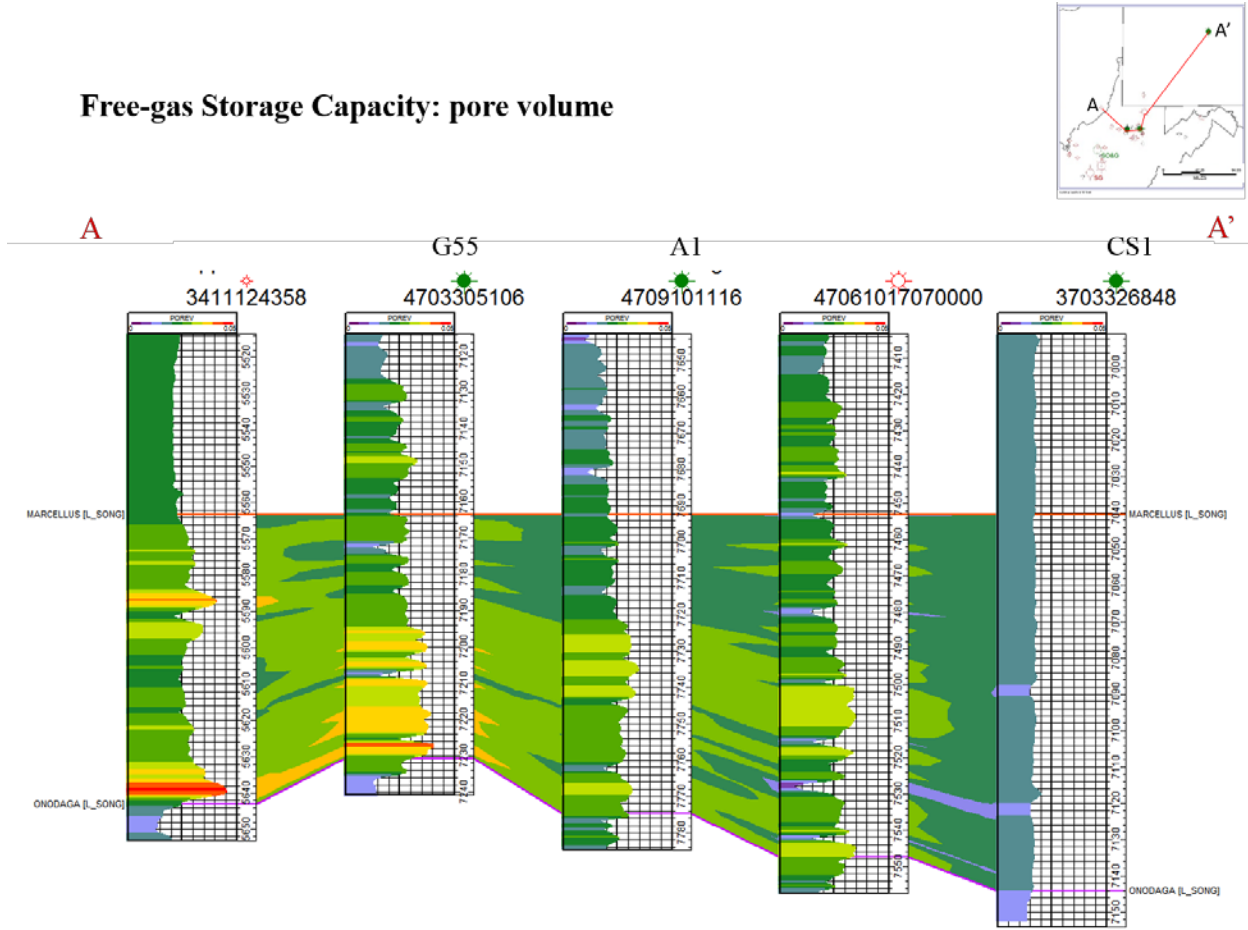


Figure 4-17. Cross-section illustrating the free-gas storage capacity change through different horizons in the Marcellus Shale.

Conclusions

The pore structure of Mahantango and Marcellus formations were characterized using samples from three wells with different thermal maturity, and clay and OM content.

In Mahantango and Marcellus formations in Appalachian basin, evolution of the pore system is driven by compaction, cementation, and OM maturation through both the occlusion of primary porosity and generation of secondary porosity. The stratigraphic distribution of the pore

networks shows that the depositional environment influences the detrital grain assemblage. More rigid grains shelter large primary inter-particle pores from collapsing due to compaction. While, the ductile nature of OM can occlude primary pores and is sensitive to compaction. Smaller pore sizes below the resolution of the SEM dominate the porosity in OM-rich samples. The infill of secondary OM into pre-existing inter-particle or intra-particle pores implies that OM-hosted pores within inter-connected secondary OM have a potentially better connectivity than those occurred within spatially isolated particulate OM. Observations from BET analyses suggest that at high thermal maturity level ($2.67 < R_o < 2.89$), chemical processes have a much stronger effect on pore networks than mechanical compaction. Loss of porosity within high maturity samples has occurred through the significant decrease of pores between 1 and 3 nm. Generation of porosity within OM shows substantial heterogeneity, and varies as a function of the amount of OM, thermal maturity, and rock fabric.

In the organic-rich shale horizons ($TOC > 4.5\%$), mineral-hosted pores may be initially filled by non-porous OM (secondary OM) that may be converted to porous bitumen at a higher thermal maturity. The mineral-hosted pores will be filled/occupied by part of the OM, in which case the OM pores are preserved by clay microstructure. Those OM surrounding silica or carbonate grains will suffer from compaction, and pores developed in it can hardly be preserved. Organic-lean horizons, on the other hand, may preserve many of the mineral-hosted pores.

Ion milled-SEM is a powerful technology to study mudrock reservoirs. By appropriate sampling, representative images can be achieved. However, due to the inability to resolve porosity less than 10nm, SEM analysis will underestimate the porosity. This underestimation mainly occurs in OM porosity. In the Marcellus organic-rich shale, a significant portion of the

effective porosity, sorption storage capacity and free-gas storage capacity is smaller than 10 nm and with current technology cannot be visually resolved.

Reference Cited:

- Adesida, A. G., I. Y. Akkutlu, D. E. Resasco, and C. S. Rai, 2011, SPE 147397 Kerogen Pore Size Distribution of Barnett Shale using DFT Analysis and Monte Carlo Simulations: SPE Annual Technical Conference and Exhibition, p. 1–14, doi:10.2118/147397-MS.
- Ambrose, R. J., D. Energy, R. C. Hartman, and W. Labs, 2010, SPE 131772 New Pore-scale Considerations for Shale Gas in Place Calculations: doi:10.2118/131772-MS.
- Anovitz, L. M., and D. R. Cole, 2015, Characterization and Analysis of Porosity and Pore Structures: Reviews in Mineralogy and Geochemistry, v. 80, p. 61–164, doi:10.2138/rmg.2015.80.04.
- Bai, B., M. Elgmati, H. Zhang, and M. Wei, 2013, Rock characterization of Fayetteville shale gas plays: Fuel, v. 105, p. 645–652, doi:10.1016/j.fuel.2012.09.043.
- Barrett, E. P., L. G. Joyner, and P. P. Halenda, 1951, The determination of pore volume and area distributions in porous substances. I. computations from nitrogen isotherms: Journal of the American Chemical Society, v. 73, no. 1, p. 373–380, doi:10.1021/ja01145a126.
- Bennett, R. H., N. R. O. Brien, M. H. Hulbert, O. S. Directorate, N. Oceanographic, O. S. Directorate, and N. Oceanographic, 1991, Determinants of clay microfabric signatures- Processes and mechanisms, *in* Microstructure of fine-grained sediments: New York, Springer-Verlag, p. 5–32.
- Bernard, S., L. Brown, R. Wirth, A. Schreiber, H.-M. Schulz, B. Horsfield, A. C. Aplin, and E. J. Mathia, 2013, FIB-SEM and TEM Investigations of an Organic-rich Shale Maturation Series from the Lower Toarcian Posidonia Shale, Germany: Nanoscale Pore System and Fluid-rock Interactions: Electron microscopy of shale hydrocarbon reservoirs: AAPG Memoir 102, p. 53–66, doi:10.1306/13391705M1023583.

- Bohacs, K. M., Q. R. Passey, M. Rudnicki, W. L. Esch, and O. R. Lazar, 2013, The Spectrum of Fine-Grained Reservoirs from “Shale Gas” to “Shale Oil”/ Tight Liquids : Essential Attributes, Key Controls, Practical Characterization: IPTC 2013: International Petroleum Technology Conference, no. Figure 1, p. 1–16, doi:10.2523/16676-MS.
- Boyce, M., A. Yanni, and T. Carr, 2010, Depositional control of organic content in the Middle Devonian Marcellus interval of West Virginia and Western Pennsylvania: Critical Assessment of ..., p. 3–6.
- Brunauer, S., P. H. Emmett, and E. Teller, 1938, Adsorption of Gases in Multimolecular Layers: Journal of the American Chemical Society, v. 60, no. 1, p. 309–319, doi:citeulike-article-id:4074706\rdoi: 10.1021/ja01269a023.
- Bustin, R. M., A. M. M. Bustin, B. Columbia, X. Cui, and D. J. K. Ross, 2008, SPE 119892 Impact of Shale Properties on Pore Structure and Storage Characteristics.
- Bustin, R. M., a Bustin, D. Ross, G. Chalmers, V. Murthy, C. Laxmi, and X. Cui, 2009, Shale Gas Opportunities and Challenges *: Search and Discovery Articles, v. 40382.
- Carr, T. R. et al., 2016, The Marcellus Shale Energy and Environment Laboratory (MSEEL)*, in AAPG Eastern Section Meeting, Lexington, Kentucky.
- Chalmers, G. R. L., and R. Marc Bustin, 2007, On the effects of petrographic composition on coalbed methane sorption: International Journal of Coal Geology, v. 69, no. 4, p. 288–304, doi:10.1016/j.coal.2006.06.002.
- Chalmers, G. R. L., D. J. K. Ross, and R. M. Bustin, 2012, Geological controls on matrix permeability of Devonian Gas Shales in the Horn River and Liard basins, northeastern British Columbia, Canada: International Journal of Coal Geology, v. 103, p. 120–131, doi:10.1016/j.coal.2012.05.006.

- Chen, R., and S. Sharma, 2017, Linking the Acadian Orogeny with organic-rich black shale deposition: Evidence from the Marcellus Shale: *Marine and Petroleum Geology*, v. 79, p. 149–158, doi:10.1016/j.marpetgeo.2016.11.005.
- Chen, R., and S. Sharma, 2016, Role of alternating redox conditions in the formation of organic-rich interval in the Middle Devonian Marcellus Shale , Appalachian Basin , USA: *Palaeogeography, Palaeoclimatology, Palaeoecology*, v. 446, p. 85–97, doi:10.1016/j.palaeo.2016.01.016.
- Chen, R., S. Sharma, T. Bank, D. Soeder, and H. Eastman, 2015, Comparison of isotopic and geochemical characteristics of sediments from a gas- and liquids-prone wells in Marcellus Shale from Appalachian Basin, West Virginia: *Applied Geochemistry*, v. 60, p. 59–71, doi:10.1016/j.apgeochem.2015.01.001.
- Clarkson, C. R., J. M. Wood, S. E. Burgis, S. D. Aquino, and M. Freeman, 2012, Nanopore-structure analysis and permeability predictions for a tight gas siltstone reservoir by use of low-pressure adsorption and mercury-intrusion techniques: *SPE Reservoir Evaluation & Engineering*, v. 15, no. 6, p. 648–661, doi:10.2118/155537-PA.
- Crain, E. R., and D. Holgate, 2014, A 12-Step program to reduce uncertainty in kerogen-rich reservoirs: *Canadian Well Logging Society*, v. i, no. Spring, p. 10–16.
- Culligan, K. A., D. Wildenschild, B. S. B. Christensen, W. G. Gray, and M. L. Rivers, 2006, Pore-scale characteristics of multiphase flow in porous media : A comparison of air – water and oil – water experiments: *Advances in Water Resources*, v. 29, p. 227–238, doi:10.1016/j.advwatres.2005.03.021.
- Culligan, K. A., D. Wildenschild, B. S. B. Christensen, W. G. Gray, M. L. Rivers, and A. F. B. Tompson, 2004, Interfacial area measurements for unsaturated flow through a porous

- medium: *Water Resources Research*, v. 40, no. W12413, p. 1–12,
doi:10.1029/2004WR003278.
- Curtis, M. E., and R. J. Ambrose, 2011, Investigation of the relationship between organic porosity and thermal maturity in the Marcellus Shale, *in* SPE Conference: p. 4pp,
doi:10.2118/144370-ms.
- Curtis, M. E., C. H. Sondergeld, R. J. Ambrose, and C. S. Rai, 2012, Microstructural investigation of gas shales in two and three dimensions using nanometer-scale resolution imaging: *AAPG Bulletin*, v. 96, no. 4, p. 665–677, doi:10.1306/08151110188.
- Deirieh, A., 2016, *From Clay Slurries to Mudrocks : A Cryo-SEM Investigation of the Development of the Porosity and Microstructure*: Massachusetts Institute of Technology, 226 p.
- Desbois, G., J. L. Urai, and P. A. Kukla, 2009, Morphology of the pore space in claystones – evidence from BIB/FIB ion beam sectioning and cryo-SEM observations: *eEarth Discussions*, v. 4, no. 1, p. 1–19, doi:10.5194/eed-4-1-2009.
- Dilks, A., and S. C. Graham, 1985, Quantitative Mineralogical Characterization of Sandstones by Back-scattered Electron Image Analysis: *Journal of Sedimentary Petrology*, v. 55, no. 3, p. 347–355.
- Dong, T., and N. B. Harris, 2013, Pore Size Distribution and Morphology in the Horn River Shale, Middle and Upper Devonian, Northeastern British Columbia, Canada: *Electron microscopy of shale hydrocarbon reservoirs: AAPG Memoir 102*, p. 67–80,
doi:10.1306/13391706M1023584.
- Driskill, B., J. Walls, J. DeVito, and S. W. Sinclair, 2013, Applications of SEM Imaging to Reservoir Characterization in the Eagle Ford Shale, South Texas, U.S.A., *in* *Electron*

- microscopy of shale hydrocarbon reservoirs: AAPG Memoir 102: p. 115–136,
doi:10.1306/13391709M1023587.
- EIA, U. S., 2018, Annual Energy Outlook 2018 with projections to 2050 Table of contents:
Washington, DC, 74 p.
- Erdman, N., and N. Drenzek, 2013, Integrated Preparation and Imaging Techniques for the
Microstructural and Geochemical Characterization of Shale by Scanning Electron
Microscopy: Electron microscopy of shale hydrocarbon reservoirs: AAPG Memoir 102, p.
7–14, doi:10.1306/13391700M1023581.
- Espitalie, J., G. Deroo, and F. Marquis, 1985, La pyrolyse Rock-Eval et ses applications.
Deuxième partie.: Revue de l'Institut Français du Pétrole, v. 40, no. 6, p. 755–784,
doi:10.2516/ogst:1985045.
- Ettensohn, F. R., and T. R. Lierman, 2012, Large-scale Tectonic Controls on the Origin of
Paleozoic Dark-shale Source-rock Basins: Examples from the Appalachian Foreland Basin,
Eastern United States: AAPG Bulletin, v. 100, no. January 2012, p. 95–124,
doi:10.1306/13351549M1003529.
- Fishman, N. S., J. L. Ridgley, D. K. Higley, M. L. W. Tuttle, and D. L. Hall, 2012, Ancient
Microbial Gas in the Upper Cretaceous Milk River Formation, Alberta and Saskatchewan:
A Large Continuous Accumulation in Fine-grained Rocks Neil: Shale Reservoirs —Giant
Resources for the 21st Century: AAPG Memoir 97, v. 97, p. 258–289,
doi:10.1306/13321471M973493.
- Gallagher, N. C. J., and G. L. Wise, 1981, A Theoretical Analysis of the Properties of Median Fi
hers: IEEE Transactions on acoustic, speech, and signal processing, v. 29, no. 6, p. 1136–
1141.

- Giffin, S., R. Littke, J. Klaver, and J. L. Urai, 2013, Application of BIB-SEM technology to characterize macropore morphology in coal: *International Journal of Coal Geology*, v. 114, p. 85–95, doi:10.1016/j.coal.2013.02.009.
- Hemes, S., G. Desbois, J. L. Urai, M. De Craen, and M. Honty, 2013, Variations in the morphology of porosity in the Boom Clay Formation: Insights from 2D high resolution BIB-SEM imaging and Mercury injection Porosimetry: *Geologie en Mijnbouw/Netherlands Journal of Geosciences*, v. 92, no. 4, p. 275–300, doi:doi:10.1017/S0016774600000214.
- Hemes, S., G. Desbois, J. L. Urai, B. Schröppel, and J. O. Schwarz, 2015, Multi-scale characterization of porosity in Boom Clay (HADES-level, Mol, Belgium) using a combination of X-ray u-CT, 2D BIB-SEM and FIB-SEM tomography: *Microporous and Mesoporous Materials*, v. 208, p. 1–20, doi:10.1016/j.micromeso.2015.01.022.
- Houben, M. E., G. Desbois, and J. L. Urai, 2014, A comparative study of representative 2D microstructures in Shaly and Sandy facies of Opalinus Clay (Mont Terri, Switzerland) inferred from BIB-SEM and MIP methods: *Marine and Petroleum Geology*, v. 49, p. 143–161, doi:10.1016/j.marpetgeo.2013.10.009.
- Houben, M. E., G. Desbois, and J. L. Urai, 2013, Pore morphology and distribution in the Shaly facies of Opalinus Clay (Mont Terri, Switzerland): Insights from representative 2D BIB-SEM investigations on mm to nm scale: *Applied Clay Science*, v. 71, p. 82–97, doi:10.1016/j.clay.2012.11.006.
- Huang, J., T. Cavanaugh, and B. Nur, 2013, An Introduction to SEM Operational Principles and Geologic Applications for Shale Hydrocarbon Reservoirs: *Electron microscopy of shale hydrocarbon reservoirs: AAPG Memoir 102*, p. 1–6, doi:10.1306/13391699M1023580.
- Jarvie, D. M., R. J. Hill, T. E. Ruble, and R. M. Pollastro, 2007, *Unconventional shale-gas*

- systems: The Mississippian Barnett Shale of north-central Texas as one model for thermogenic shale-gas assessment: *AAPG Bulletin*, v. 91, no. 4, p. 475–499, doi:10.1306/12190606068.
- Katz, A. J., and A. H. Thompson, 1985, Fractal Sandstone Pores: Implications for Conductivity and Pore Formation: *Physical Review Letters*, v. 54, no. 12, p. 1325–1328.
- Kelly, S., H. El-sobky, C. Torres-verdín, and M. T. Balhoff, 2016, Advances in Water Resources Assessing the utility of FIB-SEM images for shale digital rock physics: *Advances in Water Resources*, v. 95, p. 302–316, doi:10.1016/j.advwatres.2015.06.010.
- Klaver, J., G. Desbois, R. Littke, and J. L. Urai, 2015, BIB-SEM characterization of pore space morphology and distribution in postmature to overmature samples from the Haynesville and Bossier Shales: *Marine and Petroleum Geology*, v. 59, p. 451–466, doi:10.1016/j.marpetgeo.2014.09.020.
- Klaver, J., G. Desbois, J. L. Urai, and R. Littke, 2012, BIB-SEM study of the pore space morphology in early mature Posidonia Shale from the Hils area, Germany: *International Journal of Coal Geology*, v. 103, p. 12–25, doi:10.1016/j.coal.2012.06.012.
- Ko, L. T., R. G. Loucks, K. L. Milliken, Q. Liang, T. Zhang, X. Sun, P. C. Hackley, S. C. Ruppel, and S. Peng, 2017, Controls on pore types and pore-size distribution in the Upper Triassic Yanchang Formation , Ordos Basin , China : Implications for pore-evolution models of lacustrine mudrocks: *Interpretation*, v. 5, no. 2, p. 127–148, doi:10.1190/INT-2016-0115.1.
- Kuila, U., and M. Prasad, 2013, Specific surface area and pore-size distribution in clays and shales: *Geophysical Prospecting*, v. 61, no. 2, p. 341–362, doi:10.1111/1365-2478.12028.
- Lash, G. G., and D. R. Blood, 2014, Organic matter accumulation, redox, and diagenetic history

- of the Marcellus Formation, southwestern Pennsylvania, Appalachian basin: *Marine and Petroleum Geology*, v. 57, no. November, p. 244–263,
doi:10.1016/j.marpetgeo.2014.06.001.
- Lash, G. G., and T. Engelder, 2011, Thickness trends and sequence stratigraphy of the Middle Devonian Marcellus Formation, Appalachian Basin: Implications for Acadian foreland basin evolution: *AAPG Bulletin*, v. 95, no. 1, p. 61–103, doi:10.1306/06301009150.
- Lazar, R., K. Bohacs, R. Klimentidis, M. Dumitrescu, and J. Ottmann, 2016, An SEM Study of Porosity in the Eagle Ford Shale of Texas—Pore Types and Porosity Distribution in a Depositional and Sequence-stratigraphic Context: *The Eagle Ford Shale: A renaissance in U.S. oil production: AAPG Memoir 110*, p. 167–186, doi:10.1306/13541961M1103589.
- Lazar, O. R., K. M. Bohacs, J. H. S. Macquaker, J. Schieber, and T. M. Demko, 2015, Capturing Key Attributes of Fine-Grained Sedimentary Rocks In Outcrops, Cores, and Thin Sections: Nomenclature and Description Guidelines: *Journal of Sedimentary Research*, v. 85, no. 3, p. 230–246.
- Loucks, R. G., R. M. Reed, S. C. Ruppel, and U. Hammes, 2012, Spectrum of pore types and networks in mudrocks and a descriptive classification for matrix-related mudrock pores: *AAPG Bulletin*, v. 96, no. 6, p. 1071–1098, doi:10.1306/08171111061.
- Loucks, R. G., R. M. Reed, S. C. Ruppel, and D. M. Jarvie, 2009, Morphology, Genesis, and Distribution of Nanometer-Scale Pores in Siliceous Mudstones of the Mississippian Barnett Shale: *Journal of Sedimentary Research*, v. 79, no. 12, p. 848–861,
doi:10.2110/jsr.2009.092.
- Luffel, D. L., and F. K. Guidry, 1992, New Core Analysis Methods for Measuring Reservoir Rock Properties of Devonian Shale, *in* SPE Annual Technical Conference and Exhibition:

p. 1184–1190, doi:10.2118/20571-PA.

Mastalerz, M., A. Schimmelmann, A. Drobniak, and Y. Chen, 2013, Porosity of Devonian and Mississippian New Albany Shale across a maturation gradient: Insights from organic petrology', gas adsorption, and mercury intrusion: AAPG Bulletin, v. 97, no. 10, p. 1621–1643, doi:10.130/04011312194.

Matthew, B. L., and T. R. Carr, 2009, Lithostratigraphy and Petrophysics of the Devonian Marcellus Interval in West Virginia and Southwestern Pennsylvania.

Milliken, K. L., and R. J. Day-Stirrat, 2013, Cementation in mudrocks: Brief review with examples from cratonic basin mudrocks: AAPG Memoir, v. 103, p. 133–150, doi:10.1306/13401729H5252.

Milliken, K. L., R. J. Day-Stirrat, P. K. Papazis, and C. Dohse, 2012, Carbonate Lithologies of the Mississippian Barnett Shale, Fort Worth Basin, Texas: Shale reservoirs—Giant resources for the 21st century, p. 290–321, doi:10.1306/13321473M97252.

Milliken, K. L., W. L. Esch, R. M. Reed, and T. Zhang, 2012, Grain assemblages and strong diagenetic overprinting in siliceous mudrocks, Barnett Shale (Mississippian), Fort Worth Basin, Texas: AAPG Bulletin, v. 96, no. 8, p. 1553–1578, doi:10.1306/12011111129.

Milliken, K. L., L. T. Ko, M. Pommer, and K. M. Marsaglia, 2014, Sem Petrography of Eastern Mediterranean Sapropels: Analogue Data For Assessing Organic Matter In Oil and Gas Shales: Journal of Sedimentary Research, v. 84, no. 11, p. 961–974, doi:10.2110/jsr.2014.75.

Milliken, K. L., and T. Olson, 2016, Amorphous and Crystalline Solids as Artifacts in SEM Images: p. 1–8, doi:10.1306/13592013M112252.

Milliken, K. L., and R. M. Reed, 2010, Multiple causes of diagenetic fabric anisotropy in weakly

- consolidated mud , Nankai accretionary prism , IODP Expedition 316: *Journal of Structural Geology*, v. 32, no. 12, p. 1887–1898, doi:10.1016/j.jsg.2010.03.008.
- Milliken, K. L., M. Rudnicki, D. N. Awwiller, and T. Zhang, 2013, Organic matter-hosted pore system, Marcellus Formation (Devonian), Pennsylvania: *AAPG Bulletin*, v. 97, no. 2, p. 177–200, doi:10.1306/07231212O48.
- Mosher, K., J. He, Y. Liu, E. Rupp, and J. Wilcox, 2013, Molecular simulation of methane adsorption in micro- and mesoporous carbons with applications to coal and gas shale systems: *International Journal of Coal Geology*, v. 109–110, p. 36–44, doi:10.1016/j.coal.2013.01.001.
- Nole, M., H. Daigle, K. L. Milliken, and M. Prodanovic, 2016, A method for estimating microporosity of fine-grained sediments and sedimentary rocks via scanning electron microscope image analysis: *Sedimentology*, v. 63, no. 6, p. 1507–1521, doi:10.1111/sed.12271.
- Olson, E., 2012, The Importance of Sample Preparation when Measuring Specific Surface Area: *Journal of GXP Compliance*, v. 16, no. 3, p. 52~62.
- Otsu, N., 1979, A Threshold Selection Method from Gray-Level Histograms: *IEEE Transactions on Systems, Man, and Cybernetics*, v. 19, no. 1, p. 62–66, doi:10.1109/TSMC.1979.4310076.
- Passey, Q. R., K. M. Bohacs, W. L. Esch, R. E. Klimentidis, and S. K. Sinha, 2012, My source rock is now my reservoir - geologic and petrophysical characterization of shale-gas reservoirs: *Search and Discovery*, v. 80231, no. 80231, p. 47pp.
- Phansalkart, N., S. More, A. Sabale, and M. Joshi, 2011, Adaptive Local Thresholding for Detection of Nuclei in Diversity Stained Cytology Images, *in International Conference on*

Communications and Signal Processing: p. 218–220.

Pommer, M., and K. Milliken, 2015, Pore types and pore-size distributions across thermal maturity, Eagle Ford Formation, southern Texas: AAPG Bulletin, v. 99, no. 9, p. 1713–1744, doi:10.1306/03051514151.

Reed, R. M., R. G. Loucks, and S. C. Ruppel, 2014, Comment on “ Formation of nanoporous pyrobitumen residues during maturation of the Barnett Shale (Fort Worth Basin) ” by Bernard et al . (2012): International Journal of Coal Geology, v. 127, p. 111–113, doi:10.1016/j.coal.2013.11.012.

Ross, D. J. K., and R. M. Bustin, 2008a, Characterizing the shale gas resource potential of Devonian-Mississippian strata in the Western Canada sedimentary basin: Application of an integrated formation evaluation: AAPG Bulletin, v. 92, no. 1, p. 87–125, doi:10.1306/09040707048.

Ross, D. J. K., and R. M. Bustin, 2008b, Characterizing the shale gas resource potential of Devonian-Mississippian strata in the Western Canada sedimentary basin: Application of an integrated formation evaluation: AAPG Bulletin, v. 92, no. 1, p. 87–125, doi:10.1306/09040707048.

Ross, D. J. K., and R. M. Bustin, 2009, The importance of shale composition and pore structure upon gas storage potential of shale gas reservoirs: Marine and Petroleum Geology, v. 26, no. 6, p. 916–927, doi:10.1016/j.marpetgeo.2008.06.004.

Ross, D. J. K., and R. M. Bustin, 2009, The importance of shale composition and pore structure upon gas storage potential of shale gas reservoirs: Marine and Petroleum Geology, v. 26, no. 6, p. 916–927, doi:10.1016/j.marpetgeo.2008.06.004.

Ross, D. J. K., and R. Marc Bustin, 2007, Impact of mass balance calculations on adsorption

capacities in microporous shale gas reservoirs: *Fuel*, v. 86, no. 17–18, p. 2696–2706,
doi:10.1016/j.fuel.2007.02.036.

Sageman, B. B., A. E. Murphy, J. P. Werne, C. A. Ver Straeten, D. J. Hollander, and T. W. Lyons, 2003, A tale of shales: The relative roles of production, decomposition, and dilution in the accumulation of organic-rich strata, Middle-Upper Devonian, Appalachian basin: *Chemical Geology*, v. 195, no. 1–4, p. 229–273, doi:10.1016/S0009-2541(02)00397-2.

Saidian, M., L. J. Godinez, and M. Prasad, 2016, Effect of clay and organic matter on nitrogen adsorption specific surface area and cation exchange capacity in shales (mudrocks): *Journal of Natural Gas Science and Engineering*, v. 33, p. 1095–1106,
doi:10.1016/j.jngse.2016.05.064.

Saidian, M., L. J. Godinez, and M. Prasad, 2015, Effect of Clay and Organic Matter on Nitrogen Adsorption Specific Surface Area and Cation Exchange Capacity in Shales (Mudrocks): *Annual Logging Symposium*, v. 56, p. 1–16.

Sauvola, J., and M. Pietikainen, 2000, Adaptive document image binarization: *Pattern recognition*, v. 33, p. 225–236.

Schieber, J., 2010, Common Themes in the Formation and Preservation of Intrinsic Porosity in Shales and Mudstones - Illustrated with Examples Across the Phanerozoic: *SPE Unconventional Gas Conference*, p. 10, doi:10.2118/132370-MS.

Schieber, J., 2013, SEM Observations on Ion-milled Samples of Devonian Black Shales from Indiana and New York: The Petrographic Context of Multiple Pore Types: *Electron microscopy of shale hydrocarbon reservoirs: AAPG Memoir 102*, no. April 2010, p. 153–172, doi:10.1306/13391711M1023589.

Schindelin, J. et al., 2012, Fiji: an open source platform for biological image analysis.: *Nature*

- Methods, v. 9, no. 7, p. 676–682, doi:10.1038/nmeth.2019.Fiji.
- Schindelin, J., C. T. Rueden, M. C. Hiner, and K. W. Eliceiri, 2015, The ImageJ ecosystem: An open platform for biomedical image analysis: *Molecular Reproduction and Development*, v. 82, no. 7–8, p. 518–529, doi:10.1002/mrd.22489.
- Schneider, J., P. B. Flemings, R. J. Day-Stirrat, and J. T. Germaine, 2011, Insights into pore-scale controls on mudstone permeability through resedimentation experiments: *Geology*, v. 39, no. 11, p. 1011–1014, doi:10.1130/G32475.1.
- Schneider, C. a, W. S. Rasband, and K. W. Eliceiri, 2012, NIH Image to ImageJ: 25 years of image analysis: *Nature Methods*, v. 9, no. 7, p. 671–675, doi:10.1038/nmeth.2089.
- Sezgin, M., and B. Sankur, 2004, Survey over image thresholding techniques and quantitative performance evaluation: *Journal of Electronic Imaging*, v. 13, no. 1, p. 146–168, doi:10.1117/1.1631316.
- Sing, K., 2001, The use of nitrogen adsorption for the characterisation of porous materials: *Colloids and Surfaces A: Physicochemical and Engineering Aspects*, v. 187–188, p. 3–9, doi:10.1016/S0927-7757(01)00612-4.
- Sing, K. S. W., D. H. Everett, R. a. W. Haul, L. Moscou, R. a. Pierotti, J. Rouquérol, and T. Siemieniowska, 1982, Reporting Physisorption Data for Gas / Solid Systems with Special Reference to the Determination of Surface Area and Porosity: *Pure and Applied Chemistry*, v. 57, no. 4, p. 603–619, doi:10.1351/pac198557040603.
- Sing, K. S. W., and R. T. Williams, 2004, Physisorption hysteresis loops and the characterization of nanoporous materials: *Adsorption Science and Technology*, v. 22, no. December 2015, p. 773–782, doi:10.1260/0263617053499032.
- Slatt, R. M., and N. R. O'Brien, 2013, *Microfabrics Related to Porosity Development*,

- Sedimentary and Diagenetic Processes, and Composition of Unconventional Resource Shale Reservoirs as Determined by Conventional Scanning Electron Microscopy: Electron microscopy of shale hydrocarbon reservoirs: AAPG Memoir 102, p. 37–44, doi:10.1306/13391703M102441.
- Slatt, R. M., and N. R. O'Brien, 2011, Pore types in the Barnett and Woodford gas shales: Contribution to understanding gas storage and migration pathways in fine-grained rocks: AAPG Bulletin, v. 95, no. 12, p. 2017–2030, doi:10.1306/03301110145.
- Soeder, D. J., 2017, The Development of Natural Gas from the Marcellus Shale: Boulder, Colorado, The Geological Society of America, 143 p.
- Sondergeld, C. H., R. J. Ambrose, C. S. Rai, and J. Moncrieff, 2010, Micro-structural studies of gas shales: Society of Petroleum Engineers Unconventional Gas Conference, SPE Paper 131771, p. 17, doi:10.2118/131771-MS.
- Song, L., T. Paronish, V. Agrawal, B. Hupp, and S. Sharma, 2017, Depositional Environment and Impact on Pore Structure and Gas Storage Potential of Middle Devonian Organic Rich Shale, Northeastern West Virginia, Appalachian Basin, *in* Unconventional Resources Technology Conference (URTeC:2667397): doi:10.15530/urtec-2017-2667397.
- Strapoć, D., M. Mastalerz, A. Schimmelmann, A. Drobniak, and N. R. Hasenmueller, 2010, Geochemical constraints on the origin and volume of gas in the New Albany Shale (Devonian-Mississippian), eastern Illinois Basin: AAPG Bulletin, v. 94, no. 11, p. 1713–1740, doi:10.1306/06301009197.
- Thommes, M., K. Kaneko, A. V. Neimark, J. P. Olivier, F. Rodriguez-Reinoso, J. Rouquerol, and K. S. W. Sing, 2015, Physisorption of gases, with special reference to the evaluation of surface area and pore size distribution (IUPAC Technical Report): Pure and Applied

- Chemistry, v. 87, no. 9–10, p. 1051–1069, doi:10.1515/pac-2014-1117.
- Tian, H., L. Pan, X. Xiao, R. W. T. Wilkins, Z. Meng, and B. Huang, 2013, A preliminary study on the pore characterization of Lower Silurian black shales in the Chuandong Thrust Fold Belt, southwestern China using low pressure N₂ adsorption and FE-SEM methods: *Marine and Petroleum Geology*, v. 48, p. 8–19, doi:10.1016/j.marpetgeo.2013.07.008.
- Velde, B., 1996, Compaction trends of clay-rich deep sea sediments: *Marine Geology*, v. 133, p. 193–201.
- Walls, J. D., and E. Diaz, 2011, Relationship of shale porosity- permeability trends to pore type and organic content: *Petrophysics in Tight Oil Workshop*.
- Wang, G., and T. R. Carr, 2013, Organic-rich marcellus shale lithofacies modeling and distribution pattern analysis in the appalachian basin: *AAPG Bulletin*, v. 97, no. 12, p. 2173–2205, doi:10.1306/05141312135.
- Wang, G., Y. Ju, Z. Yan, and Q. Li, 2015, Pore structure characteristics of coal-bearing shale using fluid invasion methods: A case study in the Huainan-Huaibei Coalfield in China: *Marine and Petroleum Geology*, v. 62, p. 1–13, doi:10.1016/j.marpetgeo.2015.01.001.
- Wildenschild, D., and A. P. Sheppard, 2013, X-ray imaging and analysis techniques for quantifying pore-scale structure and processes in subsurface porous medium systems: *Advances in Water Resources*, v. 51, p. 217–246, doi:10.1016/j.advwatres.2012.07.018.
- Yu, W., K. Sepehrnoori, and T. W. Patzek, 2016, Modeling Gas Adsorption in Marcellus Shale With Langmuir and BET Isotherms.: *SPE Journal*, v. 21, no. 2, p. 589–600, doi:10.2118/170801-PA.
- Zagorski, W. a., G. R. Wrightstone, and D. C. Bowman, 2012, *The Appalachian Basin Marcellus Gas Play: Its History of Development, Geologic Controls on Production, and Future*

Potential as a World-class Reservoir, *in* AAPG Memoir 97: Shale Reservoirs-Giant Resources for the 21st Century: p. 172–200, doi:10.1306/13321465M973491.

Zhang, T., G. S. Ellis, S. C. Ruppel, K. Milliken, and R. Yang, 2012, Organic Geochemistry Effect of organic-matter type and thermal maturity on methane adsorption in shale-gas systems: *Organic Geochemistry*, v. 47, p. 120–131, doi:10.1016/j.orggeochem.2012.03.012.

Zhang, S., R. E. Klimentidis, and P. Barthelemy, 2011, Porosity and permeability analysis on nanoscale FIB-SEM 3D imaging of shale rock, *in* International Symposium of the Society of Core Analysis: p. 1–12.

Summary

The pore structure of the Marcellus Shale was studied by various available data at the core scale and upscaled to a regional level. The following conclusions based on the results in this study are drawn:

- 1) A new workflow is presented to quantify porosity and OM content from SEM image analysis. The segmentation of pore space and OM is based on adaptive local thresholding, Otsu thresholding, and Image Calculator. The workflow is documented to improve the consistency and efficiency of quantitative image analysis while maintaining acceptable accuracy.
- 2) Quantitative visual analysis of 2D-SEM images is representative when estimating richness of OM. However, it can underestimate the porosity compare to GRI method. This may be the result of differences in pore size resolution.
- 3) Four pore micro-texture facies are picked, organic-rich, organic-lean, clay-rich, carbonate-rich, and they showed a stratigraphic distribution
- 4) Subcritical N₂ adsorption tests indicate that micro- to meso-pores are concentrated in the OM. Pore volume and pore surface area both show good positive correlations with TOC.
- 5) The presence of organic matter in shale strongly enhances the storage capacity by increasing the specific surface area and pore volume.
- 6) A negative correlation is found between clay content and SSA and pore volume. We suspect the accessibility of the pore space within clay minerals has been blocked.

- 7) The development of OM hosted pores is altered during thermal maturation. Shales in dry gas window show highest specific surface area and pore volume. Samples from post-matured zone show a reduced range of storage capacity under the same TOC level.
- 8) As thermal maturity increases from dry-gas zone to post-mature zone, the diminishing of pores within 1 to 3 nm is noticed, and this explained the lower specific surface area results in those highest maturity samples.
- 9) Larger OM-hosted pores are preserved by surrounding rigid grains, while smaller pores (smaller than 10 nm) are suspected to be preserved by abnormal pore pressure.
- 10) Lower Marcellus has higher adsorption capacity than Upper Marcellus, the free gas storage capacity doesn't change very significantly.